UNIVERSIDADE FEDERAL DE MINAS GERAIS
Escola de Engenharia
Programa de Pós-Graduação em Engenharia de Estruturas

Diego Magela Lemos

In-plane and buckling analysis of variable angle tow composites

Belo Horizonte
2021

Diego Magela Lemos

In-plane and buckling analysis of variable angle tow composites

Versão final

Dissertação apresentada ao Programa de Pós-Graduação em Engenharia de Estruturas da Escola de Engenharia da Universidade Federal de Minas Gerais como requisito parcial para obtenção do título de Mestre em Engenharia de Estruturas.

Orientador: Carlos Alberto Cimini Jr.

Belo Horizonte
2021

UNIVERSIDADE FEDERAL DE MINAS GERAIS

PROGRAMA DE PÓS-GRADUAÇÃO EM ENGENHARIA DE ESTRUTURAS

ATA DA DEFESA DE DISSERTAÇÃO DE MESTRADO EM ENGENHARIA DE ESTRUTURAS Nº: 379 DO ALUNO DIEGO MAGELA LEMOS.

Às **08:30** horas do dia **03** do mês de **março** de **2021**, reuniu-se, totalmente por videoconferência para atender aos novos protocolos de distanciamento social adotados pelo Governo Federal e pela Prefeitura de Belo Horizonte, que integram medidas para combater o avanço da pandemia de Covid-19, provocada pelo novo coronavírus, a Comissão Examinadora indicada pelo Colegiado do Programa em **02 de março de 2021**, para julgar a defesa da Dissertação de Mestrado intitulada **"In-Plane and Buckling Analysis of Variable Angle Tow Composites"**, cuja aprovação é um dos requisitos para a obtenção do Grau de MESTRE EM ENGENHARIA DE ESTRUTURAS na área de Estruturas.

Abrindo a sessão, o Presidente da Comissão, **Prof. Dr. Carlos Alberto Cimini Jr**, após dar a conhecer aos presentes o teor das Normas Regulamentares passou a palavra ao candidato para apresentação de seu trabalho. Seguiu-se a argüição pelos examinadores, com a respectiva defesa do candidato. Logo após, a Comissão se reuniu, sem a presença do candidato e do público, para julgamento e expedição do resultado final. Foram atribuídas as seguintes indicações:

Prof. Dr. Carlos Alberto Cimini Jr - DEES - UFMG (Orientador)
Prof. Dr. Túlio Hallak Panzera - UFSJ
Prof. Dr. Murilo Sartorato - UNESP

Pelas indicações acima, o candidato foi considerado APROVADO, conforme pareceres em anexo.

O resultado final foi comunicado publicamente ao candidato pelo Presidente da Comissão. Nada mais havendo a tratar, o Presidente encerrou a reunião e lavrou a presente ATA, que será assinada por todos os membros participantes da Comissão Examinadora.

Belo Horizonte, 03 de março de 2021 de 2020.

Observações:

1. A aprovação do candidato na defesa da Dissertação de Mestrado não significa que o mesmo tenha cumprido todos os requisitos necessários para obtenção do Grau de Mestre em Engenharia de Estruturas;

2. Este documento não terá validade sem a assinatura do Coordenador do Programa de Pós-Graduação.

Documento assinado eletronicamente por **Carlos Alberto Cimini Junior**, **Professor do Magistério Superior**, em 03/03/2021, às 18:42, conforme horário oficial de Brasília, com fundamento no art. 5º do Decreto nº 10.543, de 13 de novembro de 2020.

Documento assinado eletronicamente por **Tulio Hallak Panzera**, **Usuário Externo**, em 04/03/2021, às 13:30, conforme horário oficial de Brasília, com fundamento no art. 5º do Decreto nº 10.543, de 13 de novembro de 2020.

Documento assinado eletronicamente por **Murilo Sartorato**, **Usuário Externo**, em 04/03/2021, às 13:41, conforme horário oficial de Brasília, com fundamento no art. 5º do Decreto nº 10.543, de 13 de novembro de 2020.

Documento assinado eletronicamente por **Marcelo Greco**, **Coordenador(a) de curso de pós-graduação**, em 06/09/2021, às 11:31, conforme horário oficial de Brasília, com fundamento no art. 5º do Decreto nº 10.543, de 13 de novembro de 2020.

A autenticidade deste documento pode ser conferida no site https://sei.ufmg.br/sei/controlador_externo.php?acao=documento_conferir&id_orgao_acesso_externo=0, informando o código verificador **0595565** e o código CRC **41B09A52**.

Referência: Processo nº 23072.210514/2021-66   SEI nº 0595565

To all children, who once said "I want to be a scientist when I grow up".

Acknowledgments

First and foremost, I would like to thank my advisor, Carlos Alberto **Cimini** Jr., for all his help and support, even if not directly related to academic issues. Thank you for being a role model for me. You rock!

I am deeply grateful to my parents for allowing me to follow my dream. I know of all sacrifices you made that allowed me to finish this stage. You are my heroes.

To Patrícia, for all support, care and patient. I also thank you for all lovely and happy moments that made this journey more peaceful. You are my strength.

To my brother, for always supporting me.

To all my friends, specially to my long-time friends Vítor, Filipe, Comotti, Max, and Lucas Tadeu. I also thank my friends Shaw and Pedro from 101. You are part of my journey.

To FAPEMIG for the financial support.

Somewhere, something incredible is waiting to be known.

Carl Sagan

Resumo

Avanços nas técnicas de manufatura têm permitido mais flexibilidade no projeto e novas possibilidades para aplicar materiais compósitos em estruturas leves. Novas técnicas como automated fiber placement (AFP) possibilitam que as fibras percorram caminhos curvos, sendo assim possível laminados que apresentem propriedades que variam no plano do laminado. Estes tipos de laminados são conhecidos como laminados com rigidez variável ou variable angle tow (VAT). Neste trabalho, a resposta no plano e flambagem de painéis compósitos com rigidez variável por meio de uma variação espacial da orientação das fibras foi analisado para duas condições de contorno diferentes. Este trabalho compara o resultado da tensão no plano e carga crítica de flambagem para variações linear e cúbica do ângulo da fibra considerando quatro razões de aspecto. Restrições de manufatura foram consideradas na análise dos laminados. O método dos elementos finitos foi aplicado para resolver o sistema de equações parciais elípticas que governam o comportamento no plano destes painéis. O método de Ritz foi utilizado para encontrar a carga de flambagem dos painéis com rigidez variável. Resultados para quatro diferentes razões de aspecto são apresentados. Melhorias de até 18% na carga de flambagem foram encontradas em relação a variação linear da fibra.

Palavras-chave: Material Compósito; Compósitos *Variable Angle Tow*; Carga Crítica de Flambagem; Análise no Plano; *Automated Fiber Placement*.

Abstract

Advances in manufacturing techniques have allowed more flexibility to the design and new possibilities to apply composites materials in lightweight structures. Novel techniques such as the automated fiber placement allow the fibers to follow curvilinear paths, making possible laminate properties that vary within the laminate plane. These type of laminates are known as variable stiffness laminates or variable angle tow. In this work, the in-plane and buckling response of composite panels with variable stiffness through a spatially varying fiber orientation has been analyzed for two different boundary conditions. This work compares the outcomes of in-plane stress and critical buckling load for linear cubic fiber angle considering four aspect ratios. Manufacturing constraint has been considered in the analysis of the laminates. The finite element method has been applied to solve the system elliptic partial differential equations that govern the in-plane behavior of these panels. The Ritz method has been used to find the buckling loads for the variable stiffness panels. Results for four different aspects ratios are presented. Improvements in the buckling load of up to 18% over linear fiber angle variation were found.

Keywords: Composite Material; Variable Angle Tow Composites; Critical Buckling Load; In-plane Analysis; Automated Fiber Placement.

List of Figures

List of Tables

List of Symbols

x, y, z	Spatial coordinates
$1, 2, 3$	Local coordinates
θ	Lamina angle
$\theta(x, y)$	Fiber steering angle
d	Characteristic distance
T	Fiber angle at corresponding position
ϕ	Rotation angle
r	Steering radius
κ	Curvature
a	Length
b	Width
$\mathbf{c}$	Coefficients matrix
$\mathbf{a}$	Angle orientation vector
$\mathbf{x}$	Variable vector
σ	Stress tensor
C	Stiffness tensor
ϵ	Strain tensor
Q	Reduced stiffness in local coordinates
$\mathbf{Q}$	Reduced stiffness matrix in local coordinates
$\mathbf{T}$	Transformation matrix
$\bar{Q}$	Transformed reduced stiffness in spatial
$\bar{\mathbf{Q}}$	Transformed reduced stiffness matrix in spatial coordinates
γ	Shear strain
u	x direction displacement

u_0	Shortening load
v	y direction displacement
w	Out-of-plane displacement
h	Panel thickness
N_x, N_y, N_{xy}	In-plane stress resultant
M_x, M_y, M_{xy}	Bending moment resultant
N_{cr}	Normalized critical buckling load
E_x^{eq}	Equivalent panel stiffness

List of Abbreviations

AFP   Automated Fiber Placement

VAT   Variable Angle Tow

CLT   Classical Lamination Theory

PDE   Partial Differential Equation

FEM   Finite Element Method

SS   Simply Supported

Contents

Chapter 1

Introduction

Continuous-fiber composites materials have been widely used in many industries in the last years. These materials have begun to be used in military applications and then shifted to civil aerospace and automotive applications. Regarding these industries, the aerospace industry is the one that most uses this material. It is said that continuous-fiber composites are one of the most important classes of engineering materials, being the second one, only behind steel in industrial importance and range of applications (CLYNE; HULL, 2019). Modern aircraft, such as Boeing 787 and Airbus A350 XWB, has been successfully applied advanced continuous-fiber composite materials. The last one, for instance, has predominantly a composite airframe with 53% of its structure weight manufactured of composite materials, distributed over the wings, fuselage and other primary aerostructures (MARSH, 2010). This suggests that composite materials will be even more applied in the aerospace industry in the following decades.

The main advantage of this category of material is its superior strength to weight and stiffness to weight ratios compared to isotropic materials, allowing significant mass reduction. Besides that, but no less important, are the orthotropic properties of a single composite lamina, which brings together with other laminae, tailoring the stiffness to best respond to loading conditions in a specific component. Consequently, the design of composite structures involves more design variables than the design of isotropic structures. However, the project of continuous-fiber composites structures has historically been conservative, pointing out that there is more capacity of these materials yet to take advantage of them.

The growing in composite applications motivated by commercial interests has encouraged significant developments in manufacturing processes and structures design. The automated fiber placement (AFP) machines, for example, is a technology that has been developed over the past thirty years to attempt the industrial demands for fast manufacturing processes, as well as great flexibility to build composite laminates with complex geometries (NIK et al., 2014). The development of this new technology provided novel design approaches. Unlike traditional composite laminates with unidirectional fibers orien-
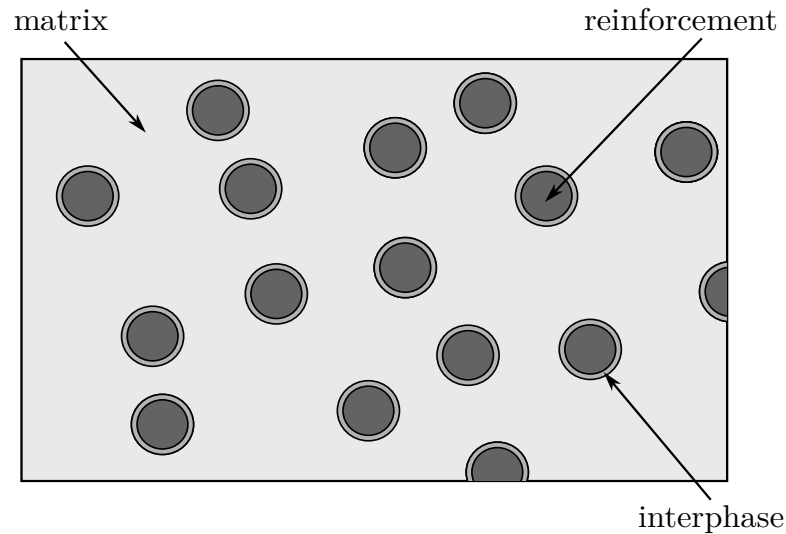
Figure 1.1: Phases of a composite material.

tation, variable angle tow (VAT) composite laminates, as known as tow-steered laminates (STODIECK et al., 2013), have a continuously varying fiber orientation, yielding a variable stiffness laminate. These type of laminates expand the design space to create more flexible and efficient structures. The VAT composite laminates will be introduced with more details later in this chapter, as well as AFP machines and a brief introduction of composite materials. This work examines the in-plane behavior of VAT composites and confirms the benefits that can be achieved by using this kind of composites for buckling applications.

1.1   A Brief Introduction to Composite Materials

As described by Vasiliev & Morozov (2001), usually any material consisting of two or more components with different properties and distinct boundaries between the components can be referred to as a composite material. The constituents will have different physical properties that when combined create a material exhibiting superior properties to its constituents. Composite materials typically consist of a discontinuous, stiffer and stronger fibrous phase, called the reinforcement, and a continuous, less stiff, called the matrix. As a consequence of different chemical compositions, an inter-phase may exist between the reinforcement and matrix. This way, the properties of a composite material depend on the physical and chemical properties of its constituents. The phases of a typical composite material are shown simplistically in Fig. 1.1.

Continuous reinforcement fibers are generally the one most used in the aerospace applications, known as fiber-reinforced composites. The role of the fibers is to carry loads and provide strength and stiffness. The matrix has to bond the fibers together and provide stress transfer between the fibers. Carbon and glass fibers are the most commonly used
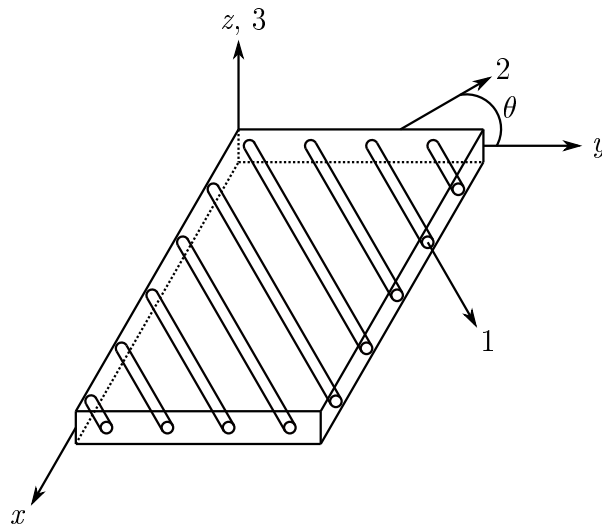
Figure 1.2: A single fiber-reinforced lamina.

reinforcements in the aerospace industry. Thermoset and thermoplastic polymer resins are normally used as the matrix material (JONES, 1998). A traditional fiber-reinforced lamina is shown in Fig. 1.2.

The mechanical response of a fiber-reinforced lamina shown in Fig. 1.2 can be expressed in two different coordinate systems, $x - y$ and $1 - 2$. In the coordinate system $1 - 2$, the $1-$axis is defined as the direction parallel to the fibers and the $2-$axis is defined as perpendicular to the $1-$axis, in the plane of the lamina. The stiffness and strength parameters of the lamina are always referred to the $1 - 2$ coordinate system. Stiffness properties in the fiber direction ($1-$axis) are usually an order of magnitude larger than in the transverse direction ($2-$axis). The $x - y$ system is parallel to the sides of the lamina and is the reference coordinate system for the applied loads. θ is the angle between the 1 direction and the x direction (or 2 direction and y direction), it is positive counterclockwise. A traditional laminate is made up of stacking multiple laminae bonded together, providing a composite part. The order that laminae are stacked is referred to as the laminate stacking sequence. This stacking sequence usually is designed according to each lamina angle θ of the laminate as $[\theta_1/\theta_2/, \ldots, \theta_N]$ (Fig. 1.3).

There are many manufacturing processes to obtain the final composite part. Typically, they consist of three steps: placing the fibrous material, impregnating it with resin and finally curing. Usually, the fiber is placed within a mold, which constitutes the shape of the part to be build. After the mold confection, the fibers are placed with the desired angle orientation at the designed location inside the mold. It is possible achieve this manually, denominated as hand-layup, or through automated mechanisms such as, filament winding, automated tape lying or automated fiber placement. The second step consists of impregnating the fibers with resin. The most commons methods are infusion or injection methods, such as resin transfer molding and injection molding. It is possible to achieve this step manually, but nowadays it is not typical. The last step is the cure of the matrix

Lamina $\longrightarrow$ Laminate $\longrightarrow$ Composite part

θ_1

$[\theta_1/\theta_2/\theta_3]$
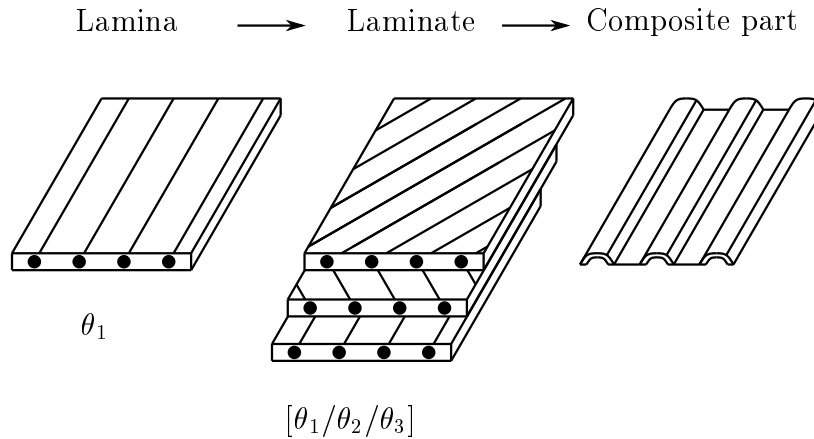
Figure 1.3: A group of laminae bonded together which, in turn, is integrated into a composite part.

material. This curing is commonly carried out in an autoclave at elevated temperatures and pressures.

Due to the high industrial demands for fast manufacturing and reducing costs, the goal of the industry is to achieve a reduction of processing time and wastes. To avoid the impregnating step, pre-impregnated fibers is used. In addition to reducing time, the cost is reduced caused by reduction of wasting. As a consequence of the high industrial demands to fast manufacturing and reducing costs, pre-impregnated (prepreg) fibers are used, avoiding the impregnating step. Prepeg fibers already contains the matrix material, this way the fibers do not need to be impregnated after the layup, it being possible cured just after the placement. Currently, the industry has dedicated efforts to advancing automated manufacturing technologies. These new technologies have opened space for novel approaches to structural designs, as will be explained later.

1.1.1 Challenges in Composite Design

The aerospace industry has been demonstrating that the use of composite materials is advantageous over metal-based materials. However, there are characteristics that may cause concerns and problems in composite design and analysis. The first one is to reliably predict the structural behavior of composites, in both stiffness and strength responses.

The orthotropy of the composite materials makes it more complicated to predict the strength response compared to isotropic, it depends on the stacking sequence. The presence of multiple materials, the relation between the interfaces (fiber-matrix and ply-ply) may create many different failure modes that normally is coupled. The second one is related to numerous options available to make the design and optimization more involved and the analysis more complex (BLOM, 2010; DANIEL; ISHAI, 2006).

It is essential to define a design space that can achieve a design practicable. The last one, but no less important, is the fabrication process. A variety of fabrication process exist,

each one is suitable for different applications. Fiber placement is a promissory manufacture process due to the fact it can provide high productivity and handle complex geometries (BLOM, 2010). Nowadays the fiber orientation can even be curved using fiber placement machines. Deep knowledge of the behavior of the composite structures is crucial to an excellent structural design using composite laminates.

1.2   Automated Fiber Placement

The quality and mechanical properties of a composite part are significantly depending on the placement and angle orientation of the fibers. With the advance of composite applications, the industry required fast and precise manufacturing. Hand-layup is a process dependent on high-skilled labor to precisely place the fibers. Besides that, it is both expensive and susceptible to fiber disposing and stacking errors, restricting the use of composites to only small secondary components. Impulsed by their high stiffness and strength to weight ratios, new automated manufacturing systems were developed. Thus, the continuous-fiber composite materials begin to be applied in primary structural components in the aerospace industry such as wing, fuselages and stabilators.

The initial AFP machines prototypes were developed based on the computer numerically controlled machines. They were commercially introduced around the end of the 1980s, and firstly implemented by an aerospace company, the Boeing Helicopters (DIRK; WARD; POTTER, 2012; EVANS, 1998). A schematic AFP machine head is shown in Fig. 1.4.

According to Brooks (2018), the AFP layup process works as follows: a continuous strip of resin-impregnated unidirectional fiber-reinforced tape (or tow) is fed into the machine head, where it is heated up and rolled down to bond it to the surface of the mold to define the structural shape. Currently AFP machines allow up to 32 individually tows, typically varying in width from 3.2 mm to 12.7 mm. These tows can be added or dropped at any point along the path of the machine head (DIRK; WARD; POTTER, 2012). This permits significant flexibility to layup complex geometries such as fuselage sections with window cut-outs (Fig. 1.5). Besides that, there is no constraint regarding that the tows paths must be straight, they also can be tow-steered, as shown in Fig. 1.6. The AFP machines have the ability to rotate and cut the tape during the layup process. The tow layup paths are defined automatically by a pre-set computer program (BROOKS, 2018). Some advantages regarding AFP, according to Smith & Grant (2006) are:

- Less man-hour per produced part.

- Reduction in wasted material during layup.

- Elimination of human-based error sources.

- Reduced requirement for in-process inspection

These factors lead to the adoption of the AFP process to be applied by many companies to fabricate their primary structures, as is shown in Tab. 1.1.

Table 1.1: Companies that utilized AFP process (GRANT, 2000).

Aircraft	Components
F-18 E/F	Inlet duct, aft center side skins, stabilator skins
C-17 Globemaster	Fan cowl doors, landing gear pods
Agusta 609	Fuselage panels
V-22 Osprey	Aft fuselage, side skins, sponsons, grips
Premier I	Fuselage sections
Hawker Horizon	Fuselage sections
F22 Raptor	Stabilator pivot shaft

1.2.1 Manufacturing Limitations

Any manufacturing process has its limitation and they should be taken into consideration when designing to avoid unexpected outcomes. Fiber path and geometry restrictions are some commons issues.

Minimum Turning Radius

An important constrain is known as minimum turning radius. When a fiber path is steered, the tows experience a in-plane deformation. This happen because the inner radius of a steered tow is smaller than the outer radius, consequently resulting in a tension force along the outer edge and a compressive force along the inner (Fig. 1.7). These fibers might start to buckling out-of-plane if the turning radius is too small. Consequently, a minimum turning radius (or maximum allowable curvature) is imposed, usually defined in terms of a minimum radius for the center-line of the course (BLOM, 2010). The out-of-plane displacements, as shown in Fig. 1.8, are undesirable since it affect the laminate properties.

Gaps and Overlaps

Gaps and overlaps may occur depending on how adjacent courses are disposed. To manufacture the laminate, the AFP machine head places the first course (reference path). At that point, the head is offset along an axis direction for placing the adjacent courses to cover the whole laminate. Depending on the offset value, gaps or overlaps may happen (FAYAZBAKHSH et al., 2013). Two approaches are usually used, which are known as the parallel and shifted path method (WALDHART, 1996). The shifted method consists of translating a reference path in order that the fiber angle orientation remains the same

Redirect
roller

Individual tow payout
with controlled tension

Clamp

Restart rollers

Compaction roller

Cutters

Controlled heat
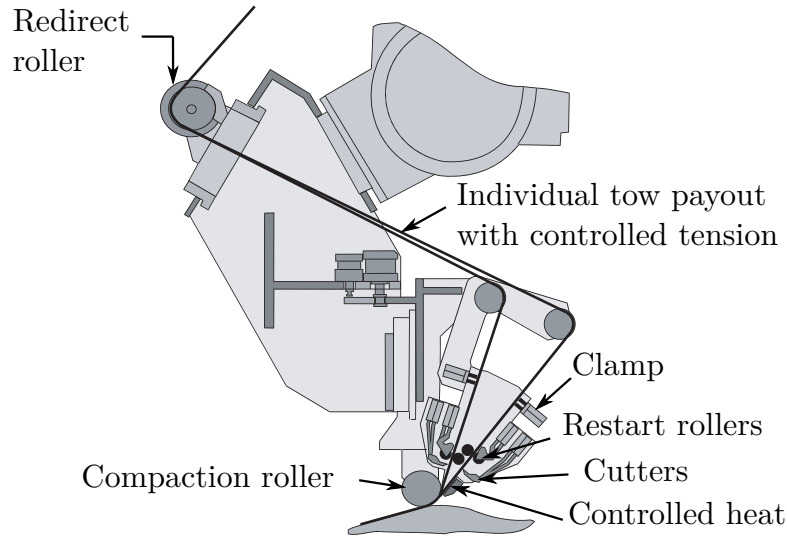
Figure 1.4: Fiber placement head (EVANS, 1998).

along an axis direction. The parallel method creates fibers path in a such manner that each path is defined as a constant distance from the reference path. A schematic representation of the both method is shown in Fig. 1.9. As can be seen in Fig. 1.9a, the parallel method prevents gaps and overlaps, but requires that the radius of curvature to achieve this, being susceptible to tow buckling. Gaps and overlaps as shown in Fig. 1.9b and Fig. 1.9c might cause a reduction in laminate quality.

Coverage parameter

The coverage parameter determines the degree to which a smooth boundary is covered by the discrete tows of the course. As the tows are cut perpendicular to the fiber direction, small gaps or overlaps are created. This concept is illustrated in Fig. 1.10. A boundary gap or overlap occurs when the material cannot perfectly meet the edge of a part when laying up the fiber path. This can result in either a shortage between the tow and the boundary edge or an excess material along the edge (HARIK et al., 2018). The gaps created cause resin-rich region, causing a weak area in the laminate. The overlaps lead to areas with larger thickness, which might influence the laminate strength.

1.2.2   The effect of defects on laminate behavior

As it was cited before, AFP machines induce defects which emerge during the manufacturing process (FAYAZBAKHSH, 2013). Thus, it is important to comprehend their impact on the mechanical properties of the final part. Sawicki & Minguett (1998) explored the effect of a gap width by means of the compression strength test. It is concluded that any gap size induced a strength decrease. Turoski (2000) conducted an experimental and numerical analysis to obtain the effect of the number of gaps for several mechanical properties,

Figure 1.5: Fiber placement machine laying on a fuselage section (source: Mtorres).

Figure 1.6: Steered fibers disposed by a AFP machine (source: Ingersoll Machine Tools).
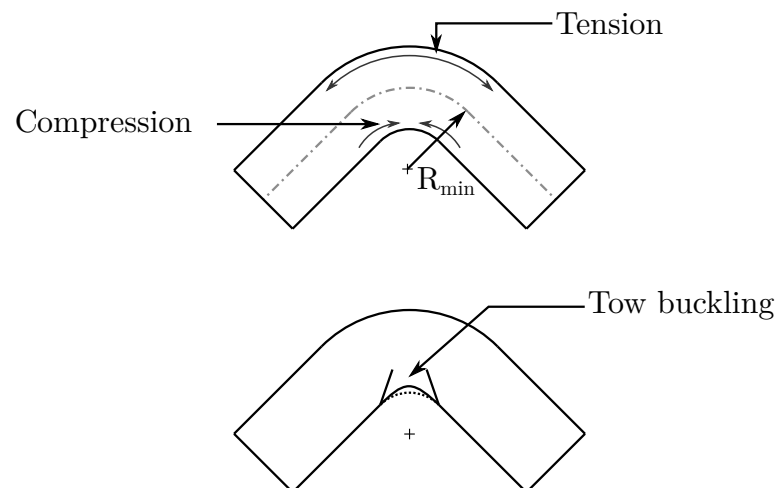
Figure 1.7: A minimum turning radius, $R_{\min}$, should be defined to avoid local fiber buckling due to in-plane compressive forces.
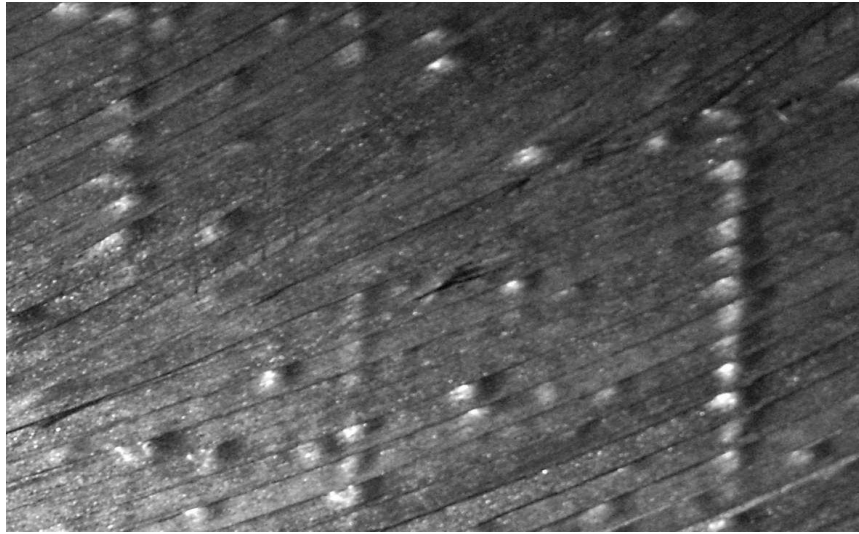
Figure 1.8: Buckled tows in a laminate with steered fiber courses (BLOM, 2010).

Decresing
radius of
curvature

Overlap

Gap

(a)   (b)   (c)
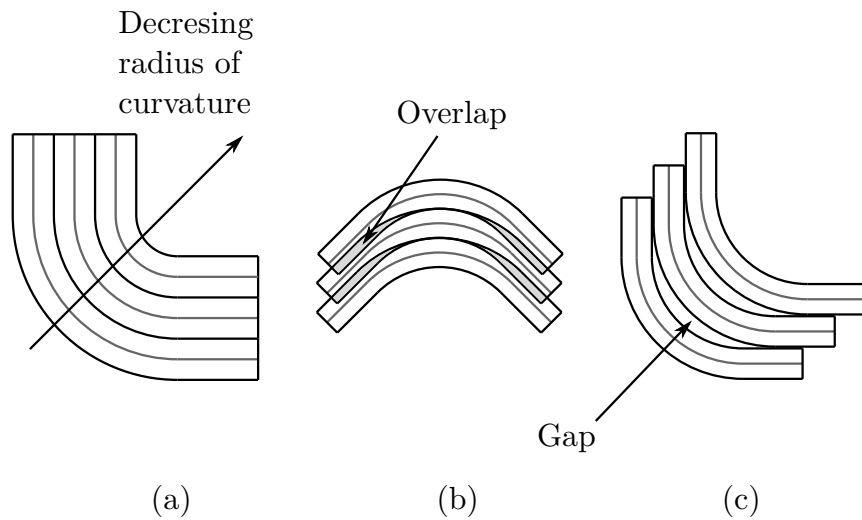
Figure 1.9: Schematic overview of two different path steering. (a) Parallel path. (b) Shifted path exhibiting overlaps. (c) Shifted path exhibiting gaps.

Boundary   Boundary   Boundary
curve   curve   curve

(a) 0% coverage   (b) 50% coverage   (c) 100% coverage
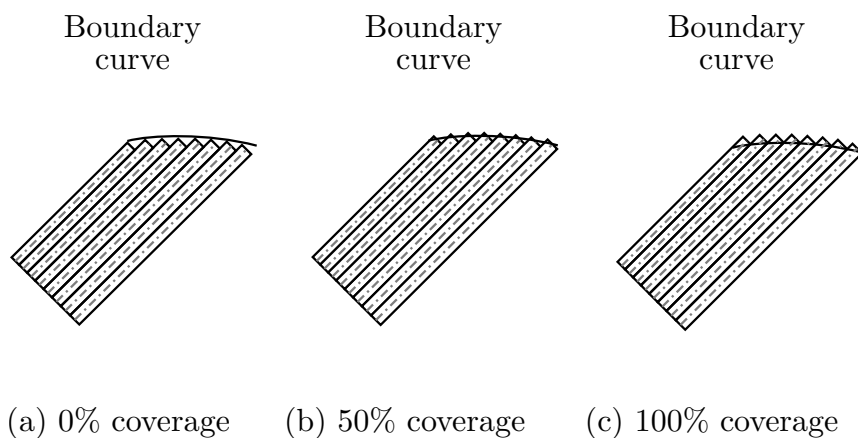
Figure 1.10: Tow drop locations with different coverage parameters. Adapted from Gurdal, Tatting & Wu (2005).

such as tension and compression for notched and unnotched quasi-isotropic laminates. It is concluded that in general, the unnotched specimens are more influenced by the defects than the notched specimens. Croft et al. (2011) studied the mechanical performance of laminates that are associated with AFP process induced defects such as gap, overlap, half gap/overlap and twisted tow. Their results show that the ultimate strength is less affected by different defect configurations at the lamina level than laminate, less than 5% and up to 13%, respectively. (FAYAZBAKHSH et al., 2012) show that a maximum improvement of 54% in the buckling load can be reached for a variable stiffness laminate following a complete overlap strategy. However, when gaps emerge in the laminates, the improvement in the buckling load reduces by 12%.

1.3   Variable Stiffness Laminates

Currently, the composite laminates applied in the aerospace industry consist of laminae with 0°, 90°, 45° and −45° (BLOM, 2010). The reason for this is due to early hand-layup manufacturing technique, as explained before. It would be hard and prone to errors align fibers in other directions. Besides that, a laminate made up of 0°, 90° and ±45° plies is appropriate to most load cases. The stiffness properties of these laminates are independent of spatial location being known as constant stiffness laminates. As a result of the automated manufacturing process, other angle orientations are possible, although there are "golden design rules" in the aerospace industry for using only 0°, 90°, ±45°. These "golden design rules" are based on many coupon tests. This way, it is necessary a strong reason, such as weight savings, for different angle orientations begin to be used in the aerospace industry.

A potential change in the application of fiber-reinforced composites is the concept of variable stiffness composites. Variable stiffness composites consist of plies that do not have a constant fiber orientation, the stiffness properties are a function of the spatial location. The stiffness variation might be discrete or continuous. Discrete variations consist of dividing the lamina into parts that present different angle orientations, while continuous variation consists of varying the fiber angle orientation continuously within the lamina's surface. These two approaches are shown in Fig. 1.11. Basically, continuous fiber variation is a generalization of discrete variations, which was possible due to the capability of automated fiber placement machines. This allows a vast range of possibilities to take into account the anisotropic properties of composites materials by steering fiber that it is possible obtain the desired stiffness at the desired location within a laminate, resulting in weight savings that traditional laminates cannot achieve. This kind of laminates is also referred to as tow-steered and variable angle tow composites in the literature. There are composites laminates fabricated with variable fiber volume fraction, internally dropped plies and with stiffeners which also are considered variable stiffness composites

(AKHAVAN, 2015), however, the focus of this research is on continuous fiber variation.

The initial work on variable stiffness composites was made by Gurdal & Olmedo (1993). Using a linear fiber angle variable, they showed that improvements on axial stiffness is possible for a laminate subject to uniform end shortening. Li, Kelly & Crosky (2002) applied the fiber steering concept to increase the performance of the bearing strength of bolted holes, and the fibres in this study were steered such that the fibres followed the principle tensile and compressive stress trajectories around the hole. A bolted joint in composite coupons has been strengthened by up to 169% for peak load or 36% for bearing strength using the modified steered pattern. Huang & Haftka (2005) have shown that increasing the load carrying capability of a composite plate with a hole in the center and loaded in tension results in a set of nearly concentric circles near the hole where the authors chose to limit the tailored region of the composite with a hole to the region close to the hole.

Buckling improvement of a component or structure using a variable stiffness composite has been the topic of several research efforts. Although significant increase in the buckling load can be obtained through tailoring laminate stacking sequence of composite panels with traditional straight fibers, the potential of fibrous composites is not fully exploited (SETOODEH et al., 2009). The improvement is attributed to the redistribution of in-plane loads to relatively stiff regions, and then resist buckling in critical regions (HAO et al., 2017b). An approach for the design of panels with cutouts was first introduced in the late eighties by Hyer & Charette (1991) in which curvilinear fibers were suggested to improve structural response instead of straight fiber paths.

Setoodeh et al. (2009) showed that variable stiffness composite is able to withstand more than twice the compressive load before buckling occurs compared to a quasi-isotropic composite panel. The paper has allowed for a better understanding of the load redistribution mechanism responsible for an increased buckling load. A buckling load increase of 33.9% with respect to a constant stiffness composite panel is reported in Lopes, Gürdal & Camanho (2008) for a variable stiffness composite panel where overlapping tows are present. Similar results for a clamped square variable stiffness composite panel were reported where an improvement of 66% in the buckling load is found for a simply supported composite panel. Tatting & Gurdal (2002) parameter based continuous curvilinear fiber path definition, in which fiber orientation angles vary linearly along the panel side, to design variable-stiffness panels with a center hole for maximum buckling load. Their study showed that up to 60% improvement can be gained by optimal design of panels while complying with the existing manufacturing techniques for curvilinear fibre paths. Brink, Vankan & Maas (2012) demonstrate that an improvement of buckling load ranging from 35% to 67% can be achieved by using a variable-stiffness design. Hao et al. (2017a) analyzed panel with multiple cutouts using a variable stiffness based on flow field function. They showed that improvements on buckling load is obtained when compared with linear

(a) Multi-parts   (b) Continuous fiber
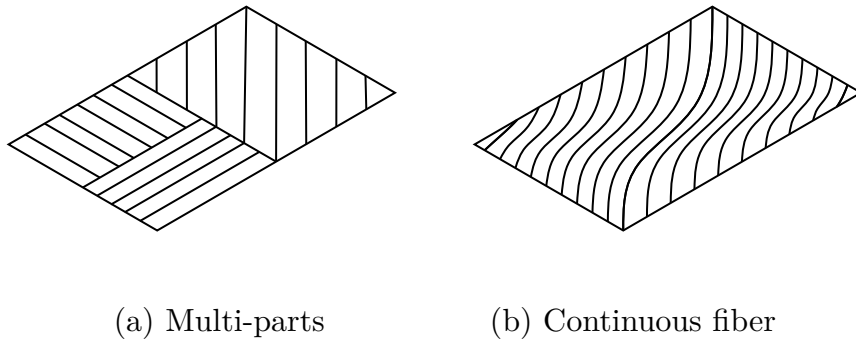
Figure 1.11: Schematic representation of discrete and continuous variable stiffness lamina.
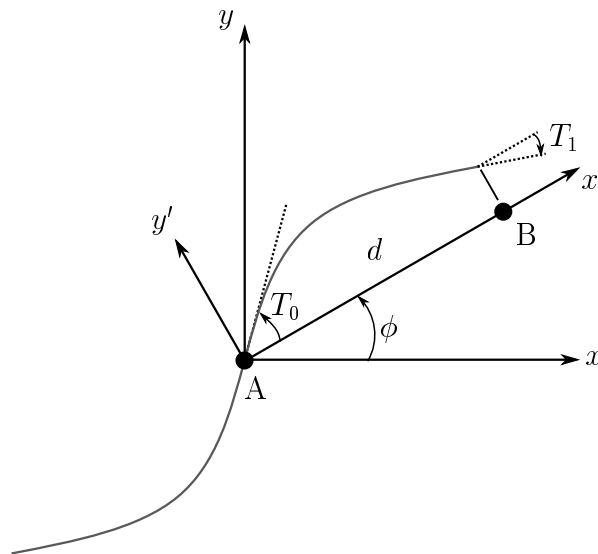
Figure 1.12: Path definition of a linear angle variation. Adapted from Gürdal, Tatting & Wu (2008).

angle variations and straight fibers.

1.3.1   Modeling of Variable Stiffness Laminates

In order to obtain and study variable stiffness laminates, it is required an approach to defining the stiffness variation within the lamina, which consists of defining the fiber trajectories in variable angle tow laminates. The most straightforward manner to define the fiber path orientation is to assume that the fiber angle orientation varies linearly in one direction between two reference points. This concept of a continuous, linear fiber angle variation along one direction with a ply to tailor the stiffness of a composite laminate was introduced by Gurdal & Olmedo (1993). After them, this approach was generalized by Tatting & Gurdal (2002), allowing the fiber to vary along any arbitrary axis, as shown in Fig. 1.12.

In Fig. 1.12, T_0 and T_1 are the defined fiber angle orientation at the reference points A and B, respectively, d is the characteristic distance between the reference points and ϕ is the rotation angle between the local coordinate system related to the global coordinate
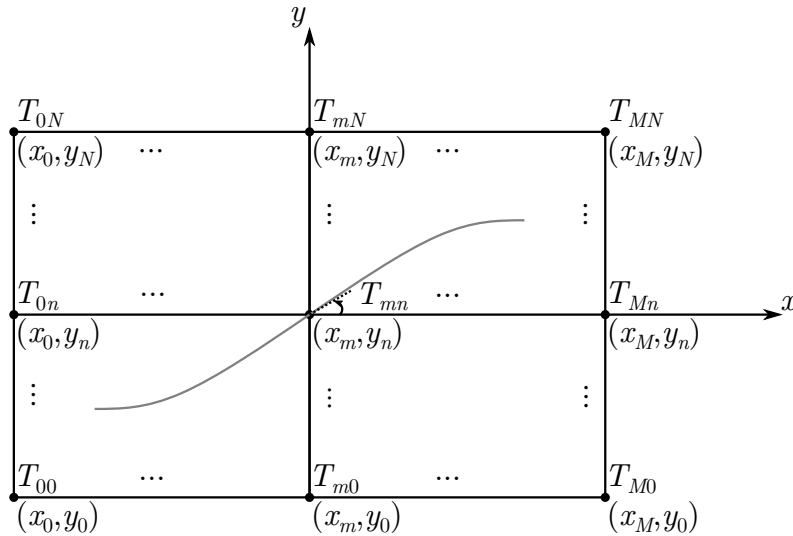
Figure 1.13: Schematic representation of a plate with a curvilinear path determined by $(M+1) \times (N+1)$ control points.

system. The fiber angle orientation concerning the coordinate system x' can be described as:

$$\theta(x') = \phi + (T_1 - T_0)\frac{|x'|}{d} + T_0 \tag{1.1}$$

Although the fiber orientation angle varies along a single axis, the fiber angle orientation can be decomposed into the $x - y$ plane. The notation to represent a single layer is written as $\phi\langle T_0|T_1\rangle$ (GÜRDAL; TATTING; WU, 2008). This way, there are three parameters to construct the laminates, ϕ, T_0 and T_1. From these parameters it is possible to generate laminates with a wide range of tailoring possibilities. One can construct laminates with different combinations of $\pm\phi$ angles and stacks of $\pm\langle T_0|T_1\rangle$. For example, a laminate with $\pm\phi \pm \langle T_0|T_1\rangle$ designation will have four curvilinear layers: a $\pm\langle T_0|T_1\rangle$ pair along $+\phi$ and a $\pm\langle T_0|T_1\rangle$ pair along $-\phi$ direction. It is also possible to model more complex fiber angle orientations such as non-linear variations, as cubic (PARNAS; ORAL; CEYHAN, 2003), Lagrangian polynomials (WU et al., 2012), trigonometric functions (ZHU et al., 2017), and Bezier curves (CAO; FU; HAN, 2019).

A common approach consists of using Lagrange's polynomials of various orders to interpolate the values of the so-called control angles assigned at a set of points within the lamina. A fiber value angle known as control angle, T_{mn}, is associated with each of these points. Thus, the fiber angle over a lamina $\theta(x, y)$ is interpolated from the control angles as shown in Eq. 1.2 (WU et al., 2012). A schematic representation is shown in Fig. 1.13.

$$\theta(x, y) = \sum_{m=0}^{M}\sum_{n=0}^{N} T_{mn} \prod_{m\neq i}\frac{x - x_i}{x_m - x_i} \prod_{n\neq j}\frac{y - y_j}{y_n - y_j} \tag{1.2}$$

This approach provides fiber paths with different polynomial degrees, providing high design flexibility. However, it has been shown that trajectories represented by high-order

polynomials can be difficult, or even impossible, to manufacture due to limitations of the manufacturing process, especially regarding the small radii curvature (PEREIRA, 2019). To avoid possible manufacturing defects, one can make a cubic fiber angle orientation, keeping certain design flexibility but adopting a less complex variation. A cubic fiber angle orientation can be defined as:

$$\theta\left(x'\right) = \phi + \left[\left(\mathbf{c}^{-1}\mathbf{a}\right)\right]^{T}|\mathbf{x}|' \tag{1.3}$$

$$\mathbf{c} = \begin{bmatrix} 0 & 0 & 0 & 1 \\ d^3/216 & d^2/36 & d/6 & 1 \\ d^3/27 & d^2/9 & d/3 & 1 \\ d^3/8 & d^2/4 & d/2 & 1 \end{bmatrix}, \mathbf{a} = \{T_0, T_1, T_2, T_3\}^T \text{ and } \mathbf{x} = \{x^3, x^2, x^1, x^0\}^T \tag{1.4}$$

where $\mathbf{c}$ is the matrix of coefficients, d is a characteristic distance between the position of the angle T_0 and T_3, $\mathbf{a}$ is the angle orientation vector and $\mathbf{x}$ is the variable vector related to the $x' - y'$ coordinate system rotated by an angle ϕ in relation to $x - y$ coordinate system, analogous to Eq. 1.1. For $\phi = 0$, for example, $d = a/2$. Besides that, when $\phi = 0°$, the angles T_0, T_1, T_2 and T_3 are located at $x = 0$, $x = a/6$, $x = a/3$ and $x = a/2$, respectively, where a is the panel length. Figure 1.14 shows the difference between a linear and cubic angle variation. The layer representation is defined as $\phi\langle T_0|T_1|T_2|T_3\rangle$, similar to the linear angle variation.

Once is defined the fiber angle orientation, the following relation can obtain the reference path of steered tow over the plane:

$$\frac{\mathrm{d}y'}{\mathrm{d}x'} = \tan\left(\theta(x')\right) \tag{1.5}$$

The first fiber path created is the reference fiber path. The next fiber path is made by shifting the reference fiber path a fixed amount in the y direction, for example, when $\phi = 0°$. The remaining fiber paths for the lamina are made in the same manner, with the only difference being the amount that each path is shifted along the shifting axis. This process is followed until all panel to be fully filled, as shown in Fig. 1.15, considering a linear angle variation and $\phi = 0$. The same idea can be extended to cubic angle variations and other values of ϕ.

As explained before, the manufacturing constraints of variable stiffness are related to the minimum steering radius that the AFP machine can perform. Defining the path reference, the steering radius can be obtained by inverting the tow path curvature κ, as defined in Eq. 1.6.

$$r = \frac{1}{\kappa} = \frac{\left[1 + \left(\dfrac{\mathrm{d}y'}{\mathrm{d}x'}\right)^2\right]^{3/2}}{\dfrac{\mathrm{d}^2 y'}{\mathrm{d}x'^2}} \tag{1.6}$$
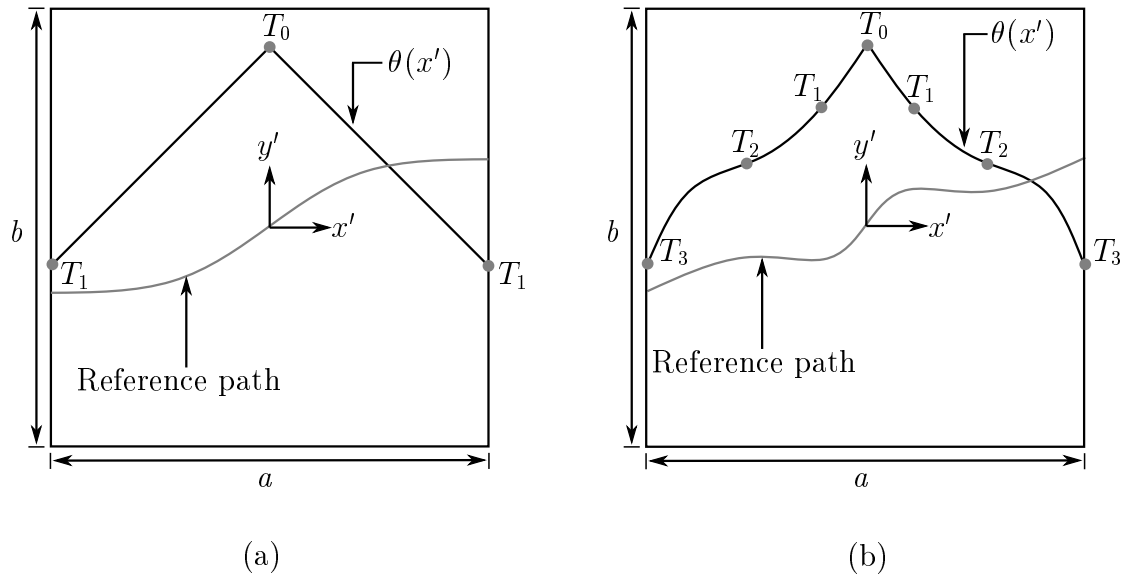
Figure 1.14: Composite plates presenting (a) linear angle variation and (b) cubic angle variation.
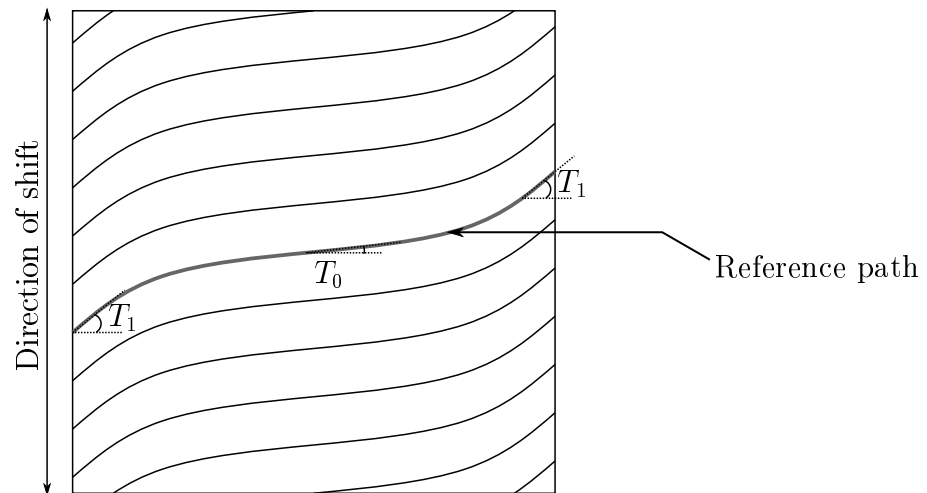
Figure 1.15: Shifting of reference path over the plate surface for a linear angle variation and $\phi = 0$.

1.4   Objectives

This dissertation aims to compare the in-plane and buckling response of panels that have a variable stiffness configuration considering a cubic and linear fiber angle variation. The main question is: does the cubic angle variation result in a higher buckling load when compared with linear angle variation? To answer this question, manufacturing constraints of VAT laminate regarding fiber steering radius inherent to AFP manufacturing process are considered in the analysis. The aim is to ensure that the panels satisfies existing limitations regarding fiber placement method. Two boundary conditions and four aspect ratios are studied.

Chapter 2

In-plane and buckling analysis

2.1 Laminate Theory

2.1.1 Lamina Constitutive Relations

In order to model the behavior of a laminated plate, it is necessary understand the response of a single lamina. The state of stress at a point in a general continuum (see Fig. 2.1) can be represented by the generalized Hooke's law (REDDY, 2007):

$$\sigma_{ij} = C_{ijkl}\epsilon_{kl} \qquad (i,j,k,l = 1,2,3) \tag{2.1}$$

where C_{ijkl} is a fourth-order stiffness tensor and ϵ_{kl} and σ_{ij} are second-order strain and stress tensors, respectively.

Equation 2.1 can be written in contracted notation as (JONES, 1998):

$$\sigma_i = C_{ij}\epsilon_j \qquad (i,j = 1,\ldots,6) \tag{2.2}$$
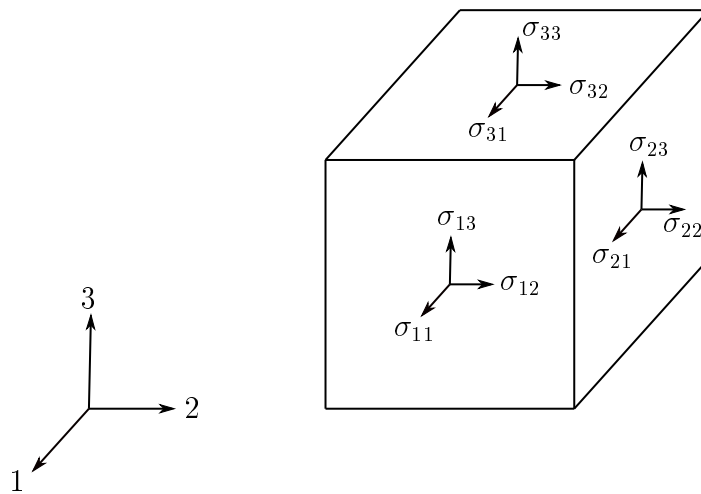
Figure 2.1: State of stress at a point of a continuum.

where σ_i are the stress components, C_{ij} is the stiffness matrix, and ϵ_j are the strain components. Energy considerations requires that $C_{ij} = C_{ji}$ (JONES, 1998). This way,

$$\begin{Bmatrix} \sigma_1 \\ \sigma_2 \\ \sigma_3 \\ \tau_4 \\ \tau_5 \\ \tau_6 \end{Bmatrix} = \begin{bmatrix} C_{11} & C_{12} & C_{13} & C_{14} & C_{15} & C_{16} \\ & C_{22} & C_{23} & C_{24} & C_{25} & C_{26} \\ & & C_{33} & C_{34} & C_{35} & C_{36} \\ & & & C_{44} & C_{45} & C_{46} \\ & & & & C_{55} & C_{56} \\ & \text{sym.} & & & & C_{66} \end{bmatrix} \begin{Bmatrix} \epsilon_1 \\ \epsilon_2 \\ \epsilon_3 \\ \gamma_4 \\ \gamma_5 \\ \gamma_6 \end{Bmatrix} \tag{2.3}$$

where

$$\begin{aligned} \sigma_1 &= \sigma_{11} & \sigma_2 &= \sigma_{22} & \sigma_3 &= \sigma_{33} \\ \tau_4 = \sigma_4 &= \sigma_{23} & \tau_5 = \sigma_5 &= \sigma_{31} & \tau_6 = \sigma_6 &= \sigma_{12} \end{aligned} \tag{2.4}$$

$$\begin{aligned} \epsilon_1 &= \epsilon_{11} & \epsilon_2 &= \epsilon_{22} & \epsilon_3 &= \sigma_{33} \\ \gamma_4 = \epsilon_4 &= \gamma_{23} = 2\epsilon_{23} & \gamma_5 = \epsilon_5 &= \gamma_{31} = 2\epsilon_{31} & \gamma_6 = \epsilon_6 &= \gamma_{12} = 2\epsilon_{12} \end{aligned} \tag{2.5}$$

Orthotropic materials have three mutually perpendicular planes of material symmetry. This implies that stiffness terms are interrelated (DANIEL; ISHAI, 2006). Then Eq. 2.3 can be rewritten as

$$\begin{Bmatrix} \sigma_1 \\ \sigma_2 \\ \sigma_3 \\ \tau_4 \\ \tau_5 \\ \tau_6 \end{Bmatrix} = \begin{bmatrix} C_{11} & C_{12} & C_{13} & 0 & 0 & 0 \\ & C_{22} & C_{23} & 0 & 0 & 0 \\ & & C_{33} & 0 & 0 & 0 \\ & & & C_{44} & 0 & 0 \\ & & & & C_{55} & 0 \\ & \text{sym.} & & & & C_{66} \end{bmatrix} \begin{Bmatrix} \epsilon_1 \\ \epsilon_2 \\ \epsilon_3 \\ \gamma_4 \\ \gamma_5 \\ \gamma_6 \end{Bmatrix} \tag{2.6}$$

As can be seen in Eq. 2.6, no coupling exists between normal stresses and shear strains, also no coupling exists between shear stresses and normal strains.

Fiber-reinforced composite materials are considered a orthotropic material. Besides that, in structural applications they are used in the form of thin laminates loaded in the plane (DANIEL; ISHAI, 2006). For this reason, they can be considered under a plane stress condition. Thus,

$$\sigma_3 = \tau_4 = \tau_5 = 0 \tag{2.7}$$

Substituting relations of Eq. 2.7 into Eq. 2.6 yields

$$\begin{Bmatrix} \sigma_1 \\ \sigma_2 \\ \tau_6 \end{Bmatrix} = \begin{bmatrix} Q_{11} & Q_{12} & 0 \\ Q_{12} & Q_{12} & 0 \\ 0 & 0 & Q_{66} \end{bmatrix} \begin{Bmatrix} \epsilon_1 \\ \epsilon_2 \\ \gamma_6 \end{Bmatrix} \tag{2.8}$$

where the reduced stiffness matrix components Q_{ij} are

$$Q_{ij} = C_{ij} - \frac{C_{i3}C_{j3}}{C_{33}} \qquad (i, j = 1, 2, 6) \tag{2.9}$$

The relations between mathematical and engineering constants are given by (DANIEL; ISHAI, 2006)

$$
\begin{aligned}
Q_{11} &= \frac{E_1}{1 - \nu_{12}\nu_{21}} \\
Q_{22} &= \frac{E_2}{1 - \nu_{12}\nu_{21}} \\
Q_{12} &= \frac{\nu_{21}E_1}{1 - \nu_{12}\nu_{21}} \\
Q_{66} &= G_{12}
\end{aligned} \tag{2.10}
$$

Usually, the lamina axes, $1 - 2$, do not coincide with the reference axes, $x - y$, or the loading. It is desirable to refer the strain and strain in term of the loading axes. Let the $1 - 2$ system be rotated by a angle θ from $x - y$ system, as shown in Figure 2.2. The resulting stresses and strains in $x - y$ plane is given by Eq. 2.11 (DANIEL; ISHAI, 2006).

$$
\begin{Bmatrix} \sigma_x \\ \sigma_y \\ \tau_{xy} \end{Bmatrix} = \begin{bmatrix} \bar{Q}_{11} & \bar{Q}_{12} & \bar{Q}_{16} \\ \bar{Q}_{12} & \bar{Q}_{22} & \bar{Q}_{26} \\ \bar{Q}_{16} & \bar{Q}_{22} & \bar{Q}_{66} \end{bmatrix} \begin{Bmatrix} \epsilon_x \\ \epsilon_y \\ \gamma_{xy} \end{Bmatrix} \tag{2.11}
$$

$\bar{Q}_{ij}$ is the transformed reduced stiffness matrix and is determined from the stiffness matrix, Q_{ij}, and the fiber orientation angle, θ.

$$
\begin{aligned}
\bar{Q}_{11} &= Q_{11}\cos^4\theta + 2(Q_{12} + 2Q_{66})\sin^2\theta\cos^2\theta + Q_{22}\sin^4\theta \\
\bar{Q}_{12} &= (Q_{11} + Q_{22} - 4Q_{66})\sin^2\theta\cos^2\theta + Q_{12}(\sin^4\theta + \cos^4\theta) \\
\bar{Q}_{22} &= Q_{11}\sin^4\theta + 2(Q_{12} + 2Q_{66})\sin^2\theta\cos^2\theta + Q_{22}\cos^4\theta \\
\bar{Q}_{16} &= (Q_{11} - Q_{12} - 2Q_{66})\sin\theta\cos^3\theta + (Q_{12} - Q_{22} + 2Q_{66})\sin^3\theta\cos\theta \\
\bar{Q}_{26} &= (Q_{11} - Q_{12} - 2Q_{66})\sin^3\theta\cos\theta + (Q_{12} - Q_{22} + 2Q_{66})\sin\theta\cos^3\theta \\
\bar{Q}_{66} &= (Q_{11} + Q_{22} - 2Q_{12} - 2Q_{66})\sin^2\theta\cos^2\theta + Q_{66}(\sin^4\theta + \cos^4\theta)
\end{aligned} \tag{2.12}
$$
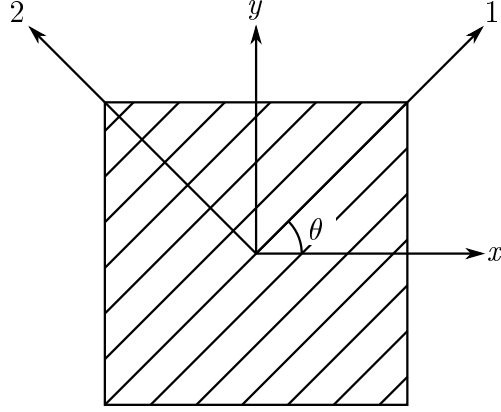
Figure 2.2: Transforming 1-2 properties into x-y coordinates.

It is possible to rewrite these relations using trigonometric identities, yielding

$$
\begin{aligned}
\bar{Q}_{11} &= U_1 + U_2 \cos(2\theta) + U_3 \cos(4\theta) \\
\bar{Q}_{12} &= U_4 - U_3 \cos(4\theta) \\
\bar{Q}_{16} &= \frac{1}{2} U_2 \sin(2\theta) + U_3 \sin(4\theta) \\
\bar{Q}_{22} &= U_1 - U_2 \cos(2\theta) + U_3 \cos(4\theta) \\
\bar{Q}_{26} &= \frac{1}{2} \sin(2\theta) - U_3 \sin(4\theta) \\
\bar{Q}_{66} &= U_5 - U_3 \cos(4\theta)
\end{aligned}
\tag{2.13}
$$

where U_1, U_2, U_3, U_4, and U_5 are the material invariants. They are defined as,

$$
\begin{aligned}
U_1 &= \frac{3Q_{11} + 3Q_{22} + 2Q_{12} + 4Q_{66}}{8} \\
U_2 &= \frac{Q_{11} - Q_{22}}{2} \\
U_3 &= \frac{Q_{11} + Q_{22} - 2Q_{12} - 4Q_{66}}{8} \\
U_4 &= \frac{Q_{11} + Q_{22} + 6Q_{12} - 4Q_{66}}{8} \\
U_5 &= \frac{Q_{11} + Q_{22} - 2Q_{12} + 4Q_{66}}{8}
\end{aligned}
\tag{2.14}
$$

The strains in Eq. 2.11 are given by the linear strain-displacement relationship

$$
\left\{ \begin{array}{c} \epsilon_x \\ \epsilon_y \\ \gamma_{xy} \end{array} \right\} = \left\{ \begin{array}{c} \frac{\partial u}{\partial x} \\ \frac{\partial v}{\partial y} \\ \frac{\partial u}{\partial y} + \frac{\partial v}{\partial x} \end{array} \right\}
\tag{2.15}
$$

The above constitutive relations is applied for a lamina that exhibits straight fiber. However, they can be applied to curvilinear fibers too. As shown before, the fiber angle

variation is defined as a function of x and y, or only x, for the simplest cases. Thus, the reduced stiffness matrix can be defined as function of x and y as, $\bar{Q}_{ij} = \bar{Q}_{ij}(\theta) = \bar{Q}_{ij}(x, y)$. Equation 2.11 can be written as

$$\begin{Bmatrix} \sigma_x \\ \sigma_y \\ \tau_{xy} \end{Bmatrix} = \begin{bmatrix} \bar{Q}_{11}(x,y) & \bar{Q}_{12}(x,y) & \bar{Q}_{16}(x,y) \\ \bar{Q}_{12}(x,y) & \bar{Q}_{22}(x,y) & \bar{Q}_{26}(x,y) \\ \bar{Q}_{16}(x,y) & \bar{Q}_{22}(x,y) & \bar{Q}_{66}(x,y) \end{bmatrix} \begin{Bmatrix} \epsilon_x \\ \epsilon_y \\ \gamma_{xy} \end{Bmatrix} \tag{2.16}$$

The strain-displacement relations remain the same.

2.1.2 Classical Lamination Theory

The elastic behavior of thin composite plates is a function of the properties and stacking sequence of the individual layers. The Classical Lamination Theory (CLT) is used to predicts the response of laminates considering that the bonds between layers, it is thin with its lateral dimensions much larger than its thickness and the straight lines normal to the laminate mid-plane remain straight and normal after deformation. Additional assumptions can be seen in Daniel & Ishai (2006), Jones (1998), Whitney (1987). According to Jones (1998) and Whitney (1987), the response of convectional thin composite plates, with constant stiffness, can be accurately obtained by using CLT. The displacements at any point within the laminate are given by

$$\begin{aligned} u &= u^0 - z\frac{\partial w}{\partial x} \\ v &= v^0 - z\frac{\partial w}{\partial y} \\ w &= w^0 \end{aligned} \tag{2.17}$$

where the terms u^0, v^0, and w^0 are the axial, transverse, and out-of-plane mid-plane displacement, respectively. The partial derivatives with respect to w denote the rotations of the mid-plane. Substituting Eq. 2.17 into Eq. 2.16 results in the following constitutive relation for the kth layer,

$$\begin{Bmatrix} \sigma_x \\ \sigma_y \\ \tau_{xy} \end{Bmatrix}_k = \begin{bmatrix} \bar{Q}_{11}(x') & \bar{Q}_{12}(x') & \bar{Q}_{16}(x') \\ \bar{Q}_{12}(x') & \bar{Q}_{22}(x') & \bar{Q}_{26}(x') \\ \bar{Q}_{16}(x') & \bar{Q}_{26}(x') & \bar{Q}_{66}(x') \end{bmatrix}_k \begin{Bmatrix} \epsilon_x^0 + z\kappa_x \\ \epsilon_y^0 + z\kappa_y \\ \gamma_{xy}^0 + z\kappa_{xy} \end{Bmatrix} \tag{2.18}$$

where

$$\kappa_x = -\frac{\partial^2 w}{\partial x^2}$$
$$\kappa_y = -\frac{\partial^2 w}{\partial y^2} \tag{2.19}$$
$$\kappa_{xy} = -\frac{\partial^2 w}{\partial x \partial y}$$

The CLT consider the stress and moment resultants to define the stress state for the laminate. The stress results is given by the average stress per unit length at different points in the laminate. It can be written as,

$$\begin{Bmatrix} N_x \\ N_y \\ N_{xy} \end{Bmatrix} = \int_{-h/2}^{h/2} \begin{Bmatrix} \sigma_x \\ \sigma_y \\ \tau_{xy} \end{Bmatrix} dz = \sum_{k=1}^{N} \int_{z_{k-1}}^{z_k} \begin{Bmatrix} \sigma_x \\ \sigma_y \\ \tau_{xy} \end{Bmatrix} dz \tag{2.20}$$

where h is laminate thickness. Similarly, the moment resultants are obtained by integrating the stress resultant through the thickness of laminate, resulting in a bending moment per unit length,

$$\begin{Bmatrix} M_x \\ M_y \\ M_{xy} \end{Bmatrix} = \int_{-h/2}^{h/2} \begin{Bmatrix} \sigma_x \\ \sigma_y \\ \tau_{xy} \end{Bmatrix} z dz = \sum_{k=1}^{N} \int_{z_{k-1}}^{z_k} \begin{Bmatrix} \sigma_x \\ \sigma_y \\ \tau_{xy} \end{Bmatrix} z dz \tag{2.21}$$

The positive direction for the stress and moment resultants acting on a plate element are shown in Fig. 2.3. By using the stress-strain relations, the stress and moment resultants can be expressed in terms of the mid-plane values of strain and curvature by substituting the Eq. 2.18 into Eqs. 2.20 and 2.21. In this manner, the stress and moment resultants can be defined by the stiffness matrix, $\mathbf{A}$, the coupling stiffness matrix, $\mathbf{B}$, and the bending stiffness matrix, $\mathbf{D}$, as follows:

$$\begin{Bmatrix} N_x \\ N_y \\ N_{xy} \end{Bmatrix} = \begin{bmatrix} A_{11} & A_{12} & A_{16} \\ A_{12} & A_{12} & A_{26} \\ A_{16} & A_{26} & A_{66} \end{bmatrix} \begin{Bmatrix} \epsilon_x^0 \\ \epsilon_y^0 \\ \gamma_{xy}^0 \end{Bmatrix} + \begin{bmatrix} B_{11} & B_{12} & B_{16} \\ B_{12} & B_{12} & B_{26} \\ B_{16} & B_{26} & B_{66} \end{bmatrix} \begin{Bmatrix} \kappa_x \\ \kappa_y \\ \kappa_{xy} \end{Bmatrix} \tag{2.22}$$

$$\begin{Bmatrix} M_x \\ M_y \\ M_{xy} \end{Bmatrix} = \begin{bmatrix} B_{11} & B_{12} & B_{16} \\ B_{12} & B_{12} & B_{26} \\ B_{16} & B_{26} & B_{66} \end{bmatrix} \begin{Bmatrix} \epsilon_x^0 \\ \epsilon_y^0 \\ \gamma_{xy}^0 \end{Bmatrix} + \begin{bmatrix} D_{11} & D_{12} & D_{16} \\ D_{12} & D_{12} & D_{26} \\ D_{16} & D_{26} & D_{66} \end{bmatrix} \begin{Bmatrix} \kappa_x \\ \kappa_y \\ \kappa_{xy} \end{Bmatrix} \tag{2.23}$$
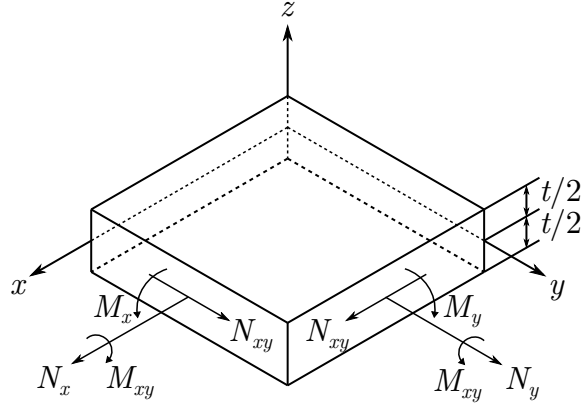
Figure 2.3: Element of a single layer with force and moment resultants. Adapted from Daniel & Ishai (2006).
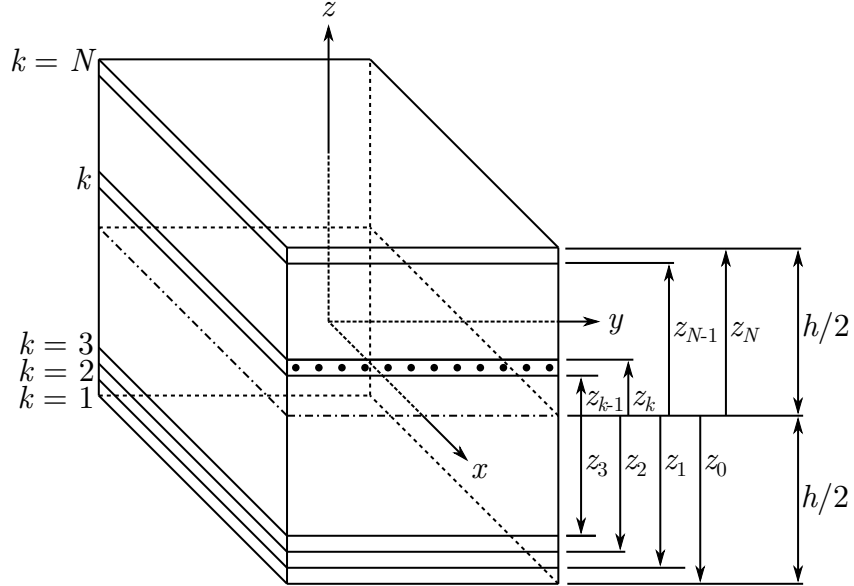
Figure 2.4: Multi-directional laminate with coordinate notation of individual plies. Adapted from Daniel & Ishai (2006).

where

$$A_{ij} = \sum_{k=1}^{N} (\bar{Q}_{ij})_k (z_k - z_{k-1})$$

$$B_{ij} = \frac{1}{2} \sum_{k=1}^{N} (\bar{Q}_{ij})_k (z_k^2 - z_{k-1}^2) \tag{2.24}$$

$$D_{ij} = \frac{1}{3} \sum_{k=1}^{N} (\bar{Q}_{ij})_k (z_k^3 - z_{k-1}^3)$$

TSAI & HAHN (1980) have proposed a method for calculating the matrices **A**, **B**,

and **D** by using the material invariants. The **A**, **B**, and **D** are expressed as,

$$[\mathbf{A}, \mathbf{B}, \mathbf{D}] = \begin{bmatrix} U_1 V_0 + U_2 V_1 + U_3 V_3 & U_4 V_0 - U_3 V_3 & (1/2)U_2 V_2 + U_3 V_4 \\ U_4 V_0 - U_3 V_3 & U_1 V_0 - U_2 V_1 + U_3 V_3 & (1/2)U_2 V_2 - U_3 V_4 \\ (1/2)U_2 V_2 + U_3 V_4 & (1/2)U_2 V_2 - U_3 V_4 & U_5 V_0 - U_3 V_3 \end{bmatrix} \quad (2.25)$$

where

$$V_{0\{A,B,D\}} = \left\{ h, 0, \frac{h^3}{12} \right\}$$

$$V_{1\{A,B,D\}} = \int_{-\frac{h}{2}}^{\frac{h}{2}} \cos(2\theta)\{1, z, z^2\}\mathrm{d}z$$

$$V_{2\{A,B,D\}} = \int_{-\frac{h}{2}}^{\frac{h}{2}} \sin(2\theta)\{1, z, z^2\}\mathrm{d}z \quad (2.26)$$

$$V_{3\{A,B,D\}} = \int_{-\frac{h}{2}}^{\frac{h}{2}} \cos(4\theta)\{1, z, z^2\}\mathrm{d}z$$

$$V_{4\{A,B,D\}} = \int_{-\frac{h}{2}}^{\frac{h}{2}} \sin(4\theta)\{1, z, z^2\}\mathrm{d}z$$

2.1.3   Special Cases of Laminates

The symmetry or antisymmetry of a laminate, based on angle, material, and thickness of plies, may zero out some elements of the matrices A_{ij}, B_{ij}, and D_{ij}. The following definitions are based on Kaw (2005).

- Symmetric laminate: It has the material, angle, and thickness of plies are the same above or below the mid-plane. For symmetric laminates, $B_{ij} = 0$. A symmetric laminate is represented by a subscript s. As example of a laminate is a $[\theta_1/\theta_2]_s = [\theta_1/\theta_2/\theta_2/\theta_1]$.

- Cross-Ply laminate: It has only $0°$ and $90°$ plies were used to make a laminate. An example is the laminate $[0°/90°/0°/90°]$. For cross-ply laminates, A_{16}, A_{26}, B_{16}, B_{26}, D_{16}, and D_{26} are equal to zero.

- Angle-Ply laminate: It has plies of the same material and thickness and only oriented at θ and $-\theta$ directions. An example of an angle ply laminate is $[-\theta/\theta/-\theta/\theta]$. If a laminate has an even number of plies, then $A_{16} = A_{26} = 0$. However, if the number of plies is odd and it consists of alternating θ and $-\theta$ plies, then it is symmetric, giving $B_{ij} = 0$, and A_{16}, A_{26}, D_{16}, and D_{26} also become small as the number of layers increases for the same laminate thickness.

- Balanced laminate: It has angles other than $0°$ and $90°$ and they occur only as plus and minus pairs of θ and $-\theta$. The plus and minus pairs do not need to be adjacent

to each other, but the thickness and material of the plus and minus pairs need to be the same. Here, the terms $A_{16} = A_{26} = 0$. An example of a balanced laminate is $[\theta_1/\theta_2/-\theta_1/\theta_1/-\theta_1/-\theta_2]$.

For certain structural applications, the in-plane/flexure coupling, relating in-plane loads to curvatures and moments to in-plane strains, promoted by B_{ij} is undesirable. To avoid this kind of behavior, a symmetric laminate is used. For some applications is also desirable to avoid anisotropy extensional/bending coupling related to the terms A_{12}, A_{26}. It can be achieve using balanced laminate. Further discussions can be found in Caprino & Visconti (1982). For symmetric, angle-ply, and balanced laminates, $[\pm\theta]_{\text{ns}}$, $B_{ij} = 0$, and $A_{16} = A_{26} = 0$. Therefore, the constitutive relations reduce to

$$\begin{Bmatrix} N_x \\ N_y \\ N_{xy} \end{Bmatrix} = \begin{bmatrix} A_{11} & A_{12} & 0 \\ A_{12} & A_{22} & 0 \\ 0 & 0 & A_{66} \end{bmatrix} \begin{Bmatrix} \epsilon_x^0 \\ \epsilon_y^0 \\ \gamma_{xy}^0 \end{Bmatrix} \tag{2.27}$$

$$\begin{Bmatrix} M_x \\ M_y \\ M_{xy} \end{Bmatrix} = \begin{bmatrix} D_{11} & D_{12} & D_{16} \\ D_{12} & D_{22} & D_{26} \\ D_{16} & D_{26} & D_{66} \end{bmatrix} \begin{Bmatrix} \kappa_x \\ \kappa_y \\ \kappa_{xy}^0 \end{Bmatrix} \tag{2.28}$$

where $A_{ij} = A_{ij}(x, y)$ and $D_{ij} = D_{ij}(x, y)$ for VAT laminates.

2.1.4 Effective Material Properties

By using CLT applied to VAT composites, it is convenient to analyze the stiffness of the panel by means of effective materials properties similar to E_1, E_2, G_{12}, ν_{12}, and ν_{21}. Considering a symmetric laminate, $B_{ij} = 0$. Then, Eq. 2.22 can be rewrite in terms of the strains as

$$\begin{Bmatrix} \epsilon_x^0 \\ \epsilon_y^0 \\ \gamma_{xy}^0 \end{Bmatrix} = \frac{1}{\psi} \begin{bmatrix} A_{22}A_{66} - A_{26}^2 & A_{16}A_{26} - A_{12}A_{66} & A_{12}A_{26} - A_{16}A_{22} \\ A_{16}A_{26} - A_{12}A_{66} & A_{11}A_{66} - A_{16}^2 & A_{12}A_{16} - A_{11}A_{26} \\ A_{12}A_{26} - A_{16}A_{22} & A_{12}A_{16} - A_{11}A_{26} & A_{11}A_{22} - A_{12}^2 \end{bmatrix} \begin{Bmatrix} N_x \\ N_y \\ N_{xy} \end{Bmatrix} \tag{2.29}$$

where

$$\psi = -A_{66}A_{12}^2 + 2A_{16}A_{26}A_{12} - A_{11}A_{26}^2 - A_{16}^2A_{22} + A_{11}A_{22}A_{66} \tag{2.30}$$

As N_x, N_y, and N_{xy} have the unit of force per unit of length, it is possible to define a pseudo-stress vector as,

$$\begin{Bmatrix} \sigma_x^* \\ \sigma_y^* \\ \tau_{xy}^* \end{Bmatrix} = \frac{1}{h} \begin{Bmatrix} N_x \\ N_y \\ N_{xy} \end{Bmatrix} \tag{2.31}$$
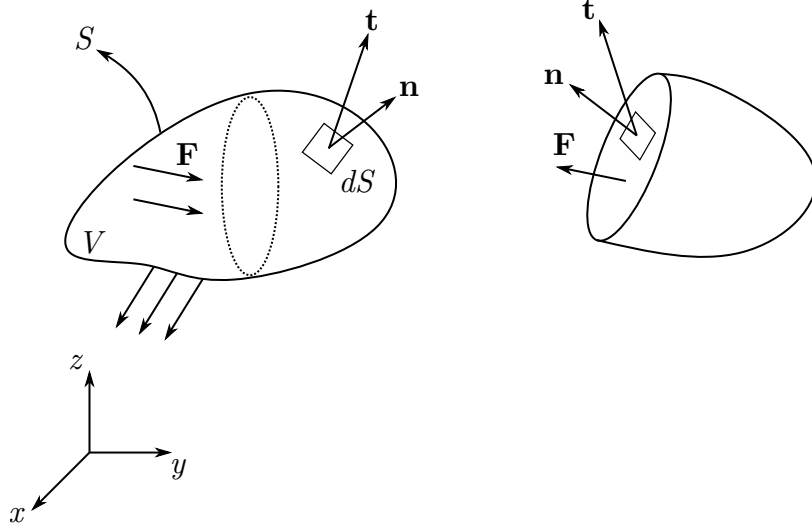
Figure 2.5: Body and surface forces acting on an arbitrary continuum.

Substituting the Eq. 2.31 into Eq. 2.29, an effective E_x^*, E_y^*, G_{xy}^*, ν_{xy}^*, and ν_{yx}^* can be defined as

$$
\begin{aligned}
E_x^* &= \frac{A_{66}A_{12}^2 - 2A_{16}A_{26}A_{12} + A_{16}^2A_{22} + A_{11}\left(A_{26}^2 - A_{22}A_{66}\right)}{h\left(A_{26}^2 - A_{22}A_{66}\right)} \\
E_y^* &= \frac{A_{66}A_{12}^2 - 2A_{16}A_{26}A_{12} + A_{16}^2A_{22} + A_{11}\left(A_{26}^2 - A_{22}A_{66}\right)}{h\left(A_{16}^2 - A_{11}A_{66}\right)} \\
G_{xy}^* &= \frac{A_{66}A_{12}^2 - 2A_{16}A_{26}A_{12} + A_{16}^2A_{22} + A_{11}\left(A_{26}^2 - A_{22}A_{66}\right)}{h\left(A_{12}^2 - A_{11}A_{22}\right)} \\
\nu_{xy}^* &= \frac{A_{16}A_{26} - A_{12}A_{66}}{A_{26}^2 - A_{22}A_{66}} \\
\nu_{yx}^* &= \frac{A_{16}A_{26} - A_{12}A_{66}}{A_{16}^2 - A_{11}A_{66}}
\end{aligned}
\tag{2.32}
$$

where $A_{ij} = A_{ij}(x, y)$ for VAT laminates.

2.2 In-plane analysis

In order to model the in-plane response of VAT composites, firstly is necessary define the equilibrium equations. Dealing with bodies in equilibrium, the applied loading must satisfy the equations of static equilibrium. Thus, the summation of forces and moments is zero (Fig. 2.5). Knowing that the whole body is in equilibrium, then all parts must also be in equilibrium. In Fig. 2.5, $\mathbf{t}$ is the surface traction vector, $\mathbf{n}$ is the unit normal vector, dS is an infinitesimal area, and $\mathbf{F}$ is the body force.

For static equilibrium, the forces acting on the body are balanced and the resultant force must vanish. It follows that
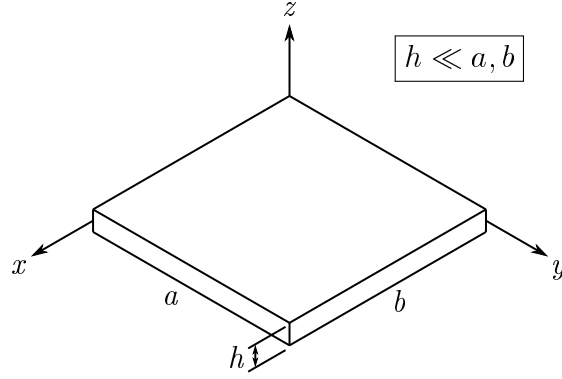
Figure 2.6: Thin plate with thickness much less than its edges length.

$$\iint_S \mathbf{t} \mathrm{d}S + \iiint_V \mathbf{F} \mathrm{d}V = 0 \tag{2.33}$$

The traction vector can be written, in index notation, as

$$t_i = \sigma_{ji} n_j \tag{2.34}$$

Substituting Eq. 2.34 into Eq. 2.33 yields

$$\iint_S \sigma_{ji} n_j \mathrm{d}S + \iiint_V F_i \mathrm{d}V = 0 \tag{2.35}$$

Applying the divergence theorem in Eq. 2.35, it reduces to

$$\iiint_V \left(\frac{\partial \sigma_{ji}}{\partial x_j} + F_i \right) \mathrm{d}V = 0 \tag{2.36}$$

As the region V is arbitrary and the integrand in Eq. 2.36 is continuous, it must vanishes, yielding

$$\frac{\partial \sigma_{ji}}{\partial x_j} + F_i = 0 \tag{2.37}$$

For thin plates as well as thin laminae, one can consider a plane stress (Fig. 2.6). Thus, the Eq. 2.37 can be written in 2D scalar setting $\sigma_z = 0$, $\sigma_{yz} = 0$ and $\sigma_{zy} = 0$ (JONES, 1998),

$$\begin{aligned} \frac{\partial \sigma_x}{\partial x} + \frac{\partial \tau_{xy}}{\partial y} + F_x = 0 \\ \frac{\partial \sigma_y}{\partial y} + \frac{\partial \tau_{xy}}{\partial x} + F_y = 0 \end{aligned} \tag{2.38}$$

Integrating the Eq. (2.38) with respect to z, using the relation in Eq. 2.20, neglecting the body forces, and according to Leibniz integral rule, it can be written as follows

$$\frac{\partial N_x}{\partial x} + \frac{\partial N_{xy}}{\partial y} = 0$$

$$\frac{\partial N_y}{\partial y} + \frac{\partial N_{xy}}{\partial x} = 0$$

(2.39)

The in-plane constitutive relation for a symmetric angle-ply laminate is given by Eq. 2.27. Substituting this relation into Eq. 2.39, yields

$$A_{11}(x,y)\frac{\partial^2 u}{\partial x^2} + A_{66}(x,y)\frac{\partial^2 u}{\partial y^2} + [A_{12}(x,y) + A_{66}(x,y)]\frac{\partial^2 v}{\partial x \partial y} + \frac{\partial A_{11}(x,y)}{\partial x}\frac{\partial u}{\partial x}$$

$$+ \frac{\partial A_{12}(x,y)}{\partial x}\frac{\partial v}{\partial y} = 0$$

$$A_{66}(x,y)\frac{\partial^2 v}{\partial x^2} + A_{22}(x,y)\frac{\partial^2 v}{\partial y^2} + [A_{12}(x,y) + A_{66}(x,y)]\frac{\partial^2 u}{\partial x \partial y}$$

$$+ \frac{\partial A_{66}(x,y)}{\partial x}\left(\frac{\partial u}{\partial y} + \frac{\partial v}{\partial x}\right) = 0$$

(2.40)

These are elliptic partial differential equations (PDEs), coupled in terms of the axial displacement u and transverse displacement v. Furthermore, these equations have variable coefficients since the elements of $A_{ij}(x,y)$ are functions of both the x and y. The solution of these equations is made simultaneously yielding the u and v displacement field, from which the strains and stress resultants can be calculated. Further details of the derivation above can be seen in Whitney (1987) and Sadd (2009).

2.3   Buckling analysis

In order to solve the buckling problem, it is possible to apply the Ritz method. This method is an energy-based method and it is applied to find the lowest load that will cause buckling (JONES, 1998; KOLLAR; SPRINGER, 2003; KUMAR, 2018). In this work, it was considered a rectangular plate simply supported along its four edges (2.7). The plate deflection expression that satisfies the geometrical boundaries is as follows

$$w(x,y) = \sum_{i=1}^{I}\sum_{j=1}^{J} c_{ij} \sin\left(\frac{i\pi x}{a}\right)\sin\left(\frac{j\pi y}{b}\right)$$

(2.41)

where c_{ij} are arbitrary coefficients and I and J are integers indicating the highest number of terms in the x and y direction.

In this method, the energy functional F is defined as the potential energy of the panel. To obtain c_{ij}, the energy functional F is minimized by by taking partial derivatives with respect to c_{ij}

$$\frac{\partial F}{\partial c_{ij}} = \frac{\partial(U+V)}{\partial c_{ij}} = 0$$

(2.42)

where U is the strain energy due to bending, and V the potential energy of the in-plane loads. The strain energy of an elastic body is given by (JONES, 1998):

$$U = \frac{1}{2} \iiint \left(\sigma_x \epsilon_x + \sigma_y \epsilon_y + \sigma_z \epsilon_z + \sigma_{xy} \epsilon_{xy} + \sigma_{xz} \epsilon_{xz} + \sigma_{yz} \epsilon_{yz} \right) \mathrm{d}V \qquad (2.43)$$

However, according to CLT theory, $\epsilon_z = \epsilon_{xz} = \epsilon_{yz} = 0$. Substituting the Eq. 2.18 into Eq. 2.42 yields

$$U = \frac{1}{2} \int_0^a \int_0^b \left[D_{11} \left(\frac{\partial^2 w}{\partial x^2} \right)^2 + 2 D_{12} \frac{\partial^2 w}{\partial x^2} \frac{\partial^2 w}{\partial y^2} + D_{22} \left(\frac{\partial^2 w}{\partial y^2} \right)^2 \right.$$
$$\left. + 4 \left(D_{16} \frac{\partial^2 w}{\partial x^2} + D_{26} \frac{\partial^2 w}{\partial y^2} \right) \frac{\partial^2 w}{\partial x \partial y} + 4 D_{66} \left(\frac{\partial^2 w}{\partial x \partial y} \right)^2 \right] \mathrm{d}x\mathrm{d}y \qquad (2.44)$$

The potential energy is related to the applied load in the pre-buckled state and the mid-plane strains that is the effect from the out-plane deflections of the panel. The V expression is given by (JONES, 1998):

$$V = \frac{1}{2} \lambda \int_0^a \int_0^b \left[N_x \left(\frac{\partial w}{\partial x} \right)^2 + N_y \left(\frac{\partial w}{\partial y} \right)^2 + 2 N_{xy} \frac{\partial w}{\partial x} \frac{\partial w}{\partial y} \right] \mathrm{d}x\mathrm{d}y \qquad (2.45)$$

where λ is an arbitrary multiplier. Equation 2.41 is then substituted into Eqs. 2.44 and 2.45. The differentiations are performed and Eq. 2.42 reduces to

$$\sum_{i=1}^{I} \sum_{j=1}^{J} \left\{ \pi^4 \int_0^a \int_0^b \left[\frac{i^2 k^2}{a^4} D_{11} + \left(\frac{i^2 l^2 + j^2 k^2}{a^2 b^2} \right) D_{12} \right. \right.$$
$$\left. + \frac{j^2 l^2}{b^4} D_{22} \right] \sin i\bar{x} \sin j\bar{y} \sin k\bar{x} \sin l\bar{y} \; \mathrm{d}x\mathrm{d}y$$
$$+ \frac{4\pi^4 ijkl}{a^2 b^2} \int_0^a \int_0^b D_{66} \cos i\bar{x} \cos j\bar{y} \cos k\bar{x} \cos l\bar{y} \; \mathrm{d}x\mathrm{d}y$$
$$- 2\pi^4 \left[\int_0^a \int_0^b \left(\frac{ik^2 j}{a^3 b} D_{16} + \frac{ijl^2}{ab^3} D_{26} \right) \cos i\bar{x} \cos j\bar{y} \sin k\bar{x} \sin l\bar{y} \; \mathrm{d}x\mathrm{d}y \right.$$
$$\left. + \int_0^a \int_0^b \left(\frac{i^2 kl}{a^3 b} D_{16} + \frac{j^2 kl}{ab^3} D_{26} \right) \sin i\bar{x} \sin j\bar{y} \cos k\bar{x} \cos l\bar{y} \; \mathrm{d}x\mathrm{d}y \right] \qquad (2.46)$$
$$+ \frac{\lambda \pi^2 ik}{a^2} \int_0^a \int_0^b N_x \cos i\bar{x} \cos j\bar{y} \cos k\bar{x} \cos l\bar{y} \; \mathrm{d}x\mathrm{d}y$$
$$+ \frac{\lambda \pi^2 jl}{b^2} \int_0^a \int_0^b N_y \sin i\bar{x} \cos j\bar{y} \sin k\bar{x} \cos l\bar{y} \; \mathrm{d}x\mathrm{d}y$$
$$+ \frac{\lambda \pi^2}{ab} \left[jk \int_0^a \int_0^b N_{xy} \sin i\bar{x} \cos j\bar{y} \sin k\bar{x} \cos l\bar{y} \; \mathrm{d}x\mathrm{d}y \right.$$
$$\left. \left. + il \int_0^a \int_0^b N_{xy} \cos i\bar{x} \sin j\bar{y} \cos l\bar{y} \sin k\bar{x} \; \mathrm{d}x\mathrm{d}y \right] \right\} c_{ij} = 0$$
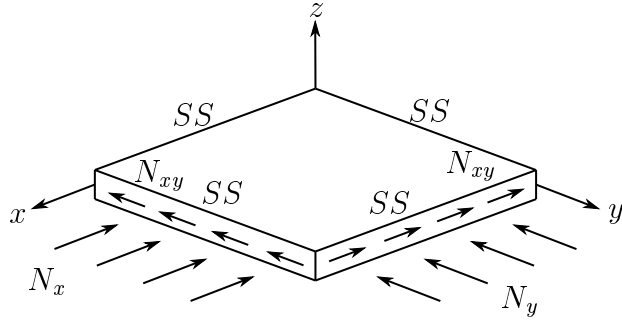
Figure 2.7: Rectangular simply supported (SS) plate subjected to compressible loads.

where $\bar{x} = \pi x/a$, $\bar{y} = \pi y/b$, the indices k and l take the values $k = 1, 2, \ldots, I$ and $l = 1, 2, \ldots, J$. D_{ij} and the stress resultants N_x, N_y, and N_{xy} are also function of x and y for VAT composites. Equation 2.46 can be rewritten as an eigenvalue problem:

$$(\mathbf{K} - \lambda \mathbf{M})c_{ij} = 0 \tag{2.47}$$

where $\mathbf{K}$ is the stiffness matrix that contains the sum of integrals of D_{ij} and $\mathbf{M}$ is the geometric matrix, containing the sum of the stress resultant integrals. The lowest value of λ, λ_{cr}, from Eq. 2.47, determines the critical buckling load or displacement, as it was analyzed in this work.

Chapter 3

Methodology

In this work, it was analyzed panels subject to an end shortening displacement with two different boundary conditions in the edges. A uniform end shortening is a common boundary condition under testing conditions. In this sort of testing, a uniform end displacement is applied while the equivalent load is measured. A schematic representation can be seen in Fig. 3.1. The Case I consists of an applied end shortening, u_0, at $x = \pm a/2$. The transverse edges have no applied forces and they are not free to deform, $v(x, y) = 0$. In the Case II, in the same manner as in Case I, it is applied an end shortening, but the another edges are free to deform. In both cases, it is not considered a shear stress applied in any edge.

To model the fiber angle variation, it was considered a linear and a cubic angle variation. Regarding the angle ϕ, it was considered in this work two different values: $0°$ and $90°$. Thus, Eqs. 1.1 and 1.3 only vary along one direction, x or y, depending on the angle. When $\phi = 0°$, the angle varies on x-axis, $\theta(x)$. When $\phi = 90°$, the angle varies on y-axis, $\theta(y)$.

To calculate the in-plane response of the VAT panels, it was applied the Finite Element Method (FEM). The FEM is a technique to solve PDEs numerically. To solve PDEs with the FEM, basically it is needed a discrete representation of a region, known as a mesh, PDEs that model the physical behavior of the phenomena and boundary conditions that coupling the PDEs with the region. The mesh is a discrete region that is partitioned into a bunch of small elements that summing up them, it compose the entire discrete region. Finding the numerical solution is based on computing the solution on the smaller elements and then combining the partial solutions into a solution over the entire mesh (HUGHES, 2000). An example of a mesh is shown in Fig. 3.2.

In this work, it was used the software Mathematica to solve the PDEs (Eq. 2.40). Mathematica is a modern technical computing system, with capabilities to perform symbolic and numeric computations, a general software for use in scientific and engineering problems. It has an integration of the symbolic, graphical, and numerical components into one system accessible through a common language (WOLFRAM et al., 1999). It has a build-in
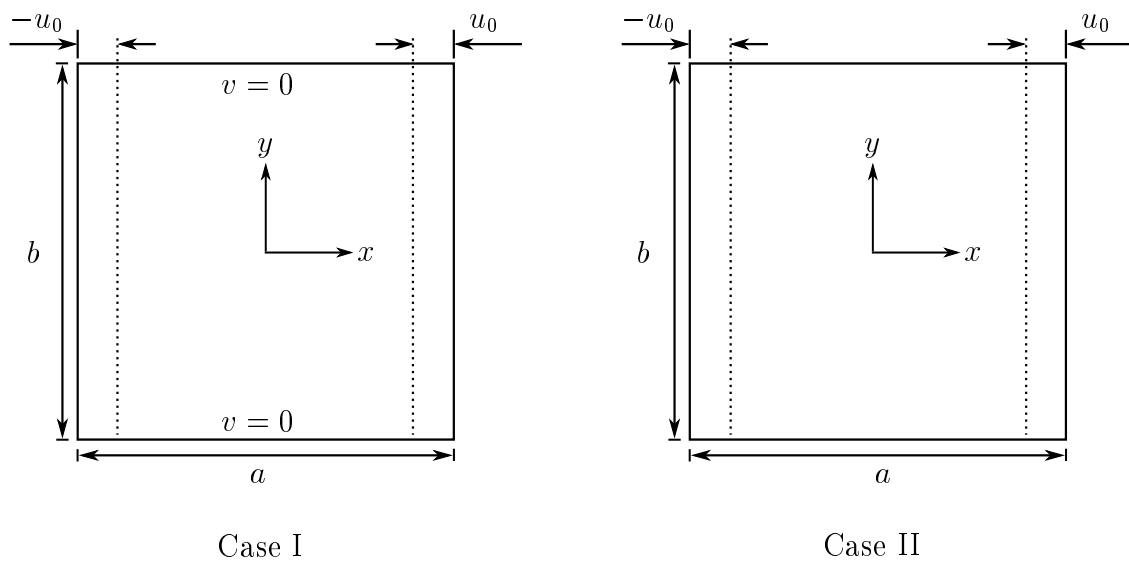
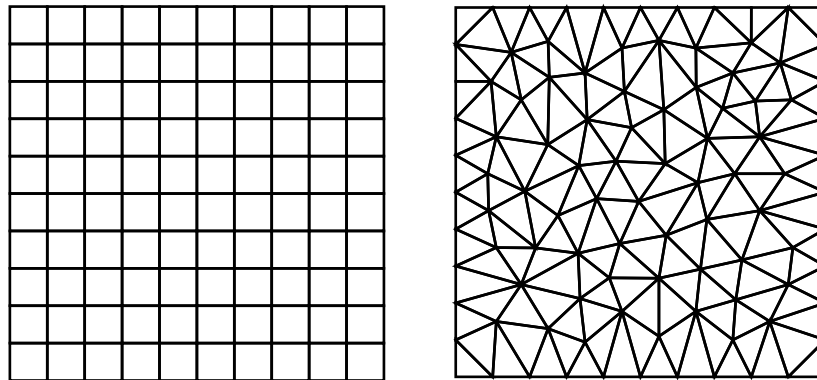Figure 3.1: Panel boundary conditions for Case I and Case II.

Figure 3.2: Two different examples of meshes presenting rectangular (left) and triangular elements (right).

function called `NDSolve`, a powerful solver of differential equations (MIKHAILOV, 2008). As one of its algorithms, `NDSolve` has an algorithm based on finite element method. As options, it is possible to choose the element type (`MeshElementType`) and the elements size (`MaxElementMeasure`). It was chose a 8-node second-order rectangular elements (OÑATE, 2013), as shown in Fig. 3.3.

As the FEM is a numerical method, it is necessary to guarantee the convergence of the solution. This convergence must satisfies both displacement field, $u(x, y)$ and $v(x, y)$. One of the most regarding solution convergence is the mesh. It is crucial determining how many elements will be necessary to provide an accurate result. The number of elements is related to the mesh size. If the mesh has few elements, it is possible that important details will be neglected, resulting in poor results.

For the sake of accurate results, it was performed a mesh convergence for both linear and cubic angle variations with the intention of define the desirable number of elements, as shown in Figs. 3.4 and 3.5. It can be seen that in the case where the fiber varies linearly,
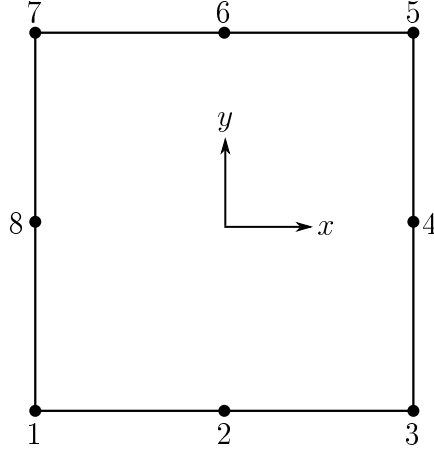
Figure 3.3: 8-node second-order rectangular element.

it is needed less elements than a cubic variation. This behavior is expected knowing that a cubic variation is more complex and presents larger displacements gradients. Case II is not shown here since it presents convergence using few elements.

Regarding the aspect ratio (a/b), it does not show relevant differences between $a/b = 0.5$, 1, and 2. For the linear variation, it was used 200 elements, and for cubic variation 400 elements. It was evaluated the laminate $[0° \pm \langle 0°|90°\rangle]_{3S}$ for a linear variation because it presents the biggest displacement gradient and this way the convergence study is valid for angles between $0°$ and $90°$. The same idea can be extended to the laminate $[0° \pm \langle 0°|90°|0°|90°\rangle]_{3S}$ in the cubic variation case.

With u and v displacement fields solved, it is possible to calculate the in-plane stress resultants using the Eq. 2.27. Thus,

$$
\begin{aligned}
N_x &= A_{11}\frac{\partial u}{\partial x} + A_{12}\frac{\partial v}{\partial y} \\
N_y &= A_{12}\frac{\partial u}{\partial x} + A_{22}\frac{\partial v}{\partial y} \\
N_{xy} &= A_{66}\left(\frac{\partial u}{\partial y} + \frac{\partial v}{\partial x}\right)
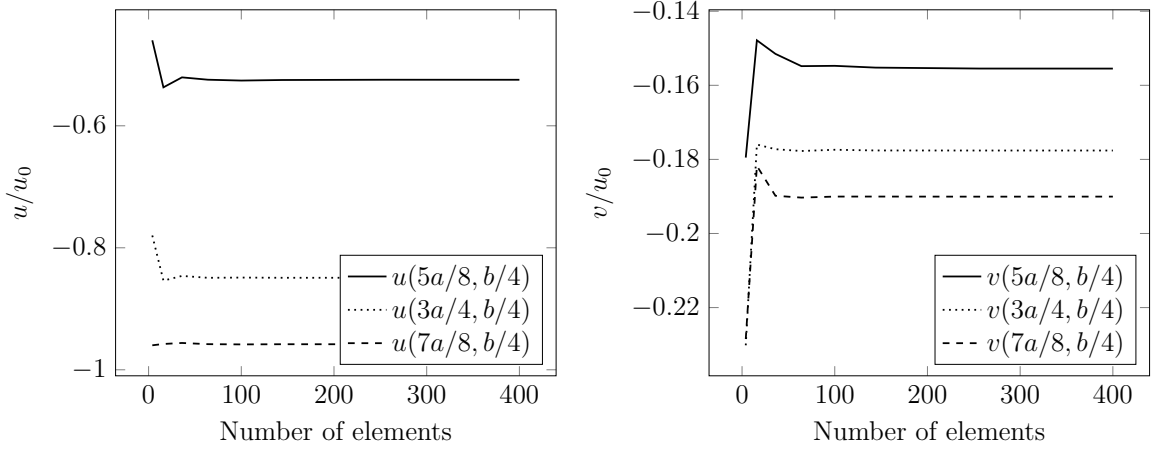\end{aligned}
\tag{3.1}
$$

Figure 3.4: Case I (a/b = 1) with cubic variation of the laminate $[0° \pm \langle 0°|90°\rangle]_{3S}$.

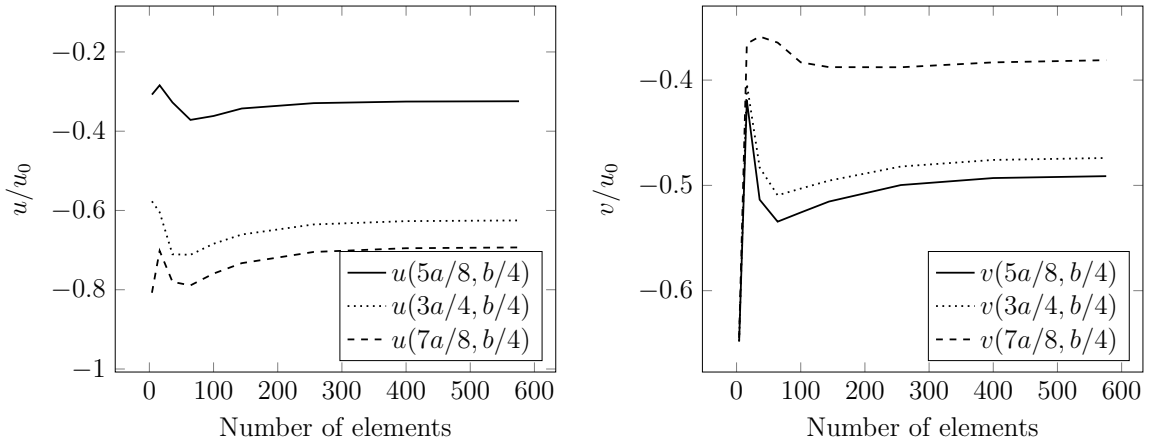Figure 3.5: Case I (a/b = 1) with cubic variation of the laminate $[0° \pm \langle 0°|90°|0°|90°\rangle]_{3S}$.

As mentioned before, depending on turning radius of the fiber path, manufacture defects can happen. This way, it was only evaluated angle variations that present turning radius less than 635 mm to avoid laminates impossible to be manufactured properly (TATTING; GURDAL, 2002). For both linear and cubic variation, the curvature can be written as:

$$k\left(x'\right) = \frac{d\theta\left(x'\right)}{dx'} \cos\left(\theta\left(x'\right)\right) \tag{3.2}$$

The curvature function was plotted in modulus for linear and cubic angle variations for different laminae, as can be shown in Figs. 3.6 and 3.7. These results are valid for any ϕ as the curvature is calculated through the first derivative and ϕ is a constant.

As can be seen in Fig. 3.6, the layer $\langle -45°|45°\rangle$ has curvature higher than k_{crit} along the whole panel. Thus, it could presents manufacture defects and it must be avoided in the design phase. In a similar way, the layers for a cubic angle variation, $\langle 0°|25°|30°|45°\rangle$ and $\langle 45°|15°|30°|90°\rangle$, shown in Fig. 3.7, also has curvature higher than k_{crit} at some regions and must be avoided. One can note that a cubic angle variations is more prone to high

curvatures. All the following results are based on laminates that have curvature lesser than k_{crit}.
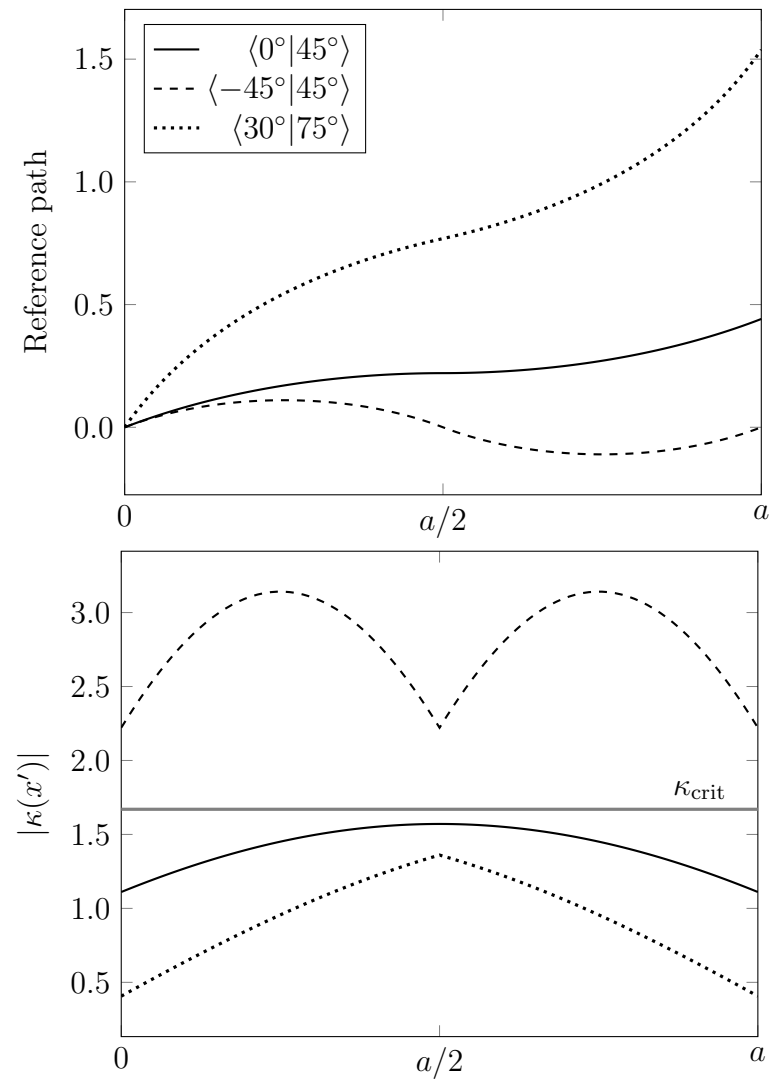

Figure 3.6: Examples of fiber curvature and reference path for $(a/b = 1)$ and linear angle variation for different laminae.
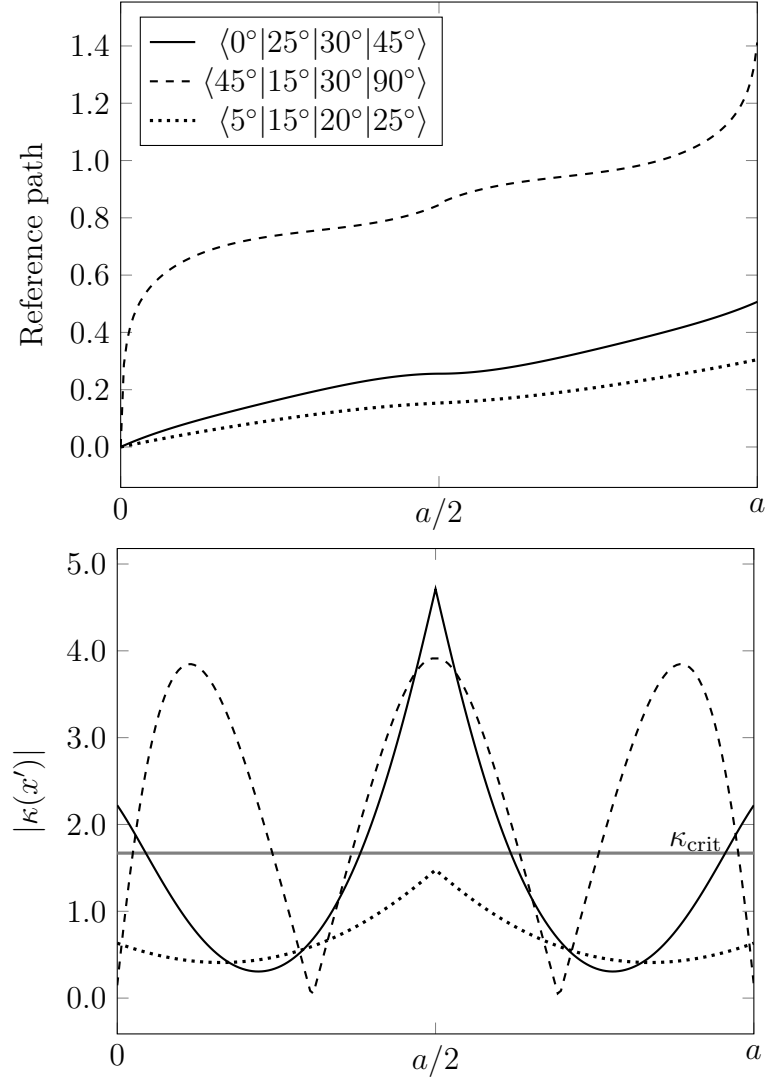
Figure 3.7: Examples of fiber curvature and reference path ($a/b = 1$) and cubic angle variation for different laminae.

Regarding the buckling analysis, in order to get reliable results, it is essential to determine the number of terms necessary in the $w(x, y)$ function. As it was analyzed the buckling load for different aspect ratios (0.5, 1, 2 and 3), it was required to perform a convergence study for all aspect ratios. The convergence of the eigenvalues for case I for linear and cubic angle variation is shown in Tabs. 3.1 and 3.2, respectively. As the boundary conditions of the case I involve N_x and N_y in the calculations, it shows most difficulty to converge. Thus, it was only evaluated the convergence for case I. Regarding the angle ϕ, the angles $0°$ and $90°$ exhibited similar results, so only the results for $\phi = 0°$ are shown. The same happened to others layups. In light of the results, it was adopted $I = J = 10$.

Table 3.1: Ritz method converge for linear angle variation.

Case I – $[0° \pm \langle 45°|75° \rangle]_{3S}$						
$a/b = 0.5$	$a/b = 1$	$a/b = 2$	$a/b = 3$			
u_{cr}	u_{cr}	u_{cr}	u_{cr}	I	J	$I \times J$
0.00547088	0.00600322	0.00851569	0.0115659	3	3	9
0.00544822	0.00595684	0.00847652	0.0115544	5	5	25
0.0054434	0.00594918	0.00846769	0.0115511	7	7	49
0.00544329	0.00594825	0.00846567	0.0115501	10	10	100
0.00544305	0.00594791	0.00846501	0.0115496	12	12	144
0.00544302	0.0059478	0.00846472	0.0115493	15	15	225

Table 3.2: Ritz method converge for cubic angle variation.

Case I – $[0° \pm \langle 45°|60°|75°|75° \rangle]_{3S}$						
$a/b = 0.5$	$a/b = 1$	$a/b = 2$	$a/b = 3$			
u_{cr}	u_{cr}	u_{cr}	u_{cr}	I	J	$I \times J$
0.00527521	0.00649227	0.0112305	0.0162436	3	3	9
0.00526544	0.00646149	0.0112295	0.0160661	5	5	25
0.00526105	0.00645667	0.0112132	0.0160133	7	7	49
0.00526036	0.00645509	0.0112109	0.0160122	10	10	100
0.00526036	0.00645501	0.0112108	0.0160120	12	12	144
0.00526033	0.00645494	0.0112108	0.0160120	15	15	225

Having in mind that the panels were loaded through a constant displacement at its edges, it is important to define the force necessary to create the uniform displacement. Thus, the total force induced on the panel can be defined as:

$$F_x = \int_0^b N_x(a, y) \mathrm{d}y. \tag{3.3}$$

To obtain an average N_x value, F_x is divided by the length of the panel edge, as follows:

$$N_x^{\mathrm{av}} = \left(\frac{1}{b} \right) F_x. \tag{3.4}$$

In order to facilitate the comparison between the results, $N_{\mathrm{cr}}^{\mathrm{av}}$ was normalized as

$$\bar{N}_x^{\mathrm{av}} = \frac{N_x^{\mathrm{av}} a^2}{E_1 h^3} \tag{3.5}$$

finally the critical normalized average load N_x is obtained by

$$N_{\mathrm{cr}} = \lambda_{\mathrm{cr}} \bar{N}_x^{\mathrm{av}} \tag{3.6}$$

where λ_{cr} is the lowest eigenvalue of the Eq. 2.47. To have a parameter related to stiffness, an equivalent panel stiffness was defined to consider an overall panel stiffness

$$E_x^{\text{eq}} = \frac{F_x a}{hbu_0} \tag{3.7}$$

where h is the panel thickness. Substituting Eq. 3.3 into Eq. 3.7 yields

$$E_x^{\text{eq}} = \left(\frac{a}{hbu_0}\right) \int_0^b N_x(a, y)\mathrm{d}y. \tag{3.8}$$

Chapter 4

Results

4.1 In-plane results and discussion

The results here are based on a twelve layer laminate, $[\pm\theta]_{3S}$. The properties of the material are shown in Tab. 4.1

Table 4.1: T300/N5208 Carbon/Epoxy lamina properties (GÜRDAL; TATTING; WU, 2008).

Material Properties	T300/N5208
Longitudinal modulus (E_1)	181 GPa
Transverse modulus (E_2)	10.3 GPa
In-plane shear modulus (G_{12})	7.17 GPa
Major Poisson's ratio (ν_{12})	0.28
Thickness (t)	0.127 mm

4.1.1 Case I

As follows, firstly it was analyzed the displacements fields and stress resultants for case I. According to its boundary conditions, the panel when compressed in the direction of the load will not extend in the transverse direction. As a consequence, the $v(x, y)$ displacement is zero for all directions, $u(x, y)$ is a function of x only, and the shear strain is zero for all x and y. In the Figs. 4.1 and 4.2. is shown the normalized u displacement at $y = b/2$ for linear and cubic angle variation, respectively.

As expected, the curves are non-linear for linear and cubic variation due to the variable stiffness. For linear variation, Fig. 4.1, all laminates presents the difference between the angle T_1 and T_0 equals to 45°. This difference was fixed to clarify the influence of T_1 and T_0 on the in-plane response. A first distinction between the laminates is the shape of the curves, they being convex or concave to some degree. One could take as example the laminates $[0° \pm \langle 45°|0°\rangle]_{3S}$ and $[0° \pm \langle 45°|90°\rangle]_{3S}$. The main difference between them is which angle is greater than the other. When T_0 is greater than T_1, the curve is concave,
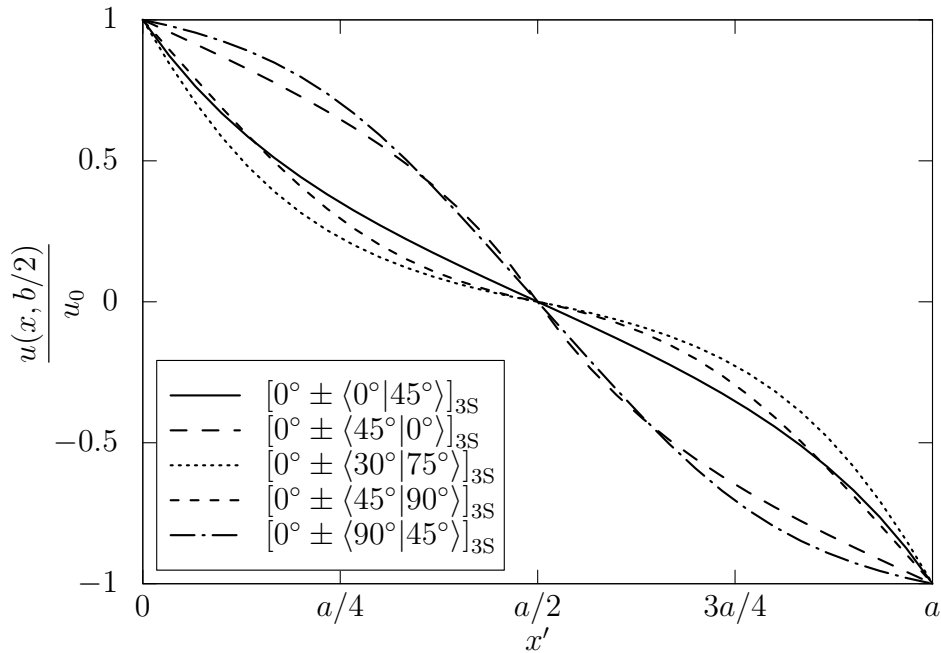
Figure 4.1: u displacement for case I with linear angle variation, aspect ratio $(a/b) = 1$ and $\phi = 0°$.

and it is convex when T_1 is greater than T_0, assuming the interval $0 \leqslant x \leqslant a/2$.

For the panel with $T_1 = 90°$, it is more compliant at its edges, and consequently exhibits large strain gradients in the region, unlike panel with $T_1 = 0°$ that exhibits less compliant at center and so high axial strain. This can be inspected by analyzing the slope (derivative) of the curves.

For panels with cubic angle variation, there is a slight different behavior, as shown in Fig. 4.2. There are four distinct regions in which the panel can exhibits less or more compliant, and so axial strain. For this reason, it can present a convex and concave shape in the interval $0 \leqslant x \leqslant a/2$. An example is the laminate $[0° \pm \langle 90°|75°|60°|90°\rangle]_{3S}$ that has the same compliant at its edge and center, however it has different compliant between them. This results in a convex region between $x = 0$ and $x = a/6$ and a concave one between $x = a/6$ and $x = a/2$. As mentioned above, u is just a function of x due to the boundary conditions, as shown in Fig. 4.3. It is possible to observe that u for the cubic variation case there are more than one convex and concave region.

In order to compare the results from linear and cubic variation, N_x and N_y were normalized as

$$\bar{N}_i = N_i \frac{a}{u_0 A_{11}^{0°}}, \quad i = x, y, xy. \tag{4.1}$$

where $A_{11}^{0°}$ is the first element of the stiffness matrix $\mathbf{A}$ for a laminate $[0°]_{6S}$. Regarding to the stress resultant N_x, it is constant in all panel domain, as can be seen in Fig. 4.4. The both laminates have the same angle at $x = 0$ and $x = a/2$, and so they present, basically, the same $\bar{N}_x$ constant result. There is minor influence of the angles T_1 and T_2
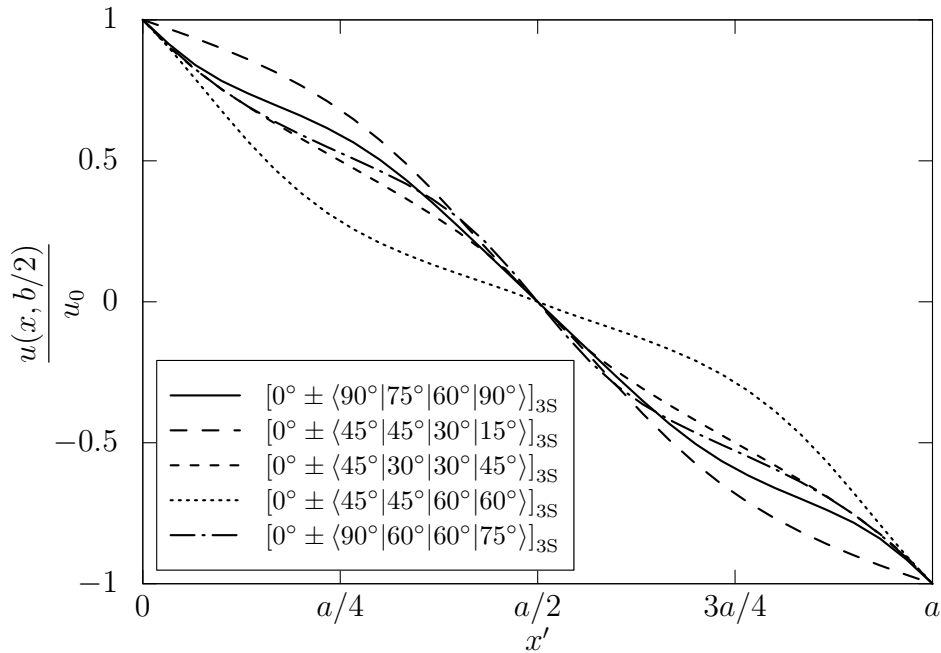
Figure 4.2: u displacement for case I with cubic angle variation, aspect ratio $(a/b) = 1$ and $\phi = 0°$.

on the results for the cubic linear case.

The transverse stress resultant, $\bar{N}_y$, unlike $\bar{N}_x$, it is not constant, it varies in the x direction (Figs. 4.5 and 4.6). In both cases, linear and cubic variation, the normalized value of $\bar{N}_y$ is negative. As u_0 is a positive value, that indicates that $\bar{N}_y$ is compressive load. Comparing the results for linear and cubic angle variation, it is possible to notice that for cubic variation is notably more complex. One feature of cubic angle variation is the possibility to have the same angle at panel edges and center, as example the laminate $[0° \pm \langle 90°|75°|60°|90°\rangle]_{3S}$. It is also possible to have a symmetric or non-symmetric stress variation in the interval $0 \leqslant x \leqslant a/2$, or $a/2 \leqslant x \leqslant a$, equivalently, as can be seen in Fig. 4.6 for the laminates $[0° \pm \langle 45°|30°|30°|45°\rangle]_{3S}$ and $[0° \pm \langle 90°|75°|60°|90°\rangle]_{3S}$, respectively.

In Fig. 4.8 is compared the stress resultant $\bar{N}_y$ for a linear and cubic angle variation. The both laminates present the same angles at the edges and center of the panel, this way they show the same stress resultant at these points. One can notice that when a cubic angle variation is used, it is possible to have more flexibility to tailor the loads. Figure 4.8 shows the stress resultant $\bar{N}_y$ for two different laminates in all panel domain. It can be seen that, indeed, $\bar{N}_y$ varies only in x direction.

Due to the case I boundary conditions, $\bar{N}_y$ is dictated by the minor Poisson's ratio ν_{yx}. It can be seen comparing the Fig. 4.8 and the Figs. 4.9 and 4.10. The stress resultant $\bar{N}_y$ has the same shape presented by the corresponding $\nu_{yx}(x)$. As $\bar{N}_y$ is a compressive load, its shape is flipped in relation to $\nu_{yx}(x)$ shape. In this manner, to tailor $\bar{N}_y$ variation over the plate, one must take into account the $\nu_{yx}(x)$ function.
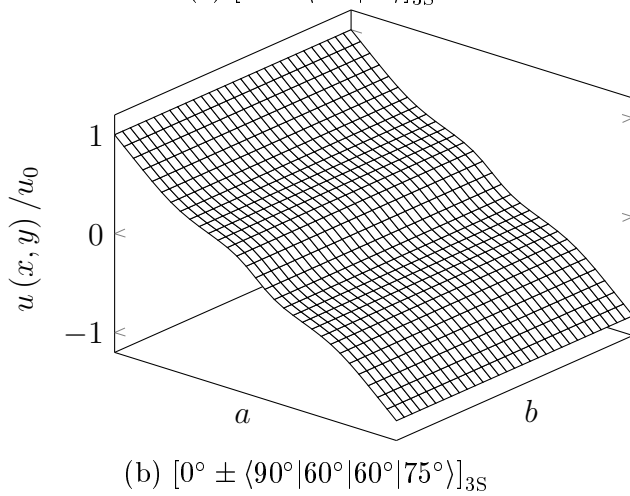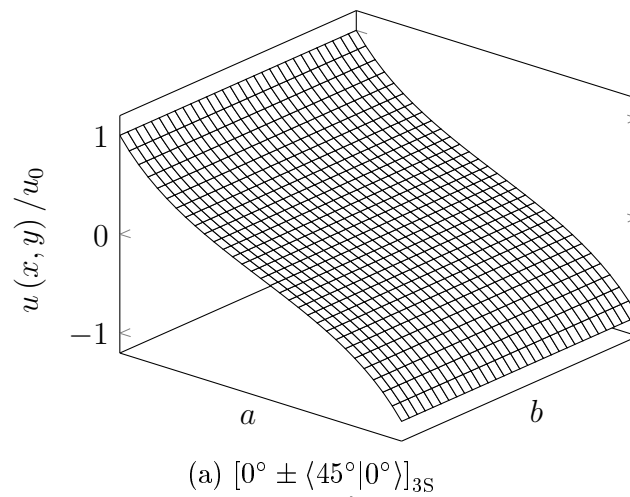
(a) $[0° \pm \langle 45°|0°\rangle]_{3S}$

(b) $[0° \pm \langle 90°|60°|60°|75°\rangle]_{3S}$

Figure 4.3: u displacement for case I with linear (a) and cubic angle variation (b), aspect ratio $(a/b) = 1$ and $\phi = 0°$.
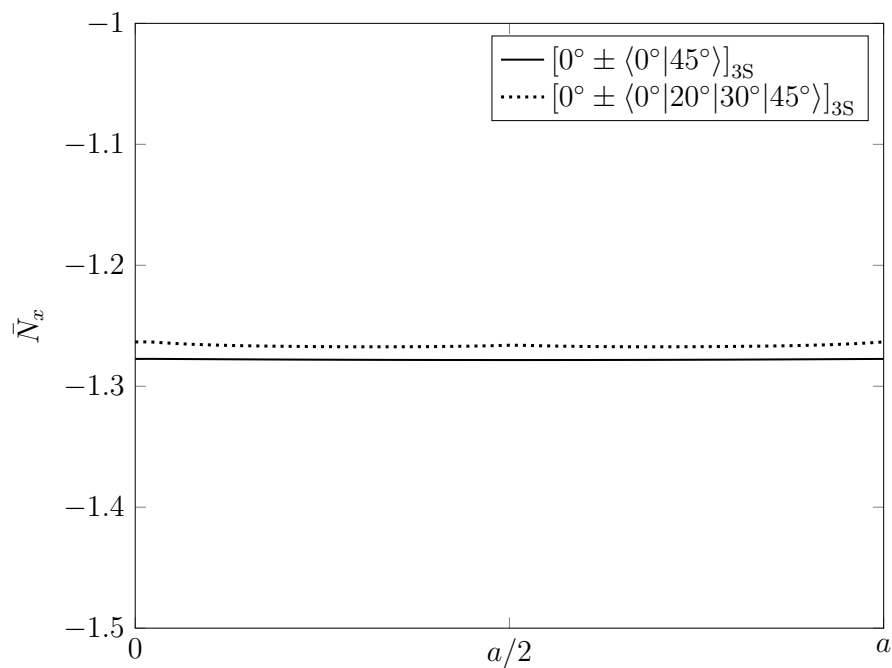

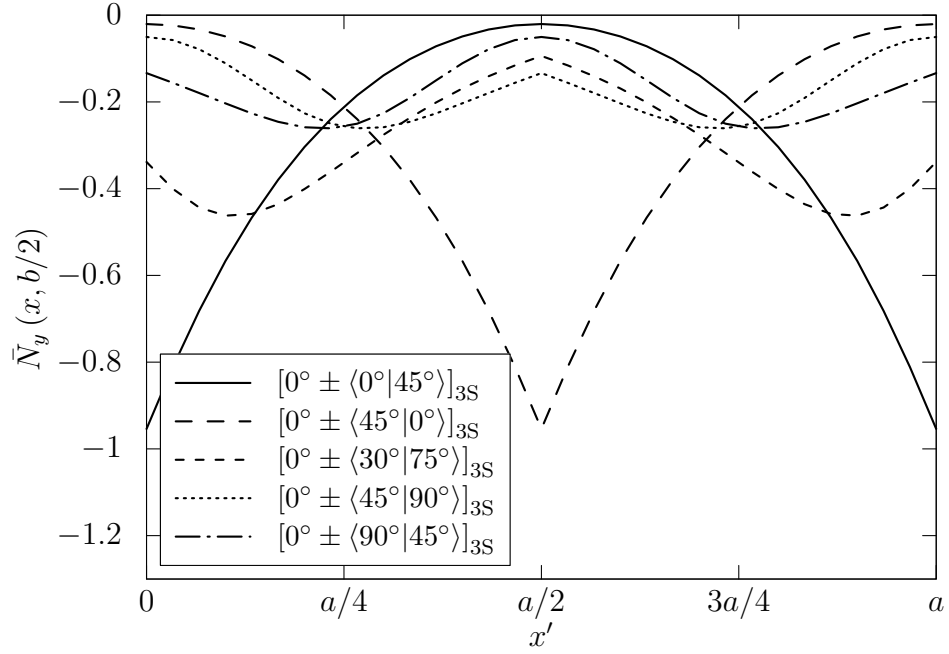Figure 4.4: Normalized stress resultant $\bar{N}_x$ at $y = b/2$.

Figure 4.5: $\bar{N}_y$ stress resultant for case I with linear angle variation, aspect ratio $(a/b) = 1$ and $\phi = 0°$.
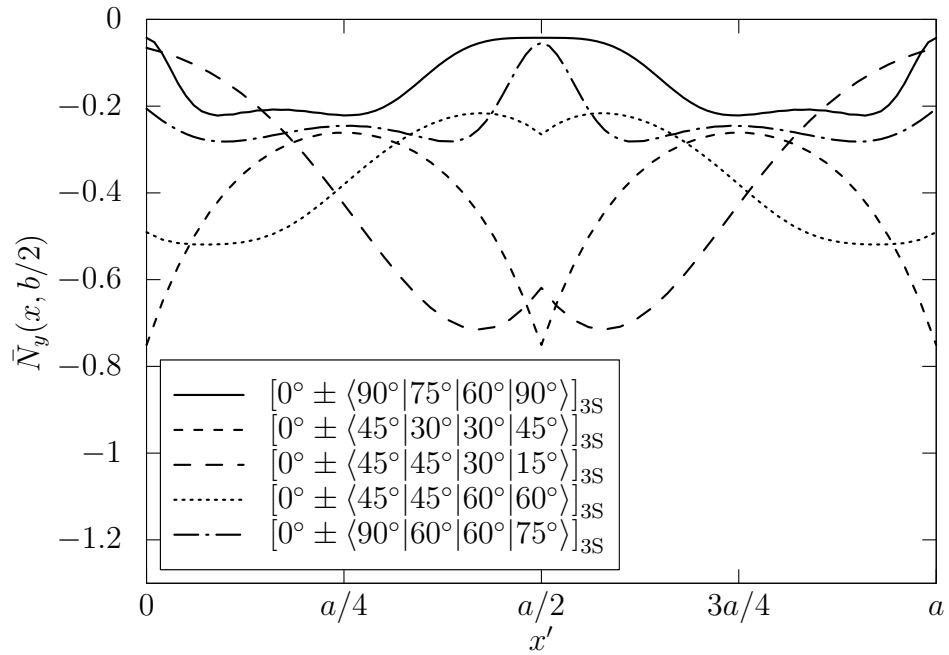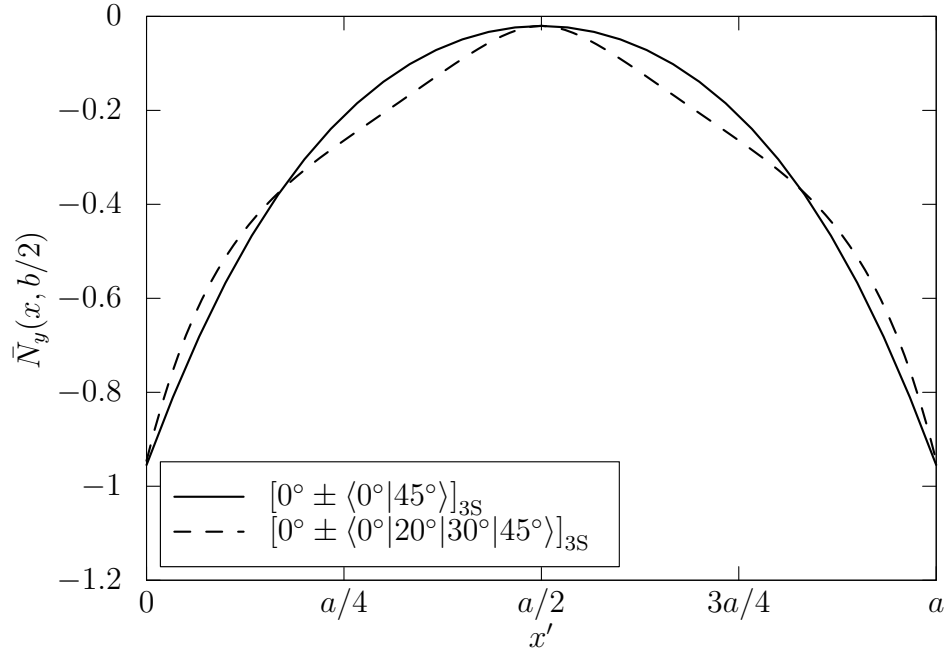

Figure 4.6: $\bar{N}_y$ stress resultant for case I with cubic angle variation, aspect ratio $(a/b) = 1$ and $\phi = 0°$.
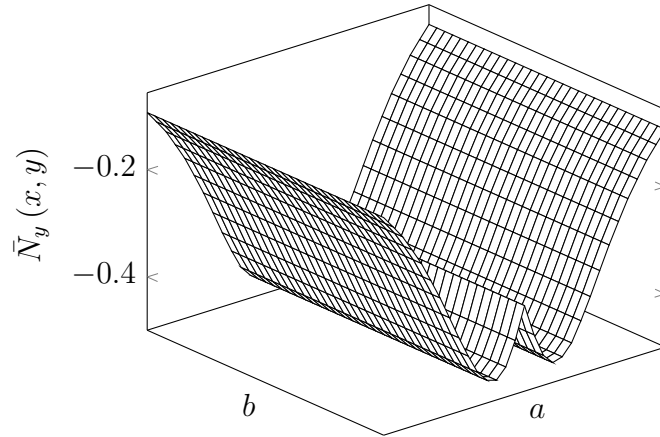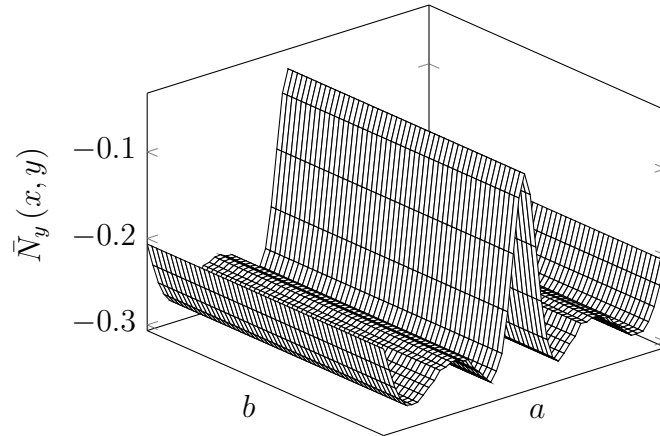
Figure 4.7: $\bar{N}_y$ stress resultant comparison between linear and cubic angle variation.

(a) $[0° \pm \langle 75°|30°\rangle]_{3S}$

(b) $[0° \pm \langle 90°|60°|60°|75°\rangle]_{3S}$

Figure 4.8: $\bar{N}_y$ stress resultant for case I with linear (b) and cubic angle variation (b), aspect ratio $(a/b) = 1$ and $\phi = 0°$.
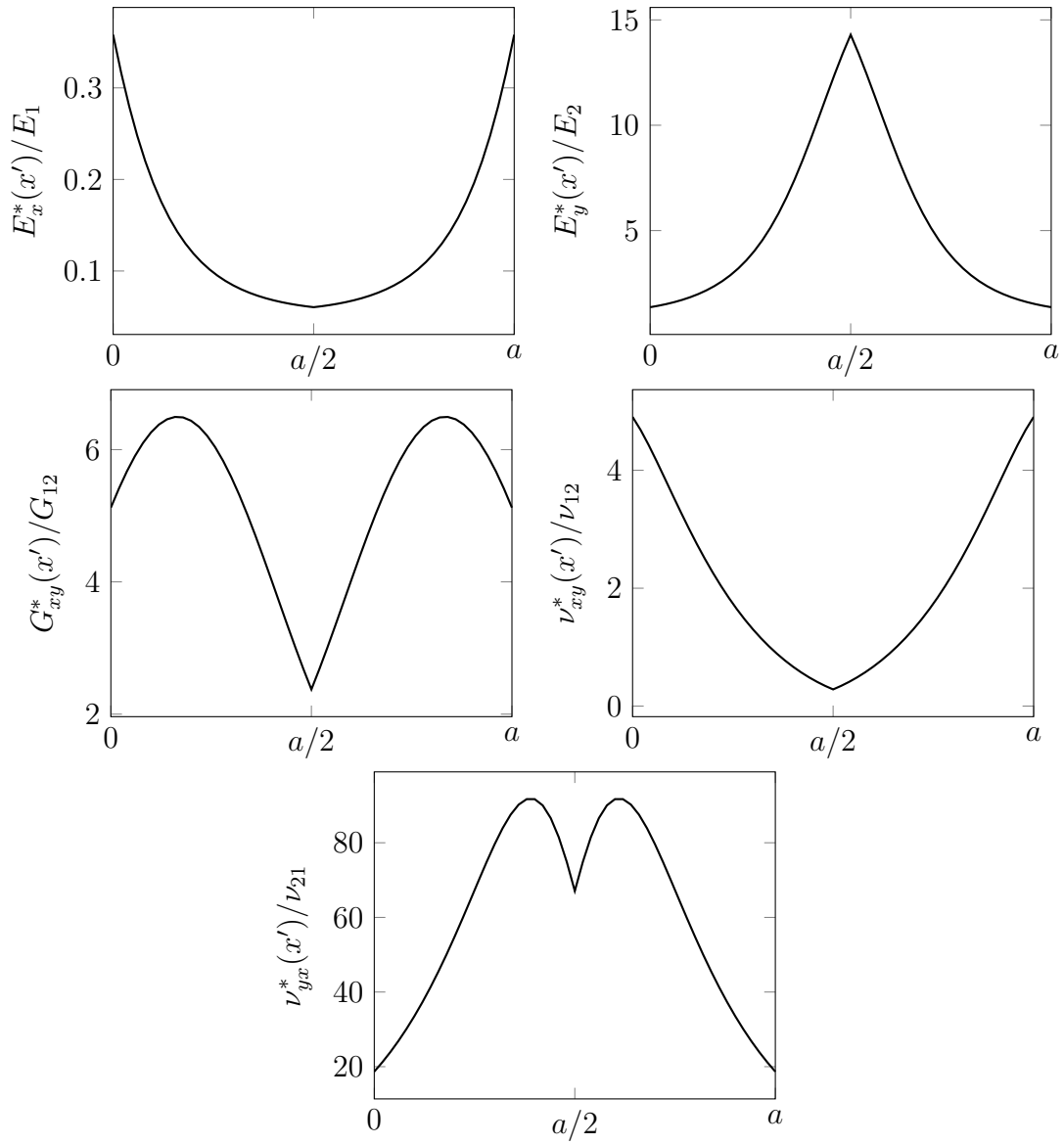
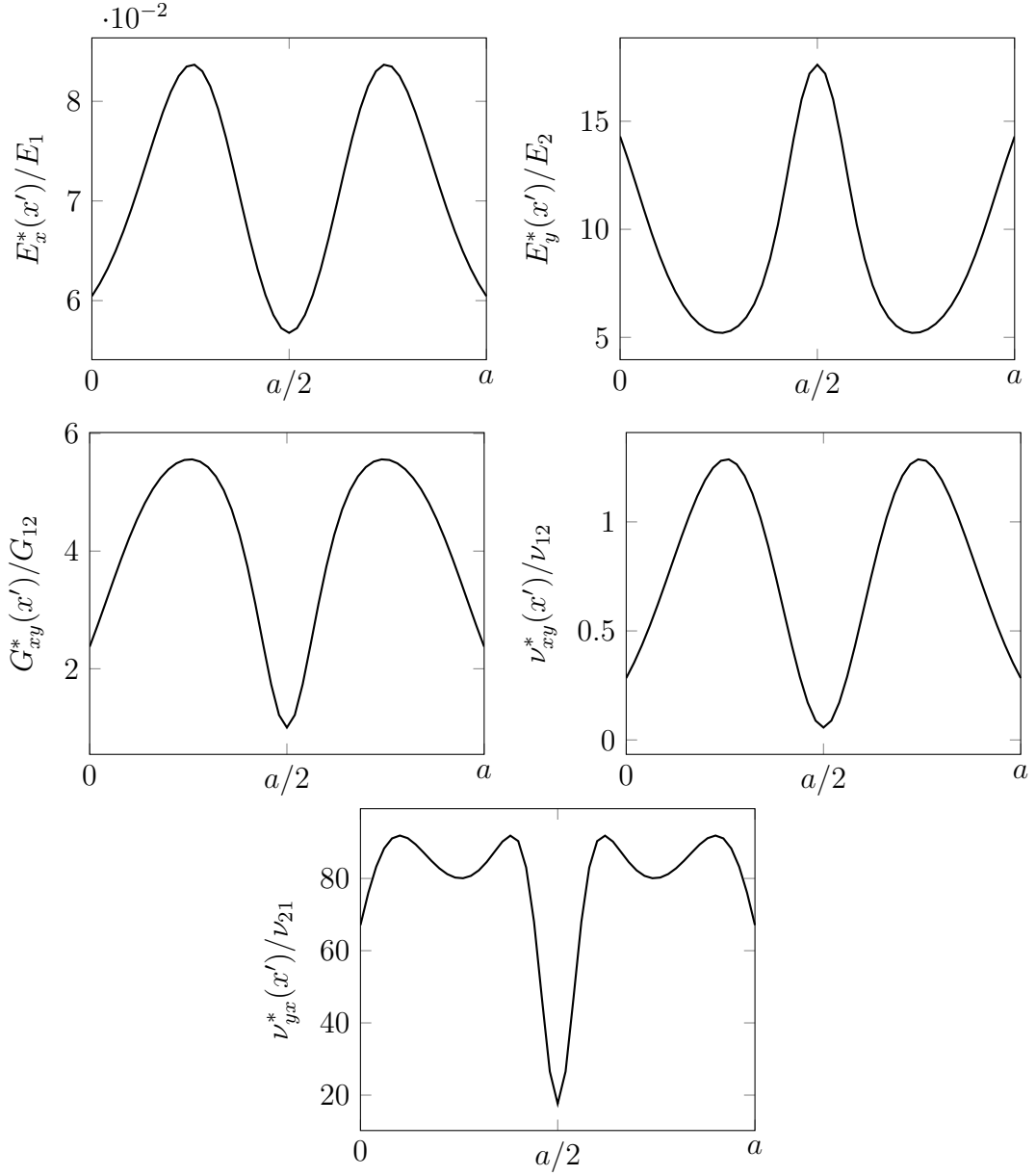Figure 4.9: Effective material properties for the laminate $[0° \pm \langle 75°|30° \rangle]_{3S}$.

Figure 4.10: Effective material properties for the laminate $[0° \pm \langle 90°|60°|60°|75°\rangle]_{3S}$.

4.1.2 Case II

In the same way as in case I, the normalized u displacement for case II also presents a non-linear curve shape (Figs. 4.11 and 4.12), in addition, it varies only in the x direction as well (Fig. 4.13). Comparing the u displacement of the laminates $[0° \pm \langle 0°|45°\rangle]_{3S}$ and $[0° \pm \langle 45°|0°\rangle]_{3S}$, it is possible to notice that when $T_1 = 45°$ the curve is convex and when $T_1 = 0°$ the curve is concave. This behavior is expected for these laminates due to the fact that when $T_1 = 0°$, the panel is more compliant at its edges, and then the curve slope is lower compared to $T_1 = 45°$. The same behavior can be seen when compared the laminates $[0° \pm \langle 45°|90°\rangle]_{3S}$ and $[0° \pm \langle 90°|45°\rangle]_{3S}$. For the cubic angle variation, one can notice that the laminates $[0° \pm \langle 90°|75°|60°|90°\rangle]_{3S}$, $[0° \pm \langle 90°|60°|60°|75°\rangle]_{3S}$, and
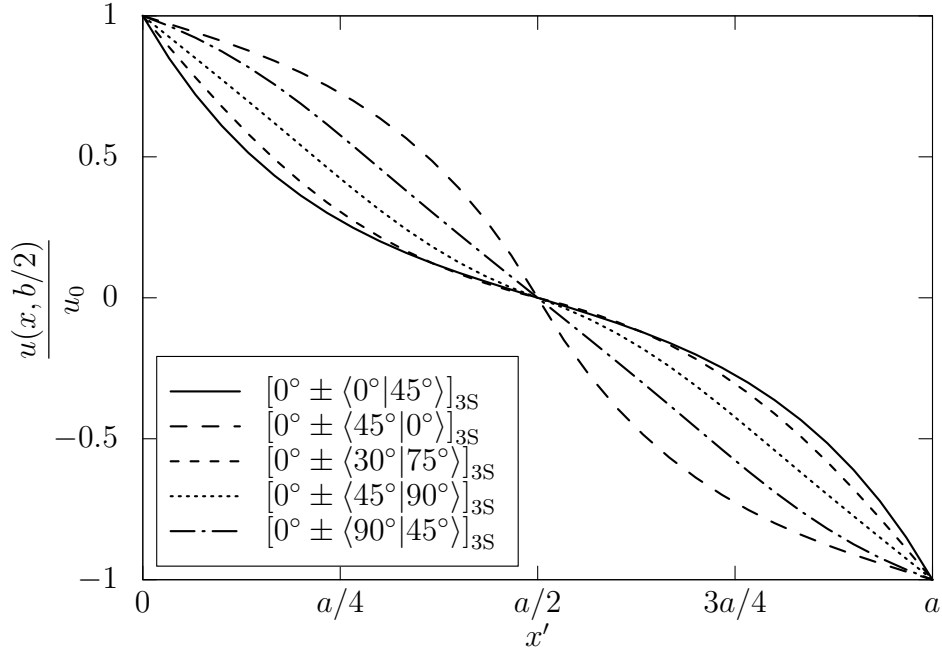
Figure 4.11: u displacement for case II with linear angle variation, aspect ratio $(a/b) = 1$ and $\phi = 0°$.

$[0° \pm \langle 45°|30°|30°|45°\rangle]_{3\mathrm{S}}$ have a similar displacement field, approximating to a constant stiffness laminate. This can be explained due to the fact that these laminates do not present a large difference between their angles, mainly the difference between the angles T_0 and T_3, so they u displacement field is similar to the laminates with constant angle.

As the transverse edges for the case II are free to deform, the v displacement field is not zero, it depends on v_{xy} and $\partial u/\partial x$, and both varies with x. In Fig. 4.14 is shown the normalized v displacement evaluated at bottom transverse edge. To study the influence of the angles T_0 and T_1 on the v displacement, the laminates $[0° \pm \langle 0°|45°\rangle]_{3\mathrm{S}}$ and $[0° \pm \langle 45°|0°\rangle]_{3\mathrm{S}}$ are good candidates. The main difference between the v displacement of each is the convexity, and it is directly proportional to the Poisson's ratio ν_{xy}. The panel $[0° \pm \langle 0°|45°\rangle]_{3\mathrm{S}}$ has a large Poisson's ratio is greater at its edges, as a consequence of this, it has a greater displacement at $x = 0$ and $x = a$. For the laminate $[0° \pm \langle 45°|0°\rangle]_{3\mathrm{S}}$, the opposite is true, as can be seen in Fig. 4.14. For cases in which the difference $T_0 - T_1$ is small, the convexity is not very expressive, as can be seen in Fig. 4.16.

For the cubic angle variation case (Fig. 4.15), it is also true that the convexity depends on angle difference. The laminate $[0° \pm \langle 45°|45°|60°|60°\rangle]_{3\mathrm{S}}$, for example, presents, basically, a flat curve. In contrast with it, the panel $[0° \pm \langle 90°|60°|60°|75°\rangle]_{3\mathrm{S}}$ shows a small bulge at its center. Comparing the linear and cubic angle variation cases, one can notice that for the cubic case is possible different convexity shapes in the interval $0 \leqslant x \leqslant a/2$, as shown in Fig. 4.17. The both panel have the same angle its center and edges, however the v displacement is different. The panel with cubic angle variation presents a convex curve shape near its edges and a bugle at its center. while for linear variation it presents
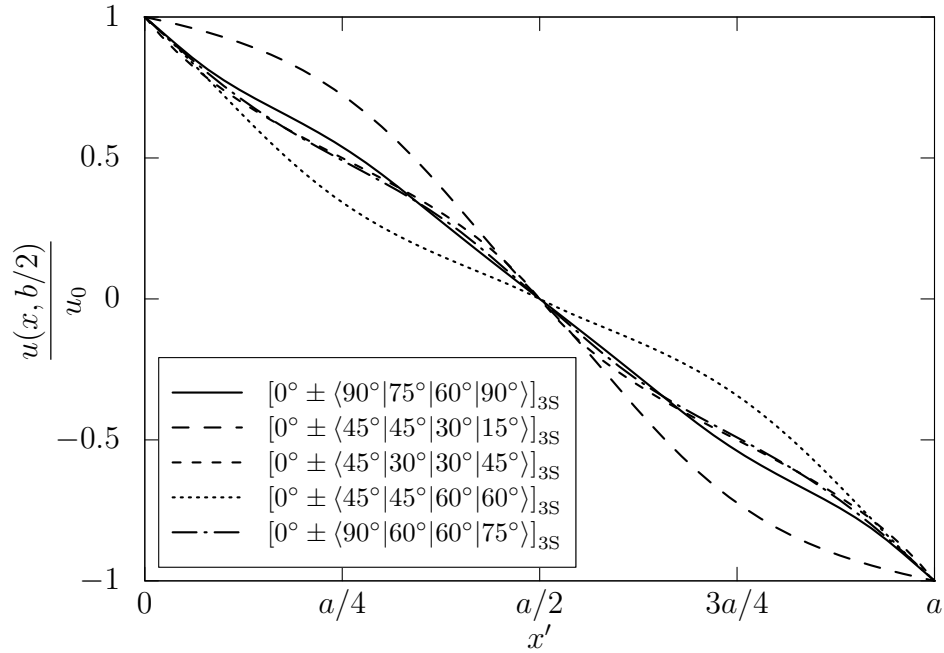
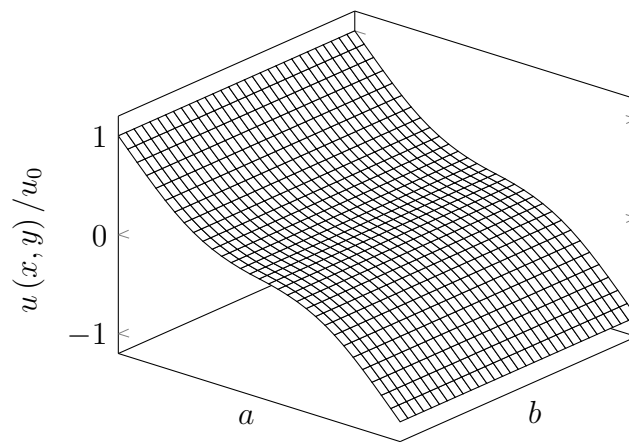Figure 4.12: u displacement for case II with cubic angle variation, aspect ratio $(a/b) = 1$ and $\phi = 0°$.

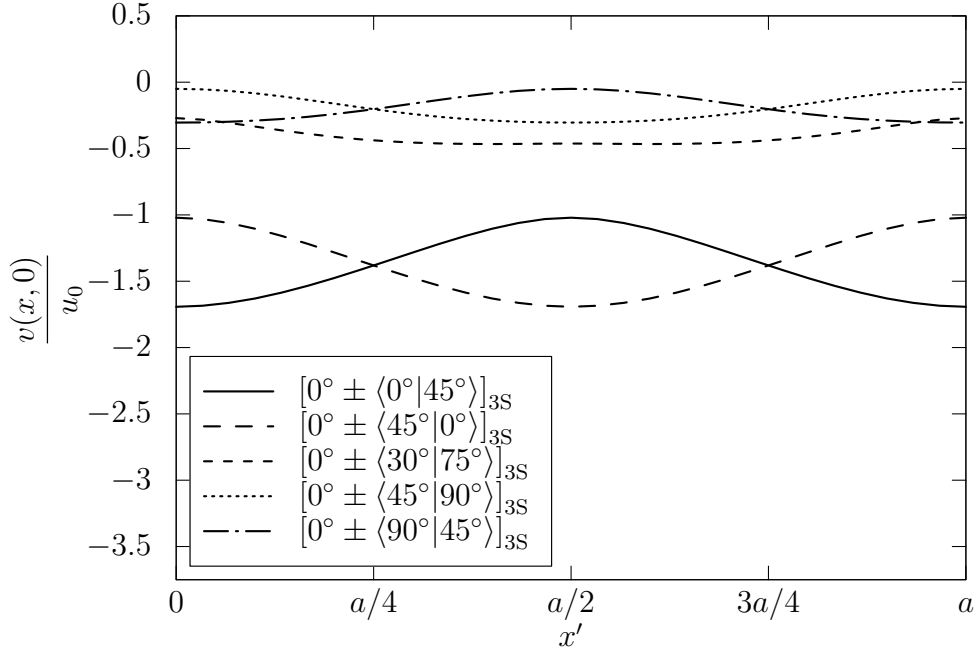Figure 4.13: u displacement for the laminate $[0° \pm \langle 45°|90°\rangle]_{3S}$.

Figure 4.14: v displacement for case II with linear angle variation, aspect ratio $(a/b) = 1$ and $\phi = 0°$.

only a bulge along the x domain.

To a better comprehension of the behavior of panels for the case II, it was analyzed the stress resultants $\bar{N}_x$, $\bar{N}_{xy}$ and $\bar{N}_y$. Unlike case I, $\bar{N}_x$ is not constant, it varies in x and y direction, in the same way that $\bar{N}_{xy}$ and $\bar{N}_y$. To compare the linear and cubic angle variation, it was evaluated the layups $[0° \pm \langle 45°|75° \rangle]_{3S}$ and $[0° \pm \langle 45°|60°|75°|75° \rangle]_{3S}$. One can notice that the panel has the same angles at its edges and center for both linear and cubic variation. As the edges are more compliant compared to the center, the largest strains occurs at $x = 0$ and $x = a$, and at center the panel is stiffer, creating a relatively uniform, as shown in Fig. 4.18.

One can notice that for a linear angle variation the resultant is bigger than for the cubic one. The difference between the maximum and minimum is equals to 23 and 37.5%, respectively. This variation can be explained due to the fact that in the interval $0 < x < a/2$ the plate with cubic angle variation shows less deformation, $\partial u/\partial x$, in the x direction, when compared to linear variation. The distribution of $\bar{N}_y$ is shown in Fig. 4.19. As can be seen, at panel center there is a compressive stress while tensile stress resultants appear near $x = 0$ and $x = a$.

To understand this behavior is important to analyze the $\bar{N}_{xy}$ and the Eq. 2.39. The distribution of $\bar{N}_{xy}$ is shown in Fig. 4.20. In order to satisfies the Eq. 2.39, $\bar{N}_y$ must be a compressive resultant at center. For the panel with a cubic angle variation, one can notice that at the center of the panel the compressive resultant $\bar{N}_y$ is more severe for cubic variation. This behavior can be addressed by how the angle function varies along the x direction (Fig. 4.21). It can be seen that for cubic variation there is a slight grow
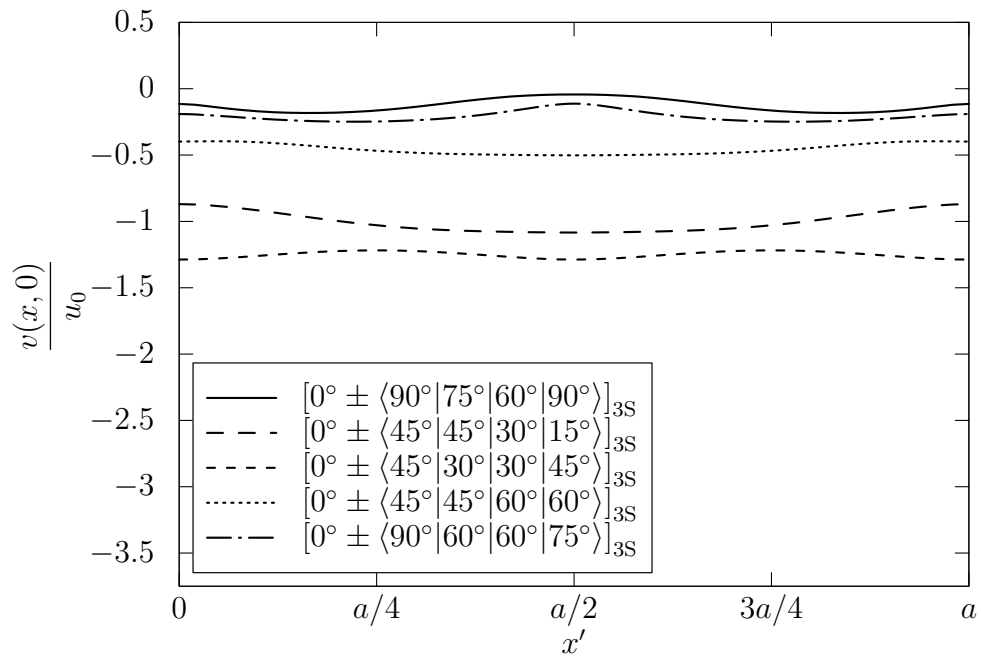
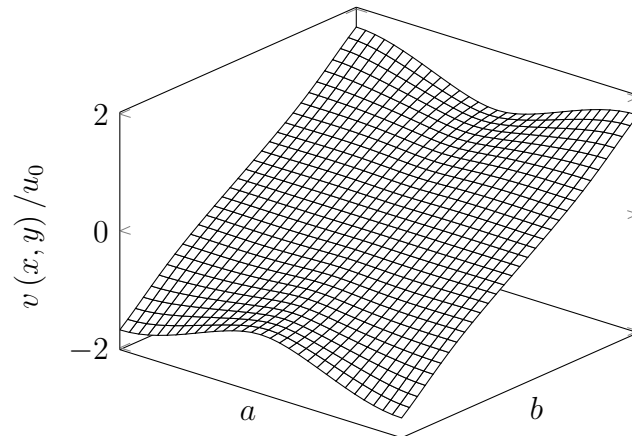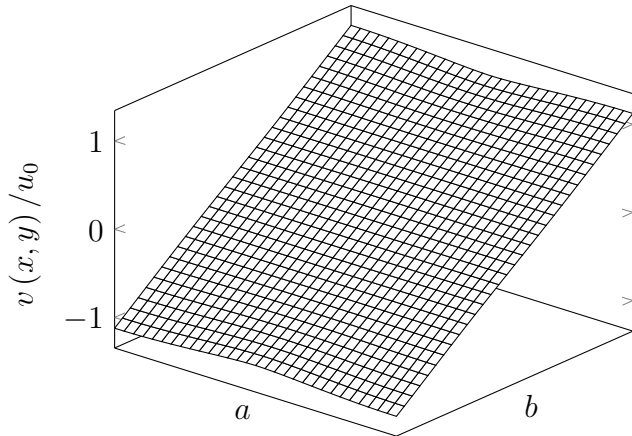Figure 4.15: v displacement for case II with cubic angle variation, aspect ratio $(a/b) = 1$ and $\phi = 0°$.

(a) $[0° \pm \langle 0°|45° \rangle]_{3S}$

(b) $[0° \pm \langle 30°|45° \rangle]_{3S}$

Figure 4.16: v displacement for two different laminates.

Figure 4.17: Comparison between v displacement for cubic and linear angle variation of laminates presenting the same angles at its center and edge.

in the angle function. It causes near the panel edges a more compliant region. Thus, it explains the differences in the stress resultant N_y between them.

(a) $[0° \pm \langle 45°|75° \rangle]_{3S}$

(b) $[0° \pm \langle 45°|60°|75°|75° \rangle]_{3S}$

Figure 4.18: Comparison between $\bar{N}_x$ for cubic and linear angle variation of laminates presenting the same angles at its center and edge.

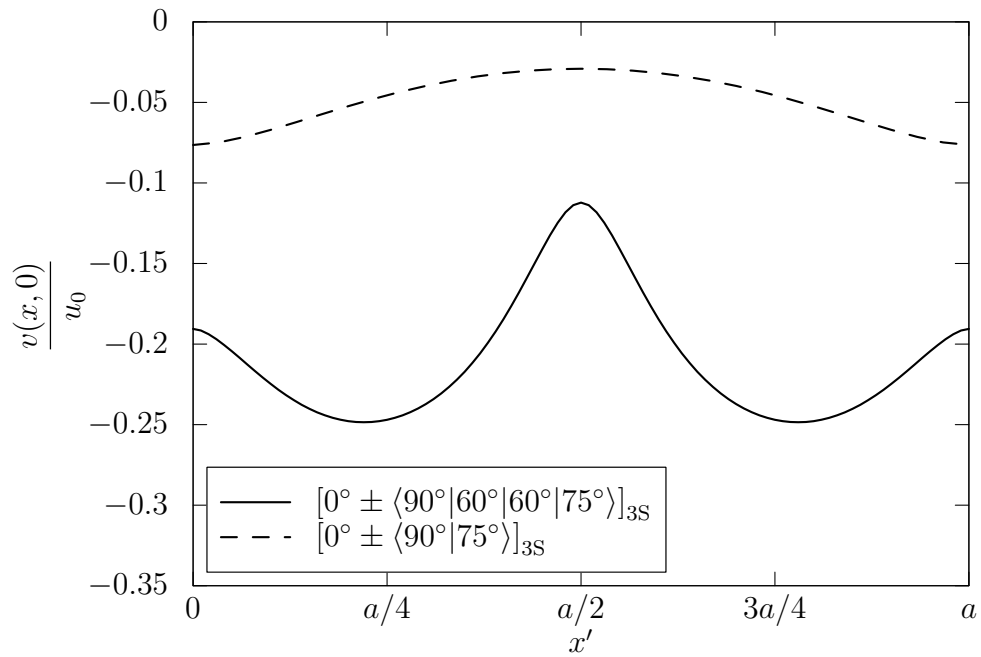(a) $[0° \pm \langle 45°|75°\rangle]_{3S}$ (b) $[0° \pm \langle 45°|60°|75°|75°\rangle]_{3S}$

Figure 4.19: Comparison between $\bar{N}_y$ for cubic and linear angle variation of laminates presenting the same angles at its center and edge.

(a) $[0° \pm \langle 45°|75°\rangle]_{3S}$ (b) $[0° \pm \langle 45°|60°|75°|75°\rangle]_{3S}$
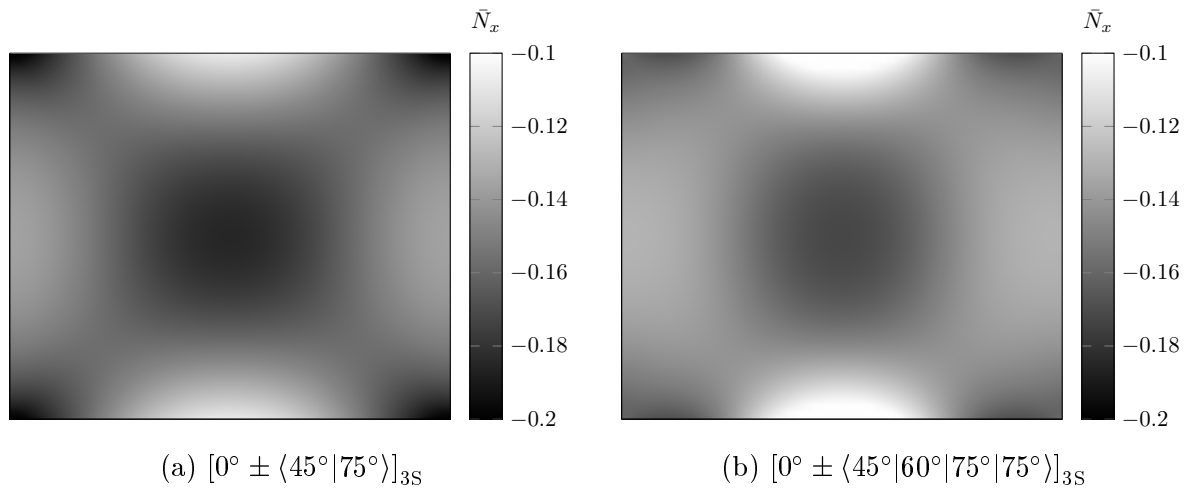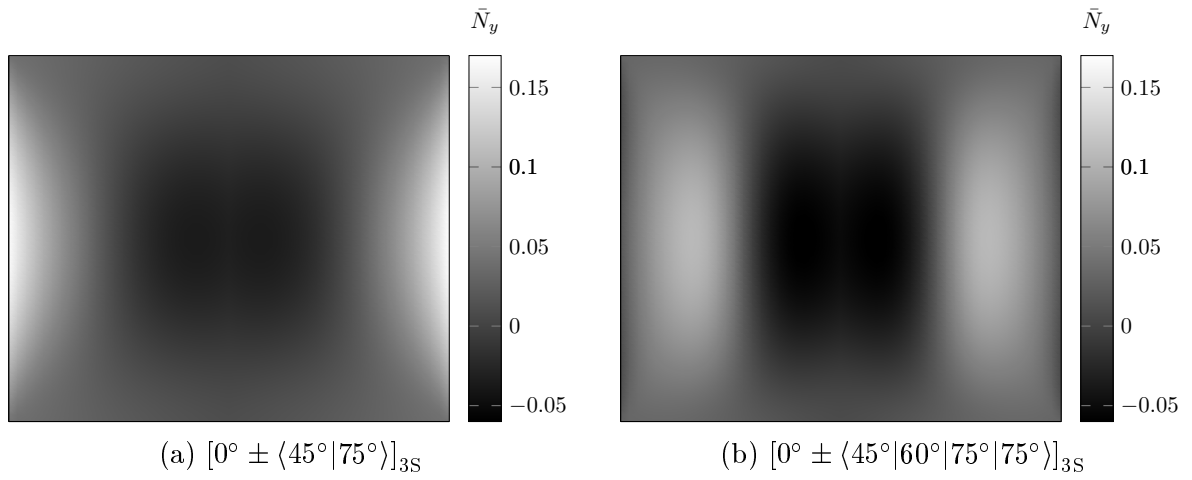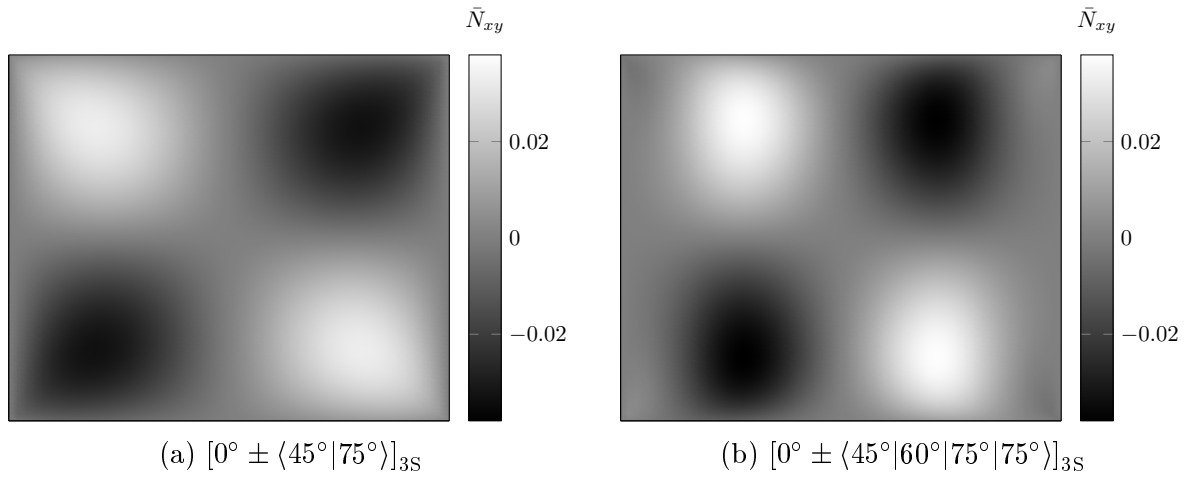
Figure 4.20: Comparison between $\bar{N}_{xy}$ for cubic and linear angle variation of laminates presenting the same angles at its center and edge.
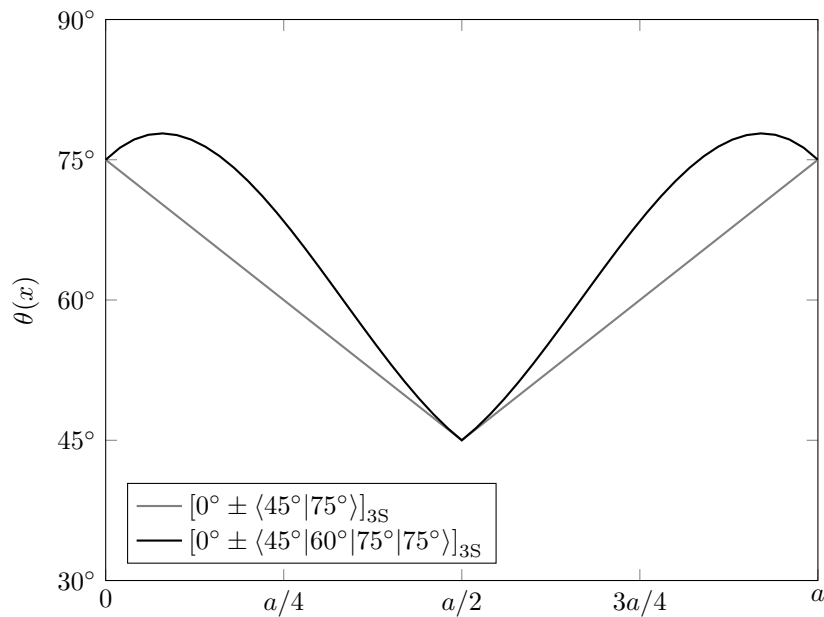
Figure 4.21: Comparison between $\theta(x)$ for cubic and linear angle variation of laminates presenting the same angles at its center and edge.

4.2 Buckling results and discussion

4.2.1 Model Validation

The model was validated for linear angle variation through both experimental and numerical studies. Marouene et al. (2016) manufactured two types of variable-stiffness panels: one variable-stiffness with complete overlaps (i.e., 100% coverage) and another with complete gaps (i.e., 0% coverage), shown in Fig. 4.22. The fiber-steered panels were manufactured using a VIPER® AFP machine. To avoid wrinkles and micro-buckling, the authors considered a minimum radius curvature of 635 mm, the same value considered in this work. As the model of this work does not consider the thickness variation over the plate, it was considered the panels with a average thickness. The panel's mechanical properties are shown in Tab. 4.2. The layup and geometric features are shown in Tab. 4.3.

The mounting fixture used was able to obtain the simply-supported edge-boundary conditions along all the four edges of the panels. The horizontal top edge was subjected to uniaxial compression by applying a uniform displacement and the other edge was fixed. More details can be found in Marouene et al. (2016). The results are shown in Tab. 4.4.

The case of panels with gaps, the present model underestimated the result, showing a difference of 28.71% from the experimental result. On the other hand, for the case with overlaps, the model overestimated, presenting a difference of 8.84%. These results shown that the gaps present a important role in the results, while overlaps not so much. In fact, to capture all effects involved on this kind of experiment, it is necessary a non-linear model, specially for the case presenting gaps. As the present model considers a constant
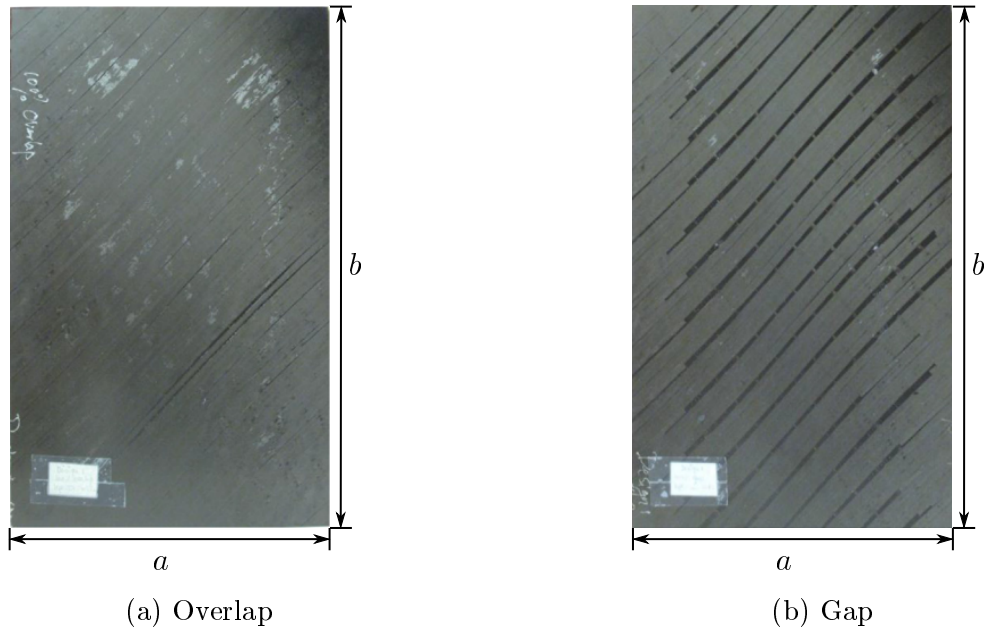
(a) Overlap   (b) Gap

Figure 4.22: Specimens tested experimentally. Adapted from Marouene et al. (2016)
.

thickness variation, it approximates to the panel with overlaps. Thus, considering the difference of 8.84%, the model has a good agreement with the experimental results.

Table 4.2: G40-800/5276-1 unidirectional carbon/epoxy prepreg.

Moduli parameters	G40-800/5276-1
Longitudinal modulus (E_1)	142.7 GPa
Transverse modulus (E_2)	9.1 GPa
In-plane shear modulus (G_{12})	4.82 GPa
Major Poisson's ratio (ν_{12})	0.3

Table 4.3: Panel features

Layup	$[0° \pm \langle 49°|41°\rangle/ \pm \langle 48°|61°\rangle/ \pm \langle 57°|73°\rangle/ \pm \langle 72°|77°\rangle]_\mathrm{S}$
Thickness (average)	Overlap = 2.84 mm and gap = 2.09 mm
Dimensions	$a = 254$ mm and $b = 406$ mm

Table 4.4: Comparison between the results from Marouene et al. (2016) and the present work.

	Overlap	Gap
Marouene et al. (2016)	18.97 kN	15.06 kN
Present	20.81 kN	8.69 kN
Difference	8.84%	28.71%

In order to validate the model numerically, the model was tested through the results from Gürdal, Tatting & Wu (2008). Gürdal, Tatting & Wu (2008) evaluated laminates

considering two boundary conditions, as evaluated in the work: one in that the transverse edges are restrained (case I) and another with the transverse edges free to deform (case II). It was calculated the values of N_{cr} for a family of curves corresponding to various values of T_0 from $0°$ to $90°$ with increments of $10°$. Each curve was generated by varying the value of T_1 between $0°$ and $90°$ for a given value of T_0.

The results for the case I, $a/b = 1$, are shown in Fig. 4.23. For this case, $\phi = 0°$. According to results calculated, the maximum value of N_{cr} is 1.43, a difference of 0.38% from the results of Gürdal, Tatting & Wu (2008), for the laminate $[0° \pm \langle 0°|50° \rangle]_{3S}$. The results for the case II, $a/b = 1$, are shown in Fig. 4.24. The case II was evaluated for $\phi = 90°$. The maximum value of N_{cr}, equals to 3.16, happened for the laminate $[90° \pm \langle 0°|75° \rangle]_{3S}$. This value is only 0.64% higher than the value of 3.14 from the results of Gürdal, Tatting & Wu (2008). In order to compare a range of values, it was compared the results from (GÜRDAL; TATTING; WU, 2008) for $T_0 = 0°$, as shown in Fig. 4.25. In light of the results, it can considered that the model is reliable.
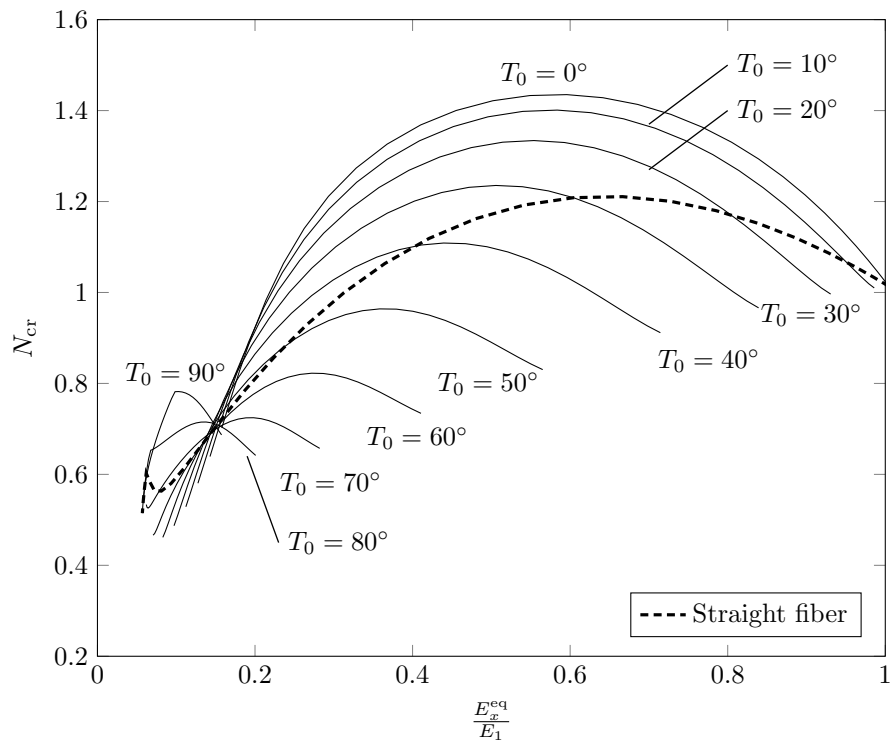

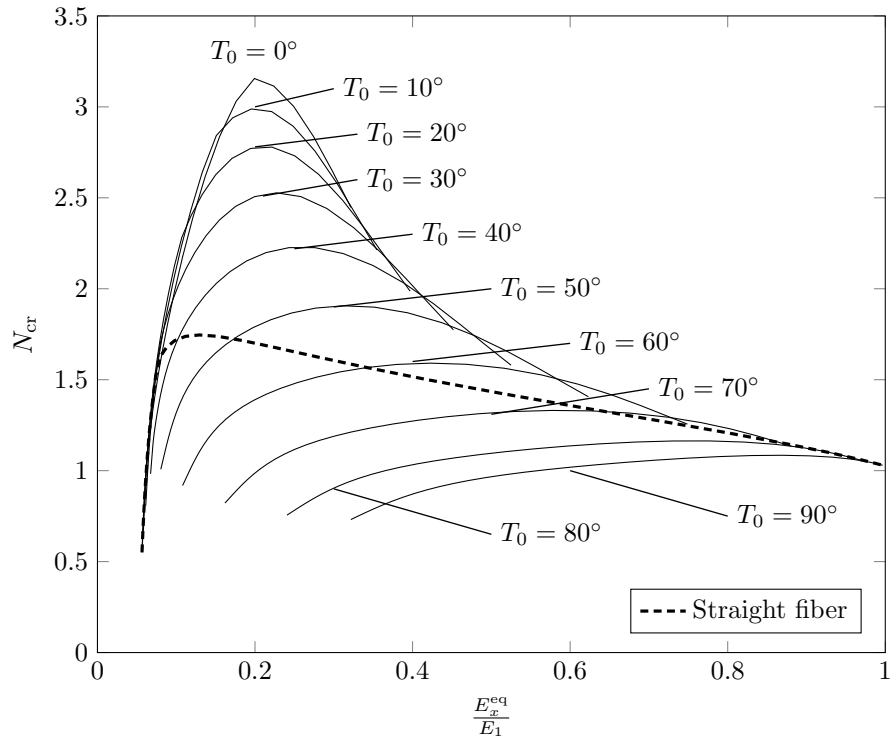Figure 4.23: Buckling and equivalent stiffness of various laminates with transverse edges restrained.

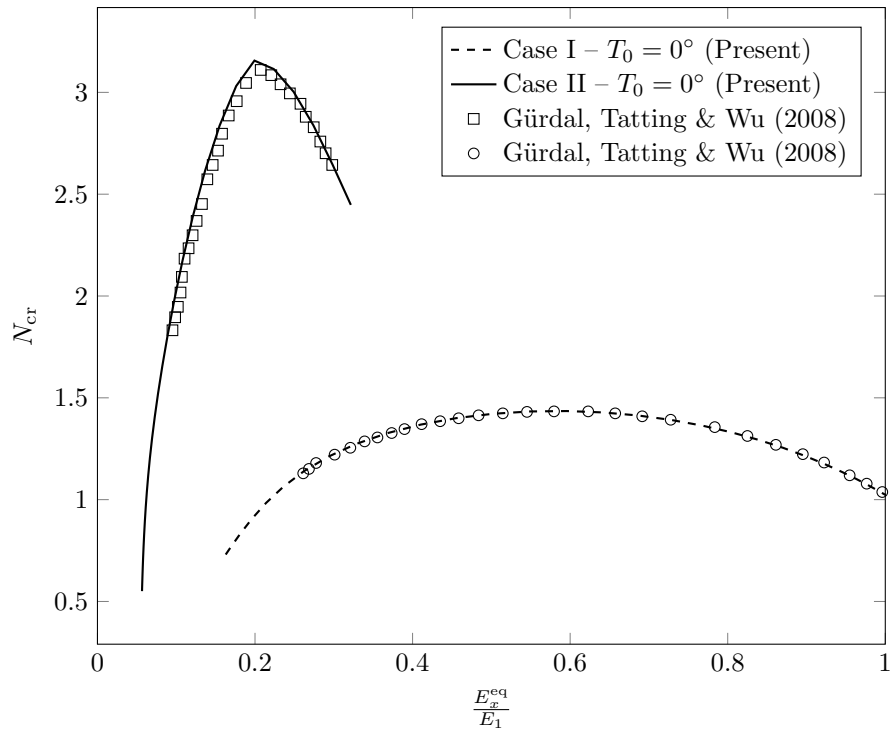Figure 4.24: Buckling and equivalent stiffness of various laminates with transverse edges free.

Figure 4.25: Comparison for different values of N_{cr}.

4.2.2 Case I

The results for case I boundary conditions is shown in this section. For linear and cubic angle variation, T_i ($i = 1, 2, 3$ or 4) was allows to vary from $0°$ to $90°$, with increments of $10°$. It was evaluated N_{cr} and E_x^{eq} for aspect ratios equals to 0.5, 1, 2 and 3. Besides that, it was compared the results for $\phi = 0°$ and $\phi = 90°$. The results of the highest values of N_{cr} for each aspect ratio and the corresponding E_x^{eq} are shown in Figs. 4.26 and 4.26. The layup of the highest value of N_{cr} for each aspect ratio is shown in Tab. 4.5. All layups shown in Tab. 4.5 present $\kappa_{\max} < \kappa_{\mathrm{crit}}$.

For $\phi = 0°$ the values of N_{cr} are practically the same for all aspect ratios for both linear and cubic angle variation. The largest difference occur for $a/b = 3$, it being the N_{cr} for cubic variation 2.4% higher. However, the ratio E_x^{eq}/E_1 for cubic variation is 5.63%, indicating that the panel with cubic angle variation is more compliant than the linear variation one. Solely for $a/b = 0.5$ the ratio E_x^{eq}/E_1 for the cubic variation is greater than the linear one, 2.13%. This can be explained due to the fact that the cubic variation layup for $a/b = 0.5$ represents a straight fiber in the x direction, while the layup for the linear varies linearly from $20°$ at its edges to $0°$ at its center.

To understand the difference observed for the N_{cr} values between the linear and cubic variation for $a/b = 3$, it is compared the behavior of N_y, shown in Fig. 4.28. As can be seen, N_y for cubic variation is more flat at panel center compared to the N_y for linear variation. This impact directly on matrix $\mathbf{M}$ of the Eq. 2.47, yielding a higher value of λ_{cr}. Besides that, for $a/b = 3$, N_x of the cubic variation is 5.94% smaller than that of linear variation.

For $\phi = 90°$, the values of N_{cr} for $a/b = 0.5$ is identical, as they should be, considering that the linear and cubic variation have the same layup. For $a/b = 1$, the cubic layup present a value of N_{cr} 1.45% greater, followed by a difference of 13% and 18.33% for $a/b = 2$ and 3, respectively. In the same way for $\phi = 0°$, the greater difference occurs when $a/b = 3$. However, for $\phi = 90°$, this difference is significantly more pronounced. In Fig. 4.29 is compared the N_x for linear and cubic variation. It is important to notice that when $\phi = 90°$, θ is function of y, i.e. $\theta(y)$. In a similar way to $\phi = 0°$, for a cubic variation N_x is more flat at panel's center, and N_y is 12.7% smaller than the linear variation.

Regarding the ratio E_x^{eq}/E_1, for $a/b = 0.5$ the value is the same for both linear and cubic variation, as expected. For $a/b = 1$, the cubic variation presented a value that is 8.57% greater than that for a linear variation. For $a/b = 2$ and 3, E_x^{eq}/E_1 for cubic variation is 12.25% smaller. As the panels for linear and cubic variation present similar angles at its edges and center, the difference in E_x^{eq}/E_1 is not so much expressive. Figure 4.30 shows the values of N_{cr} and the corresponding ratio E_x^{eq}/E_1 for T_0 ranging from $0°$ to $90°$ with increments of $10°$ for $a/b = 2$ and $\phi = 0°$, in the same manner that was made in the work of Gürdal, Tatting & Wu (2008). For $a/b = 3$ the curves are similar and for

Table 4.5: Best layups for each aspect ratio evaluated for case I.

(a/b)	$\phi = 0°$		$\phi = 90°$	
	Linear	Cubic	Linear	Cubic
0.5	$[\pm\langle 0°\|20°\rangle]_{3\mathrm{S}}$	$[\pm\langle 0°\|0°\|0°\|0°\rangle]_{3\mathrm{S}}$	$[\pm\langle 90°\|90°\rangle]_{3\mathrm{S}}$	$[\pm\langle 90°\|90°\|90°\|90°\rangle]_{3\mathrm{S}}$
1	$[\pm\langle 0°\|40°\rangle]_{3\mathrm{S}}$	$[\pm\langle 10°\|20°\|30°\|40°\rangle]_{3\mathrm{S}}$	$[\pm\langle 20°\|70°\rangle]_{3\mathrm{S}}$	$[\pm\langle 30°\|40°\|50°\|80°\rangle]_{3\mathrm{S}}$
2	$[\pm\langle 0°\|50°\rangle]_{3\mathrm{S}}$	$[\pm\langle 0°\|10°\|40°\|40°\rangle]_{3\mathrm{S}}$	$[\pm\langle 30°\|80°\rangle]_{3\mathrm{S}}$	$[\pm\langle 30°\|40°\|60°\|90°\rangle]_{3\mathrm{S}}$
3	$[\pm\langle 0°\|40°\rangle]_{3\mathrm{S}}$	$[\pm\langle 0°\|10°\|30°\|40°\rangle]_{3\mathrm{S}}$	$[\pm\langle 30°\|80°\rangle]_{3\mathrm{S}}$	$[\pm\langle 30°\|40°\|60°\|90°\rangle]_{3\mathrm{S}}$

$a/b = 0.5$ and 1, the curves are not continuous due to $\kappa_{\max} > \kappa_{\mathrm{crit}}$. For this reason, they were omitted. As for $\phi = 90°$ the fiber angle is function of y, $\theta(y)$, and the dimension b keeps constant, the curves also are not continuous and were omitted.
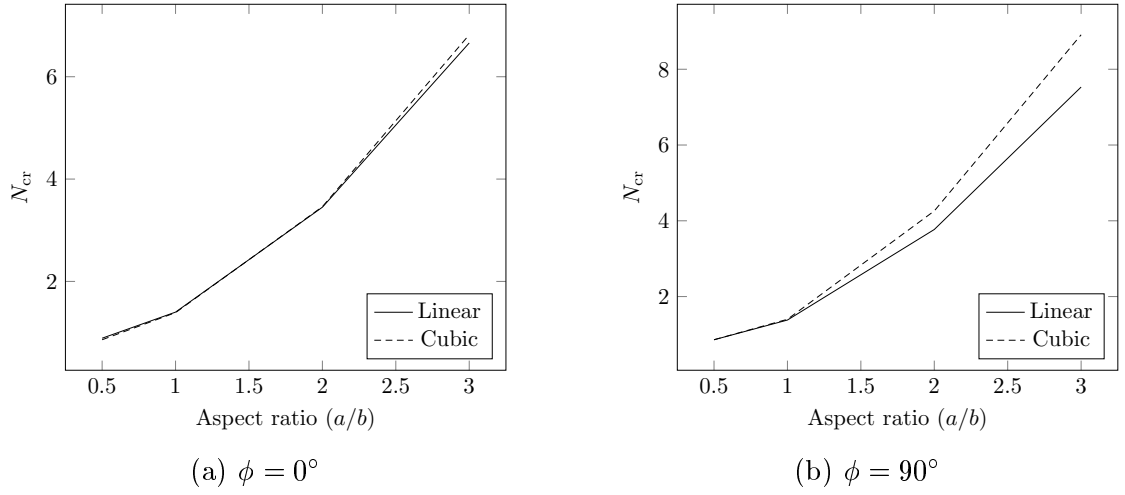

(a) $\phi = 0°$ (b) $\phi = 90°$

Figure 4.26: Buckling performance comparison between cubic and linear angle variation for case I.
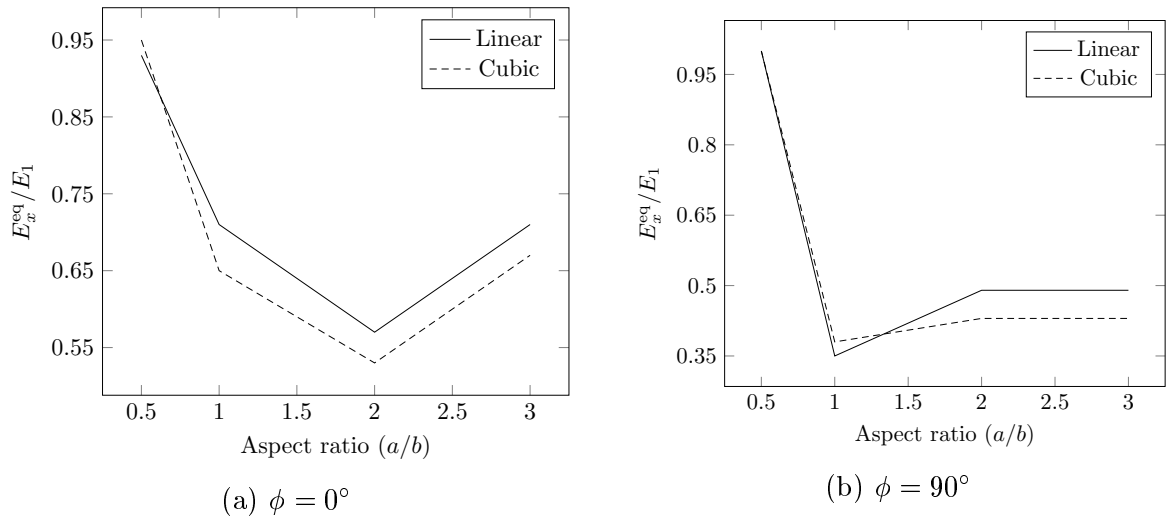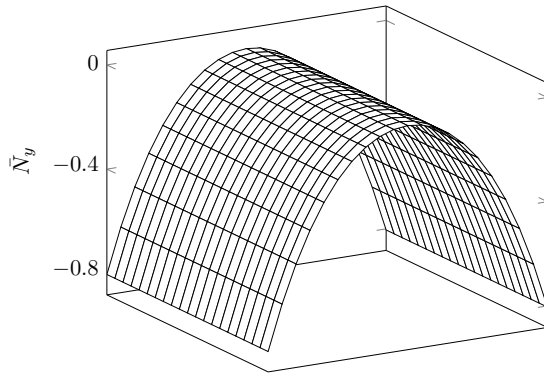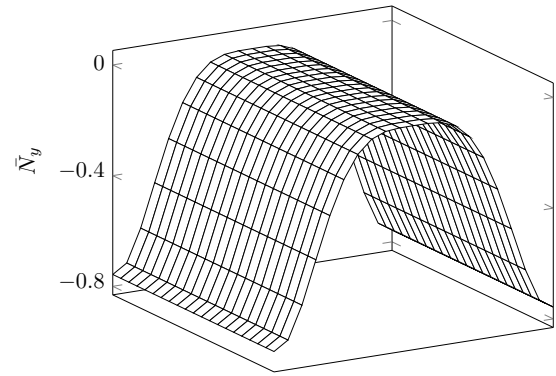

(a) $\phi = 0°$ (b) $\phi = 90°$

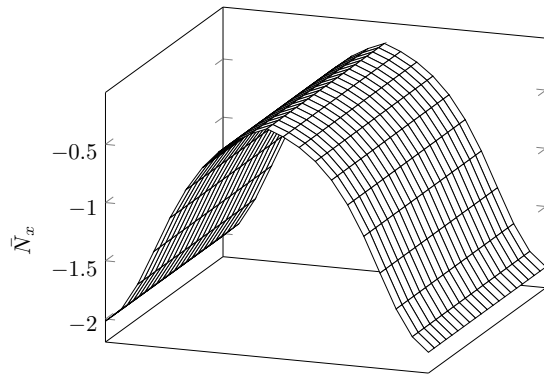Figure 4.27: Equivalent stiffness performance comparison between cubic and linear angle variation for case I.
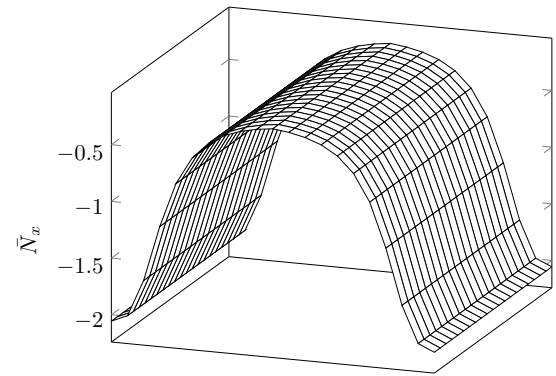
(a) Linear

(b) Cubic

Figure 4.28: $\bar{N}_y$ of the best laminates for $a/b = 3$ and $\phi = 0°$.

(a) Linear

(b) Cubic

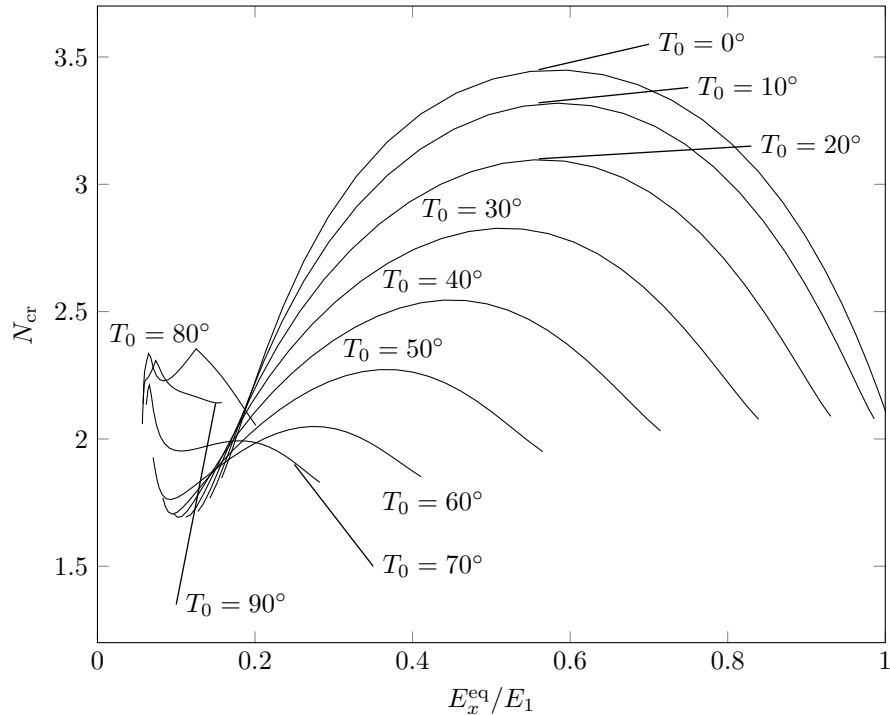Figure 4.29: $\bar{N}_x$ of the best laminates for $a/b = 3$ and $\phi = 90°$.

Figure 4.30: Normalized critical buckling load and equivalent stiffness of various laminates with $a/b = 2$ and $\phi = 0°$ for case I.

4.2.3 Case II

In the same manner as case I, T_i ($i = 1, 2, 3$ or 4) was allows to vary from $0°$ to $90°$, with increments of $10°$. It was evaluated N_{cr} and E_x^{eq} for aspect ratios equals to 0.5, 1, 2 and 3. It was compared the results for $\phi = 0°$ and $\phi = 90°$. Figure 4.31 shows the values of N_{cr} for $\phi = 0°$ and $90°$. It can be seen that for $\phi = 0°$ the values of N_{cr} are basically the same for both linear and cubic variation. These results can be addressed through the panels' layups shown in Tab. 4.6.

It is noticeable that the difference between the angles is not greater than $10°$, except for the layup $[0° \pm \langle 0°|20°\rangle]_{3S}$ for $a/b = 0.5$. Thus, N_x of this laminate presents a small variation when compared to straight fiber laminate $[\pm\langle 0°|0°|0°|0°\rangle]_{3S}$. The difference between the value of N_{cr} is 2.3% greater for linear variation. For $a/b = 1$, 2 and 3, the layups are similar, changing only the angles at the edges and center of the panel from $40°$ to $50°$. Even for the cubic angle variation, the angles between the center and edge, T_1 and T_2, are equal. Figure 4.32 shows N_x for the laminates $[0° \pm \langle 50°|40°\rangle]_{3S}$ and $[\pm\langle 40°|40°|40°|50°\rangle]_{3S}$. It can be noticed that N_x presents, basically, a constant value.

Regarding E_x^{eq}/E_1, the results are shown in Fig. 4.33. When $a/b = 0.5$, the laminate for the cubic variation is a straight fiber laminate in the x direction, thus E_x^{eq}/E_1 is equal to 1, as expected. For the linear variation case, E_x^{eq}/E_1 is 12% smaller than the cubic one. As for $a/b = 1$, 2 and 3 the laminates are similar, so the ratio E_x^{eq}/E_1 presents similar values as well. The difference between the linear and cubic variation is 18.18%, 13.33%

and 18.75% for $a/b = 1$, 2 and 3, respectively. Figure 4.30 shows the values of N_{cr} and the corresponding ratio E_x^{eq}/E_1 for the linear variation and $a/b = 2$. The same explanation about others aspect ratios for case I is valid here.

For $\phi = 90°$, there are differences between linear and cubic angle variation. When $a/b = 0.5$, for the linear variation, the laminate is in the x direction. Therefore, E_x^{eq}/E_1 is equal to 1. The laminate for the cubic variation is $[90° \pm \langle 50°|50°|60°|80° \rangle]_{3\mathrm{S}}$ and $E_x^{\mathrm{eq}}/E_1 = 0.34$. Regarding N_{cr}, for cubic variation N_{cr} is 3.45% higher than linear variation. When $a/b = 1$, the angles at edges and center are the same for linear and cubic variation. N_{cr} for cubic variation is 6.83% higher than for linear variation, while E_x^{eq}/E_1 is 10% smaller.

For $a/b = 2$, N_{cr} is 2.97% higher for cubic variation, as for E_x^{eq}/E_1 is 11.11% smaller. The angles are the same at center and at edges, as for $a/b = 1$. For $a/b = 3$, N_{cr} is 5.36% higher for cubic variation, as for E_x^{eq}/E_1 is 10% smaller. Figure 4.35 shows N_x of the laminates $[90° \pm \langle 20°|70° \rangle]_{3\mathrm{S}}$ and $[90° \pm \langle 30°|40°|50°|80° \rangle]_{3\mathrm{S}}$ for $a/b = 3$. It can be noticed that for the cubic variation N_x is more flat at the center of the panel as well, in the same manner that for case I.
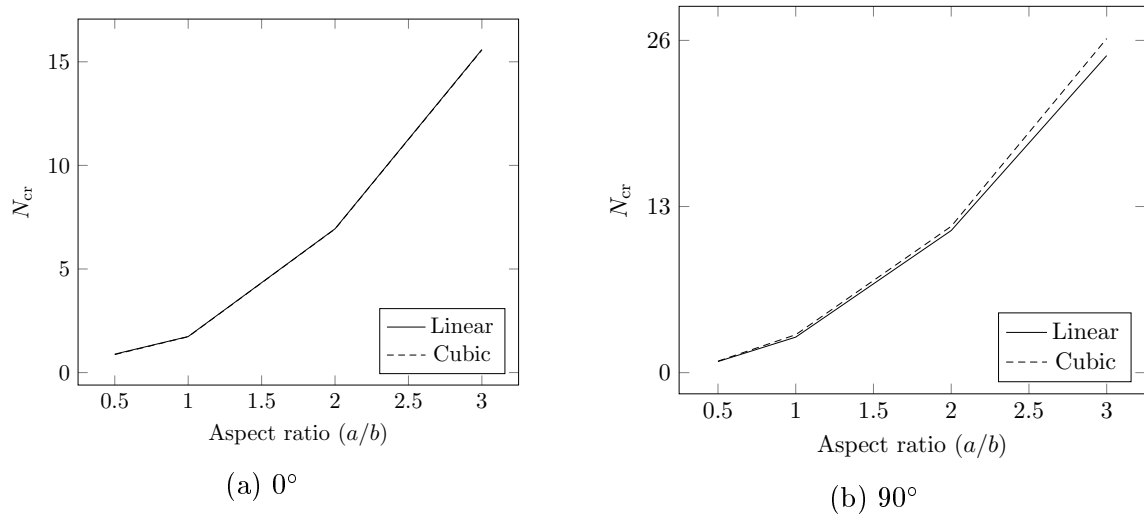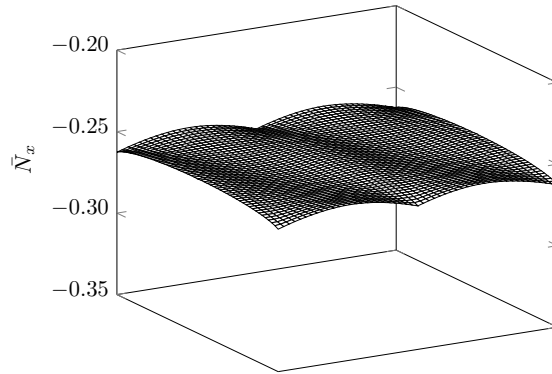

(a) 0°

(b) 90°

Figure 4.31: Buckling performance comparison between cubic and linear angle variation for case II.

Table 4.6: Best layups for each aspect ratio evaluated for case II.

| (a/b) | $\phi = 0°$ | | $\phi = 90°$ | |
	Linear	Cubic	Linear	Cubic
0.5	$[\pm\langle 0°|20°\rangle]_{3\mathrm{S}}$	$[\pm\langle 0°|0°|0°|0°\rangle]_{3\mathrm{S}}$	$[\pm\langle 90°|90°\rangle]_{3\mathrm{S}}$	$[\pm\langle 50°|50°|60°|80°\rangle]_{3\mathrm{S}}$
1	$[\pm\langle 40°|50°\rangle]_{3\mathrm{S}}$	$[\pm\langle 50°|50°|50°|40°\rangle]_{3\mathrm{S}}$	$[\pm\langle 20°|70°\rangle]_{3\mathrm{S}}$	$[\pm\langle 20°|30°|50°|70°\rangle]_{3\mathrm{S}}$
2	$[\pm\langle 50°|40°\rangle]_{3\mathrm{S}}$	$[\pm\langle 50°|40°|40°|50°\rangle]_{3\mathrm{S}}$	$[\pm\langle 20°|70°\rangle]_{3\mathrm{S}}$	$[\pm\langle 20°|30°|50°|70°\rangle]_{3\mathrm{S}}$
3	$[\pm\langle 50°|40°\rangle]_{3\mathrm{S}}$	$[\pm\langle 40°|40°|40°|50°\rangle]_{3\mathrm{S}}$	$[\pm\langle 20°|70°\rangle]_{3\mathrm{S}}$	$[\pm\langle 30°|40°|50°|80°\rangle]_{3\mathrm{S}}$

(a) Linear
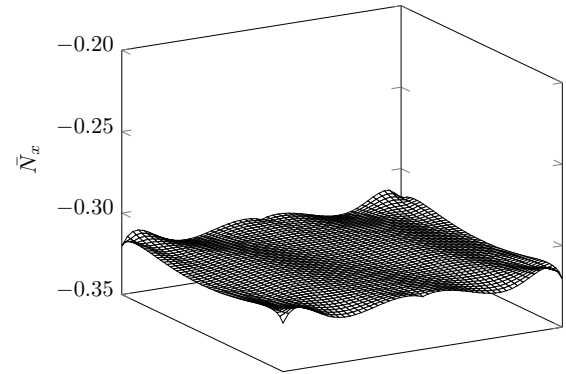
(b) Cubic

Figure 4.32: $\bar{N}_x$ of the best laminates for $a/b = 3$ and $\phi = 90°$.
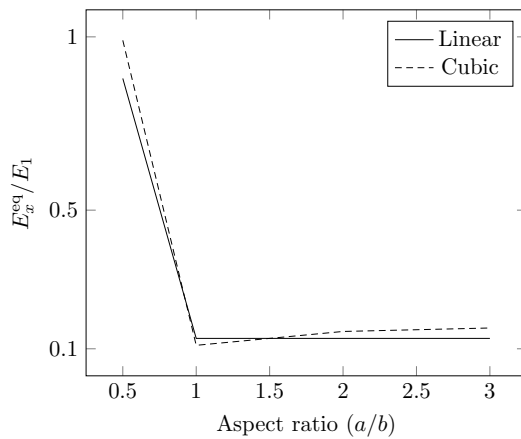
(a) 0°
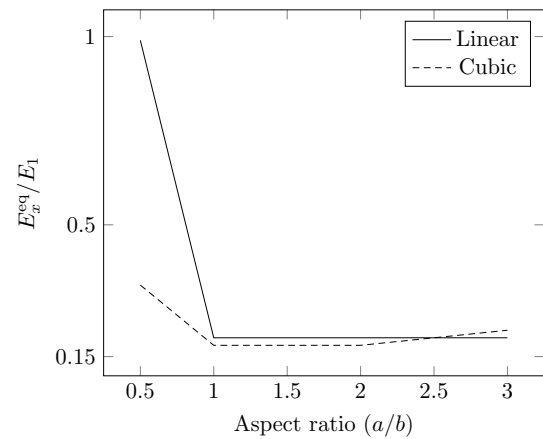
(b) 0°

Figure 4.33: Equivalent stiffness performance comparison between cubic and linear angle variation for case I.
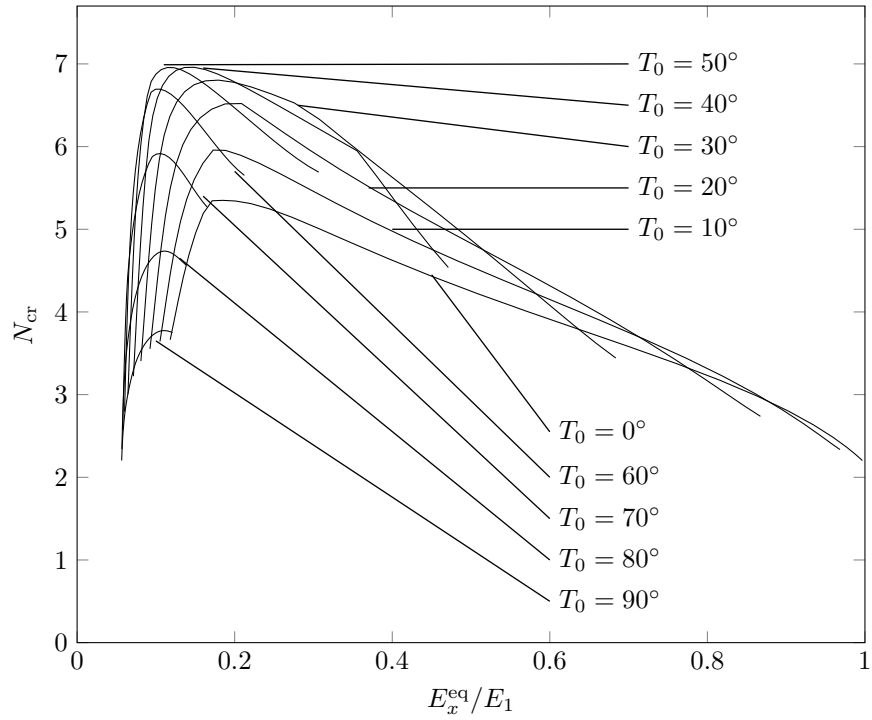
Figure 4.34: Normalized critical buckling load and equivalent stiffness of various laminates with $a/b = 2$ and $\phi = 0°$ for case II.
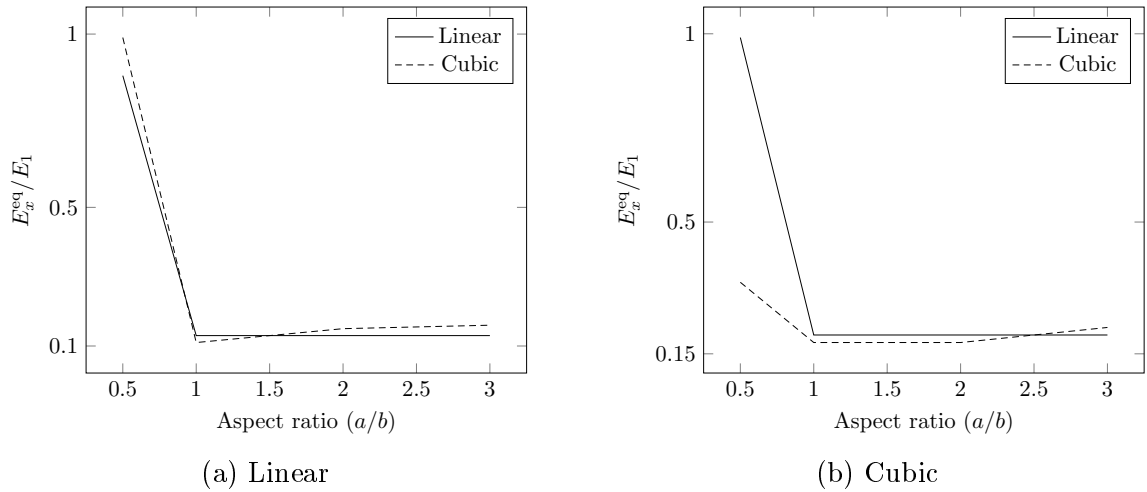

(a) Linear

(b) Cubic

Figure 4.35: $\bar{N}_x$ of thee best laminates for $a/b = 3$ and $\phi = 90°$.

Chapter 5

Concluding Remarks

This work presented a numerical investigation to identify the effects of cubic angle variation on the in-plane and buckling responses when compared to a linear angle variation of the panels with various aspect ratios. It was imposed a constraint based on manufacturing considerations to avoid fiber defects as wrinkles and micro-buckling. It was examined panels simply supported under applied uniform end shortening. Two boundary conditions were examined: the transverse edge fixed (case I) and free to deform (case II). Besides that, it was considered the fiber angle function varying along x and y direction, i.e., $\theta(x)$ and $\theta(y)$.

The results obtained indicate that a cubic angle variation allows more flexibility to tailor the resulting stress caused by the in-plane loads, although it is more prone to achieve high fiber curvature values that can be an important design constraint. Regarding the critical buckling load, the cubic angle variation for the panels with fixed transverse edges exhibits higher values (case I) when compared with the same panel presenting a linear angle variation. A more significant difference between the cubic and linear variation of the buckling load happens when a/b equals 3, and the fiber angle vary along y direction $(\theta(y))$. For $\phi = 0°$, the gains in the buckling load using a cubic variation is marginal, both for case I and II, being less expressive for case II.

For future work, it is recommended to take into account the thickness variations as it is known that the thickness is not constant, it depends directly on fiber angle function and plays an important role in stress resultant. For better results, it is also recommended to apply a numerical optimization technique to efficiently find the optimum angles.

Bibliography

AKHAVAN, H. *Non-linear vibrations of tow placed variable stiffness composite laminates.* Tese (Doutorado) — Universidade do Porto, 2015.

BLOM, A. *Structural Performance of Fiber-Placed, Variable-Stiffness Composite Conical and Cylindrical Shells.* Tese (Doutorado) — Technische Universiteit Delft, 2010.

BRINK, W. Van den; VANKAN, W.; MAAS, R. Buckling-optimized variable stiffness laminates for a composite fuselage window section. National Aerospace Laboratory NLR, 2012.

BROOKS, T. *Design Optimization of Flexible Aircraft Wings Using Tow-steered Composites.* Tese (Doutorado) — University of Michigan, 2018.

CAO, Z.; FU, H.; HAN, Z. Comparative study on bezier curve and linear variable angle method for variable stiffness laminates. *Polymer Composites*, Wiley Online Library, v. 40, n. 3, p. 952–960, 2019.

CAPRINO, G.; VISCONTI, I. C. A note on specially orthotropic laminates. *Journal of Composite Materials*, Sage Publications Sage CA: Thousand Oaks, CA, v. 16, n. 5, p. 395–399, 1982.

CLYNE, T.; HULL, D. *An introduction to composite materials.* Cambridge: Cambridge university press, 2019.

CROFT, K. et al. Experimental study of the effect of automated fiber placement induced defects on performance of composite laminates. *Composites Part A: Applied Science and Manufacturing*, Elsevier, v. 42, n. 5, p. 484–491, 2011.

DANIEL, I. M.; ISHAI, O. *Engineering mechanics of composite materials.* New York: Oxford university press, 2006.

DIRK, H.-J. L.; WARD, C.; POTTER, K. D. The engineering aspects of automated prepreg layup: History, present and future. *Composites Part B: Engineering*, Elsevier, v. 43, n. 3, p. 997–1009, 2012.

EVANS, D. O. Fiber placement. In: *Handbook of Composites.* Boston: Springer, 1998. p. 476–487.

FAYAZBAKHSH, K. *The impact of gaps and overlaps on variable stiffness composites manufactured by Automated Fiber Placement.* Tese (Doutorado) — PhD Thesis, McGill University, Canada, 2013.

FAYAZBAKHSH, K. et al. The effect of gaps and overlaps on the in-plane stiffness and buckling load of variable stiffness laminates made by automated fiber placement. In: ECCM. *Proceedings of 15th European Conference on Composite Materials*. Venice, Italy, 2012. p. 8.

FAYAZBAKHSH, K. et al. Defect layer method to capture effect of gaps and overlaps in variable stiffness laminates made by automated fiber placement. *Composite Structures*, Elsevier, v. 97, p. 245–251, 2013.

GRANT, C. Fiber placement process utilization within the worldwide aerospace industry. In: SAMPE. *SAMPE 2000 Proceedings*. Long Beach CA, 2000. v. 709.

GURDAL, Z.; OLMEDO, R. In-plane response of laminates with spatially varying fiber orientations-variable stiffness concept. *AIAA journal*, v. 31, n. 4, p. 751–758, 1993.

GURDAL, Z.; TATTING, B.; WU, K. Tow-placement technology and fabrication issues for laminated composite structures. In: AIAA. *46th AIAA/ASME/ASCE/AHS/ASC structures, structural dynamics and materials conference*. Austin, Texas, 2005. p. 2017.

GÜRDAL, Z.; TATTING, B. F.; WU, C. Variable stiffness composite panels: effects of stiffness variation on the in-plane and buckling response. *Composites Part A: Applied Science and Manufacturing*, Elsevier, v. 39, n. 5, p. 911–922, 2008.

HAO, P. et al. Buckling optimization of variable-stiffness composite panels based on flow field function. *Composite Structures*, Elsevier, v. 181, p. 240–255, 2017.

HAO, P. et al. Isogeometric buckling analysis of composite variable-stiffness panels. *Composite Structures*, Elsevier, v. 165, p. 192–208, 2017.

HARIK, R. et al. Automated fiber placement defect identity cards: cause, anticipation, existence, significance, and progression. In: SAMPE. *SAMPE Conference Proceedings*. Long Becach, CA, 2018.

HUANG, J.; HAFTKA, R. Optimization of fiber orientations near a hole for increased load-carrying capacity of composite laminates. *Structural and Multidisciplinary Optimization*, Springer, v. 30, n. 5, p. 335–341, 2005.

HUGHES, T. J. *The finite element method: linear static and dynamic finite element analysis*. New York: Dover Publications, 2000.

HYER, M. W.; CHARETTE, R. Use of curvilinear fiber format in composite structure design. *AIAA journal*, v. 29, n. 6, p. 1011–1015, 1991.

JONES, R. M. *Mechanics of composite materials*. New York: Taylor and Francis Group, 1998.

KAW, A. K. *Mechanics of composite materials*. FL, USA: CRC press, 2005.

KOLLAR, L. P.; SPRINGER, G. S. *Mechanics of composite structures*. Cambridge: Cambridge university press, 2003.

KUMAR, Y. The rayleigh–ritz method for linear dynamic, static and buckling behavior of beams, shells and plates: A literature review. *Journal of Vibration and Control*, SAGE Publications Sage UK: London, England, v. 24, n. 7, p. 1205–1227, 2018.

LI, R.; KELLY, D.; CROSKY, A. Strength improvement by fibre steering around a pin loaded hole. *Composite Structures*, Elsevier, v. 57, n. 1-4, p. 377–383, 2002.

LOPES, C.; GÜRDAL, Z.; CAMANHO, P. Variable-stiffness composite panels: Buckling and first-ply failure improvements over straight-fibre laminates. *Computers & Structures*, Elsevier, v. 86, n. 9, p. 897–907, 2008.

MAROUENE, A. et al. Buckling behavior of variable-stiffness composite laminates manufactured by the tow-drop method. *Composite Structures*, Elsevier, v. 139, p. 243–253, 2016.

MARSH, G. Airbus a350 xwb update. *Reinforced plastics*, Elsevier, v. 54, n. 6, p. 20–24, 2010.

MIKHAILOV, M. Modelling unsaturated flow by using mathematica. *Communications in numerical methods in engineering*, Wiley Online Library, v. 24, n. 11, p. 947–959, 2008.

NIK, M. A. et al. Optimization of variable stiffness composites with embedded defects induced by automated fiber placement. *Composite Structures*, Elsevier, v. 107, p. 160–166, 2014.

OÑATE, E. *Structural analysis with the finite element method. Linear statics: volume 2: beams, plates and shells*. Barcelona: Springer Science & Business Media, 2013.

PARNAS, L.; ORAL, S.; CEYHAN, Ü. Optimum design of composite structures with curved fiber courses. *Composites science and technology*, Elsevier, v. 63, n. 7, p. 1071–1082, 2003.

PEREIRA, D. de A. *Frequency and damping analyses of variable-angle tow CFRP laminates: numerical modeling, experimental assessment and optimization*. Tese (Doutorado) — Instituto Tecnológico de Aeronáutica, 2019.

REDDY, J. N. *An introduction to continuum mechanics*. Cambridge: Cambridge university press, 2007.

SADD, M. *Elasticity: Theory, Applications, and Numerics*. Boston: Elsevier Science, 2009.

SAWICKI, A.; MINGUETT, P. The effect of intraply overlaps and gaps upon the compression strength of composite laminates. In: AIAA. *39th AIAA/ASME/ASCE/AHS/ASC Structures, Structural Dynamics, and Materials Conference and Exhibit*. Long Beach, CA, USA, 1998. p. 1786.

SETOODEH, S. et al. Design of variable-stiffness composite panels for maximum buckling load. *Composite structures*, Elsevier, v. 87, n. 1, p. 109–117, 2009.

SMITH, F.; GRANT, C. Automated processes for composite aircraft structure. *Industrial Robot: An International Journal*, Emerald Group Publishing Limited, 2006.

STODIECK, O. et al. Improved aeroelastic tailoring using tow-steered composites. *Composite Structures*, Elsevier, v. 106, p. 703–715, 2013.

TATTING, B. F.; GURDAL, Z. *Design and manufacture of elastically tailored tow placed plates (NASA/CR–2002-211919)*. Hampton, Virginia, 2002.

TSAI, S. W.; HAHN, T. H. *Introduction to Composite Materials*. Lancaster: Technomic Publishing Company, Inc., 1980.

TUROSKI, L. E. *Effects of manufacturing defects on the strength of toughened carbon/epoxy prepreg composites*. Tese (Doutorado) — Montana State University-Bozeman, College of Engineering, 2000.

VASILIEV, V. V.; MOROZOV, E. V. *Mechanics and analysis of composite materials*. Oxford: Elsevier, 2001.

WALDHART, C. *Analysis of tow-placed, variable-stiffness laminates*. Dissertação (Mestrado) — Virginia Tech, 1996.

WHITNEY, J. M. *Structural analysis of laminated anisotropic plates*. Lancaster: Technomic Publishing Company, Inc., 1987.

WOLFRAM, S. et al. *The MATHEMATICA® book*. Cambridge: Cambridge university press, 1999.

WU, Z. et al. Buckling analysis and optimisation of variable angle tow composite plates. *Thin-walled structures*, Elsevier, v. 60, p. 163–172, 2012.

ZHU, Y. et al. Fiber path optimization based on a family of curves in composite laminate with a center hole. *Composites Part B: Engineering*, Elsevier, v. 111, p. 91–102, 2017.